

© 2015

Maryam Taherinejad

**ALL RIGHTS RESERVED**

# CHARACTERIZATION OF TOPOLOGICAL INSULATORS AND SEMICONDUCTORS

By

MARYAM TAHERINEJAD

A dissertation submitted to the  
Graduate School—New Brunswick  
Rutgers, The State University of New Jersey  
in partial fulfillment of the requirements  
for the degree of  
Doctor of Philosophy  
Graduate Program in Physics and Astronomy

written under the direction of  
Professor David Vanderbilt  
and approved by

---

---

---

---

---

New Brunswick, New Jersey

October, 2015

## ABSTRACT OF THE DISSERTATION

# CHARACTERIZATION OF TOPOLOGICAL INSULATORS AND SEMICONDUCTORS

By MARYAM TAHERINEJAD

Dissertation Director:

Professor David Vanderbilt

The theoretical prediction and experimental observation of topological insulators (TIs) and semiconductors in recent years have opened the floodgates to many interesting physical phenomena and potential technological applications. A major part of this work is devoted to characterization of topological insulators and semiconductors. We argue that various kinds of TIs can be insightfully characterized by an inspection of the charge centers of the hybrid Wannier functions, defined as the orbitals obtained by carrying out a Wannier transform on the Bloch functions in one dimension while leaving them Bloch-like in the other two. From this procedure, one can obtain the Wannier charge centers (WCCs) and plot them in the two-dimensional projected Brillouin zone. We show that these WCC sheets contain the same kind of topological information as is carried in the surface energy bands, with the crucial advantage that the topological properties of the bulk can be deduced from bulk calculations alone. The distinct topological behaviors of these WCC sheets in trivial, Chern, weak, strong, crystalline TIs, and in Weyl semimetal, are first illustrated by calculating them for simple tight-binding models. We then present the results of first-principles calculations

of the WCC sheets in the trivial insulator  $\text{Sb}_2\text{Se}_3$ , the weak TI  $\text{KHgSb}$ , and the strong TI  $\text{Bi}_2\text{Se}_3$ , confirming the ability of this approach to distinguish between different topological behaviors in an advantageous way.

We also study the adiabatic pumping of the Chern-Simons axion (CSA) coupling along a parametric loop characterized by a non-zero second Chern number  $C^{(2)}$  from the viewpoint of the hybrid Wannier representation. We derive a new formula for the CSA coupling, expressing it as an integral involving Berry curvatures and potentials defined on the WCC sheets. We show that a loop characterized by a non-zero  $C^{(2)}$  requires a series of sheet-touching events at which  $2\pi$  quanta of Berry curvature are passed from sheet to sheet, in such a way that  $e^2/h$  units of CSA coupling are pumped by a lattice vector by the end of the cycle. We illustrate these behaviors via explicit calculations on a model tight-binding Hamiltonian and discuss their implications.

Finally, we study the Bloch-type domain walls in rhombohedral  $\text{BaTiO}_3$ . Ferroelectric domain walls (FDWs) are usually considered to be of Ising type, but there have been suggestions in recent years that Bloch-type FDWs are also possible in some cases, e.g., in the rhombohedral phase of  $\text{BaTiO}_3$ . The mechanically compatible and electrically neutral FDWs in rhombohedral  $\text{BaTiO}_3$  are of  $71^\circ$ ,  $109^\circ$ , and  $180^\circ$  type. We have investigated these FDWs based both on first-principles calculations and on a Ginzburg-Landau-Devonshire (GLD) model. The results from both approaches confirm the Ising nature of the  $71^\circ$  FDW and the Bloch nature of the  $180^\circ$  FDW, and predict both Ising-type and Bloch-type FDWs are possible for the  $109^\circ$  case. In view of the relatively small rhombohedral strain in  $\text{BaTiO}_3$ , the results can be explained reasonably well by regarding a Bloch FDW as composed of a pair of smaller-angle Ising FDWs, and by comparing the sum of the energies of these constituents with an Ising-type solution. A reduction by 40% in the parameters describing the gradient term in the GLD model brings it into better agreement with the first-principles results for detailed properties such as the energies and widths of the FDWs.

## Acknowledgments

I am grateful to my adviser David Vanderbilt without whose guidance this work was not possible. David has been not only a wise adviser and an insightful scientist, but also a great role model. No word can express my gratitude, but I will try to appreciate what I have learnt best by implementing them in my professional and personal life.

I have also learnt a lot from the amazing condensed matter community at Rutgers Physics and Astronomy department, and I would like to thank Karin Rabe, Donald Hamann, Natan Andrei, Eva Andrie, Kristjan Haule, Premi Chandra, Lev Ioffe, Emil Yuzbashyan, Girsh Blumberg, Gabriel Kotliar, and Piers Coleman. I am also grateful to our supporting graduate directors Ronald Ransome, Ted Williams, Jolie Cizewski, and Ronald Gilman.

During my years of graduate school I was lucky to enjoy the companionship of bright postdoctoral fellows and graduate students. Among many others I would like to thank Sinisia Coh, Alexey Soluyanov, Anindya Roy, Jianpeng Liu, Kevin Garitty, Meng Ye, Matthew Foster, Chuck-Hou Yee, Victor Alexandrov, Aline Ramires, Turan Birol, and Onur Erten.

I also need to thank Abraham Ayvazian and Farideh Tehrani for believing in me. I may not have been here, had it not been for their support and encouragement.

I am especially grateful to my parents Tahereh Shahidi and Abolhassan Taherinejad for their unconditional love and support, and for bearing the heaviness of being apart for all these years. I am also grateful to my brothers Amir Hossein and Sina and my amazing friends Fariba Karimi, Mehrnoush Manouchehri, Nasim Mozaffari, Mahdieh Hashemi, and Akram Delbari. Last but not least, I am grateful to my dear Michael whose love and support has given a different meaning to my life.

## Dedication

To my parents Tahereh and Abolhassan

# Table of Contents

<b>Abstract</b> . . . . .	ii
<b>Acknowledgments</b> . . . . .	iv
<b>Dedication</b> . . . . .	v
<b>List of Tables</b> . . . . .	ix
<b>List of Figures</b> . . . . .	x
<b>1. Introduction</b> . . . . .	1
<b>2. Representations of Crystalline Solids</b> . . . . .	3
2.1. The One-electron Approximation . . . . .	4
2.2. Density Functional Theory . . . . .	5
2.3. Bloch Band Theory . . . . .	8
2.4. Wannier Representation . . . . .	11
2.4.1. Gauge Freedom . . . . .	11
2.4.2. Maximally Localized Wannier Functions . . . . .	12
2.5. Tight-binding Approximation . . . . .	14
2.6. Geometrical Phases in Matter . . . . .	15
<b>3. Topological Aspects of Wannier Charge Centers</b> . . . . .	18
3.1. Wannier Charge Centers . . . . .	19
3.1.1. Construction . . . . .	21

3.2. Bulk-boundary Correspondence . . . . .	22
3.2.1. Symmetry . . . . .	23
3.2.2. Topology . . . . .	24
3.3. Berry Phase and Electric Polarization . . . . .	28
3.3.1. Electric Polarization in Nontrivial Insulators . . . . .	29
<b>4. Topological Insulating and Semiconducting Phases in 3D . . . . .</b>	<b>31</b>
4.1. Tight-binding Models . . . . .	31
4.2. Material Systems . . . . .	35
4.2.1. Computational Methods . . . . .	36
4.3. Results . . . . .	37
4.4. TR-broken Chern insulator . . . . .	39
4.5. TR-invariant trivial insulator . . . . .	42
4.6. TR-invariant weak topological insulator . . . . .	43
4.7. TR-invariant strong topological insulator . . . . .	46
4.8. Crystalline topological insulator . . . . .	48
4.9. Weyl Semimetal . . . . .	50
4.10. Summary . . . . .	52
<b>5. Adiabatic Pumping of Chern-Simons Axion Coupling . . . . .</b>	<b>54</b>
5.1. CSA Coupling in Wannier Representation . . . . .	57
5.2. Tight-binding Model . . . . .	62
5.3. WCC Sheets' Evolution . . . . .	63
5.4. CSA Coupling Pump . . . . .	64
5.5. Symmetries . . . . .	66
5.6. Perturbations . . . . .	67
5.7. Slab Configuration . . . . .	68



5.8. Summary . . . . .	69
<b>6. Bloch-type Ferroelectric Domain Walls in BaTiO<sub>3</sub> . . . . .</b>	<b>70</b>
6.1. Domain wall and supercell geometries . . . . .	72
6.2. Computational Approach . . . . .	77
6.2.1. First-principles calculations . . . . .	77
6.2.2. The GLD model . . . . .	78
6.2.3. Domain-wall width . . . . .	80
6.3. Results . . . . .	80
6.3.1. The R71° domain wall . . . . .	81
6.3.2. The R109° domain wall . . . . .	83
6.3.3. The R180°{110} domain wall . . . . .	84
6.4. Discussion . . . . .	87
6.5. Summary . . . . .	88
<b>Bibliography . . . . .</b>	<b>90</b>

## List of Tables

4.1. Topological phase of the FKM model as a function of parameter $\alpha$ . . . . .	33
6.1. Dynamical effective charges of atoms in BaTiO <sub>3</sub> . . . . .	80
6.2. Energies and widths of FDWs in BaTiO <sub>3</sub> . . . . .	86

## List of Figures

3.1. Wannier charge centers flow . . . . .	25
4.1. Surface energy bands and WCC sheets for the TR-broken Chern insulator model . . . . .	40
4.2. Surface energy bands and WCC sheets for the TR-invariant FKM model in the trivial phase . . . . .	41
4.3. First-principles WCC sheets along $\hat{z}$ for topologically trivial $\text{Sb}_2\text{Se}_3$ . . . . .	43
4.4. Surface energy bands and WCC sheets for the TR-invariant FKM model in the weak topological phase . . . . .	44
4.5. First-principles WCC sheets for the weak TI $\text{KHgSb}$ . . . . .	45
4.6. Surface energy bands and WCC sheets for the TR-invariant FKM model in the strong topological phase . . . . .	47
4.7. First-principles WCC sheets for the strong TI $\text{Bi}_2\text{Se}_3$ . . . . .	48
4.8. Surface energy bands and WCC sheets for tight-binding model of a crystalline TI . . . . .	49
4.9. WCCs along $\hat{z}$ vs. $(k_x, k_y)$ and WCCs along $\hat{y}$ vs. $(k_x, k_z)$ for Weyl semimetal	52
5.1. The adiabatic loop . . . . .	62
5.2. The two WCC sheets of the half-filled FKM model . . . . .	63
5.3. The WCCs at the $M$ -point and $\Gamma$ -point . . . . .	64
5.4. The CSA coupling $\theta(\alpha)$ . . . . .	65
6.1. symmetry-allowed polarization directions in $\text{BaTiO}_3$ . . . . .	71
6.2. The $\text{R}71^\circ$ , $\text{R}109^\circ$ and $\text{R}180^\circ\{1\bar{1}0\}$ FDWs in $\text{BaTiO}_3$ . . . . .	73

6.3. 10-atom rotated building block . . . . .	74
6.4. Supercell with four rotated 10-atom units . . . . .	75
6.5. Polarization profiles of Ising $R71^\circ$ FDWs in rhombohedral $\text{BaTiO}_3$ . . . . .	81
6.6. Polarization profiles for Ising $R109^\circ$ FDWs in $\text{BaTiO}_3$ . . . . .	82
6.7. Polarization profiles for Bloch $R109^\circ$ FDWs in $\text{BaTiO}_3$ . . . . .	83
6.8. Polarization profiles for Ising $R180^\circ\{1\bar{1}0\}$ FDWs in $\text{BaTiO}_3$ . . . . .	84
6.9. Polarization profiles for Bloch $R180^\circ\{1\bar{1}0\}$ FDWs in $\text{BaTiO}_3$ . . . . .	85
6.10. The path swept by the polarization vector . . . . .	87

# Chapter 1

## Introduction

The theoretical prediction and experimental observation of TIs and semiconductors in recent years have opened the floodgates to many interesting physical phenomena and potential technological applications. Among many interesting characteristics, these classes of material have unique transport properties which are protected against disorder and impurity by the non-trivial topology of their ground state wave function.

Many different phases of matter with non-trivial topology have been predicted and classified since the work of Thouless *et al.* [9] explaining the topological nature of the integer quantum Hall effect; however, for many of these phases a material realization still remains to be found. Moreover, the small bulk energy gap in the current topological insulators makes them not practical for many applications in room temperature. Therefore, study of materials or configurations which can realize the predicted topological phases and enhance their properties for technological applications is very important. A major theme of this dissertation is development of a universal framework which can be the basis for understanding and efficient computational studies of topological properties of materials.

TIs are gapped in the bulk, like trivial insulators, but they are required to have robust metallic states on the edge (2D) or surface (3D). These unique surface states provide the strongest experimentally accessible signature of insulators with non-trivial topology. However, for reasons of both computational efficiency and theoretical clarity, it is preferable to be able to calculate and understand the topological phases of materials purely from bulk calculations. The method introduced in this work relies on the use of hybrid Wannier functions, which are localized in one direction and periodic in the remaining directions.

The charge centers of these hybrid Wannier functions can be plotted as sheets over two-dimensional projected Brillouin zone and contain the same kind of topological information as is carried in the surface energy bands. This method is not limited to crystals with special symmetries and has the advantage of being computationally efficient.

In Chapter 2, I introduce the basic ideas and methods used in rest of this dissertation. Different representations of crystalline materials, such as Bloch and Wannier functions, are introduced in this chapter, as well as two methods of doing electronic structure calculations: the tight-binding approximation and density functional theory. Geometrical phases in matter, such as Berry potential and Berry curvature, are also reviewed in this chapter.

The bulk-boundary correspondence between the surface energy bands and WCC spectrum is established in Chapter 3, and it is shown that the Wannier spectrum contain the same kind of topological information as is carried in the surface energy bands, with the crucial advantage that the topological properties of the bulk can be deduced from bulk calculations alone.

In Chapter 4, the distinct topological behaviour of WCC is illustrated for various 3D topological insulating and semiconducting phases using tight-binding models. Then the results of first-principles calculations of the WCC sheets in materials of various topological classes are presented, confirming the ability of this approach to distinguish between different topological behaviors in an advantageous way.

In Chapter 5, we generalize the method to an adiabatic loop in four-dimensional parametric space. One of the main results of this work is presented in this chapter, where a new formula for the Chern-Simons axion coupling in the hybrid Wannier function representation is derived in terms of a Berry curvature dipole term and a non-topological term.

The subject studied in Chapter 6 is ferroelectric domain walls in  $\text{BaTiO}_3$ . This material is a trivial insulator, but in a similar way to the WCC spectrum calculations, we study the evolution of polarization vector across each domain wall by calculating the polarization components in layers normal to the wall.

## Chapter 2

### Representations of Crystalline Solids

Crystalline solids are composed of mutually interacting electrons and nuclei. The exact description of these systems requires considering the full dynamics of all particles. However, the big difference in masses of electrons and nuclei makes it possible to ignore the influence of nuclear motions on electrons and separate the description of their motions. The occasional break down of this assumption leads to interesting phenomena like superconductivity, but many physical properties of real materials can be described by considering electrons in a rigid, infinite, periodic lattice. An immediate consequence of this assumption is that the electron wave functions follow the symmetries of the lattice. After making the single-particle approximation (see Sec. 2.1), the lattice translational symmetry leads to Bloch's theorem which states the wave function of electrons in a lattice consists of a free wave and a lattice-periodic part. In presence of defects, impurities, or external fields this theorem is not valid any more, but the complete set of Bloch functions provide a natural basis in which the electron wave function can be expanded.

An alternative representation, which has proven to be convenient for many purposes, is the set of localised Wannier functions (WFs) which are related to the Bloch functions by a unitary transformation. The WFs play an important role in the modern theory of polarization and topological classifications of insulators, which are the subject of Chapters 3, 4, and 5. They also provide an insight into the nature of chemical bonding, and have been broadly used to construct model Hamiltonians for different systems. For many practical purposes the physical properties of the material can be described by considering a smaller set of orbital functions. This method, which is known as the tight-binding approximation,

is explained in Sec. 2.5 after a review of Bloch and Wannier representations in Sections 2.3 and 2.4. A brief review of density functional theory, which is the basis of a very successful computational method for studying the ground state properties of materials, is given in Sec. 2.2.

## 2.1 The One-electron Approximation

The total non-relativistic Hamiltonian for a system of mutually interacting electrons and nuclei includes the kinetic energy of all particles and Coulomb terms describing electron-electron, nucleus-nucleus, and electron-nucleus interactions. Considering the large difference between the electron and nuclear masses, the first step to simplify this problem is ignoring the vibrations of nuclei. In this simple but drastic approximation, the nuclear positions become classical variables and we can sum their effect on the electrons dynamics in an effective periodic potential  $V_{\text{nuc}}$ . Then the many-electron wave function of  $N$  electrons in the presence of nuclei in fixed positions is described by an effective Hamiltonian which includes the kinetic energy of electrons plus the potential energy due to the nuclei

$$H_{\text{eff}}\Psi(\mathbf{r}_1\sigma_1, \mathbf{r}_2\sigma_2, \dots, \mathbf{r}_N\sigma_N) = E\Psi(\mathbf{r}_1\sigma_1, \mathbf{r}_2\sigma_2, \dots, \mathbf{r}_N\sigma_N), \quad (2.1)$$

where  $\mathbf{r}_i\sigma_i$  are the position and spin of  $i$ -th electron, and  $H_{\text{eff}}$  can be written as

$$H_{\text{eff}} = \sum_i^N \left[ \frac{p_i^2}{2m} + V_{\text{nuc}}(\mathbf{r}_i) \right] + \frac{1}{2} \sum_{i \neq j}^N \frac{e^2}{r_{ij}}. \quad (2.2)$$

Here  $\mathbf{p}_i$  and  $\mathbf{r}_i$  are the electron momenta and coordinates, and  $e$  and  $m$  denote the electron charge and mass. The last term on the right hand side of Eq. 2.2 describes the electron-electron Coulomb interactions, with the exclusion of the self-interaction terms  $i = j$ .

A pioneering approach to solve this problems is *Hartree-Fock theory*, where the total  $N$ -electron ground-state wave function is represented by an antisymmetrized product of  $N$



one-electron wave functions  $\psi_i(\mathbf{r}_i\sigma_i)$

$$\Psi(\mathbf{r}_1\sigma_1, \mathbf{r}_2\sigma_2, \dots, \mathbf{r}_N\sigma_N) = \frac{1}{\sqrt{N!}} \begin{vmatrix} \psi_1(\mathbf{r}_1\sigma_1) & \psi_1(\mathbf{r}_2\sigma_2) & \cdots & \psi_1(\mathbf{r}_N\sigma_N) \\ \psi_2(\mathbf{r}_1\sigma_1) & \psi_2(\mathbf{r}_2\sigma_2) & \cdots & \psi_2(\mathbf{r}_N\sigma_N) \\ \vdots & \vdots & \ddots & \vdots \\ \psi_N(\mathbf{r}_1\sigma_1) & \psi_N(\mathbf{r}_2\sigma_2) & \cdots & \psi_N(\mathbf{r}_N\sigma_N) \end{vmatrix}. \quad (2.3)$$

Now the original many-body problem can be replaced by a set of single particle eigenvalue problems

$$H\psi_i(\mathbf{r}) = \varepsilon_i\psi_i(\mathbf{r}). \quad (2.4)$$

The effect of the electron spin is reflected in the antisymmetric property of the many-electron wavefunction, and although the one-electron wave functions carry a spin index, we can drop this index for the rest of this chapter. The spin index needs to be restored when spin-orbit interaction is present.

In the *mean field approximation* it is assumed that each electron moves in the effective field generated by the Coulomb potential of all the other  $N - 1$  electrons. Then the single electron Hamiltonian can be written as

$$H = \frac{\mathbf{p}^2}{2m} + V_{\text{eff}}(\mathbf{r}). \quad (2.5)$$

where the effective potential  $V_{\text{eff}}$  is calculated from the electron charge density given by one-electron wave functions, and is determined in a self-consistent way.

## 2.2 Density Functional Theory

In 1964 Hohenberg and Kohn[2] proved that the properties of the many-electron system can be uniquely determined from the one-body electron density

$$n(\mathbf{r}) = N \int \Psi^*(\mathbf{r}\sigma_1, \mathbf{r}_2\sigma_2, \dots, \mathbf{r}_N\sigma_N) \Psi(\mathbf{r}_1\sigma_1, \mathbf{r}_2\sigma_2, \dots, \mathbf{r}_N\sigma_N) d\mathbf{r}_2 \dots d\mathbf{r}_N, \quad (2.6)$$

obtained from the many-body ground state  $\Psi$ . This is the basis of density functional theory (DFT), which provides an approximate way to study the ground-state properties of many-electron systems by constructing a one-electron problem with an effective potential.

Consider a system of  $N$  electrons, described by the Hamiltonian in Eq. 2.1. For convenience let us write this Hamiltonian in terms of an internal part  $H_{\text{int}}$  which includes the kinetic energy of the electrons plus electron-electron Coulomb interactions, and an external part  $V_{\text{ext}}$  which includes the electronic-nuclear interactions

$$H_{\text{int}} = T + V_{ee} = \sum_i^N \frac{\mathbf{p}_i^2}{2m} + \frac{1}{2} \sum_{i \neq j}^N \frac{e^2}{r_{ij}} \quad (2.7)$$

$$V_{\text{ext}} = \sum_i^N v_{\text{ext}}(\mathbf{r}_i), \quad (2.8)$$

where  $v_{\text{ext}}(\mathbf{r}) \equiv V_{\text{nucl}}(\mathbf{r})$ . The first Hohenberg-Kohn theorem states that there is a one-to-one correspondence between the external potential  $v_{\text{ext}}$  and the ground state electron density  $n(\mathbf{r})$ , where  $H_{\text{int}}$  is taken as fixed. In other words there exists a functional that links  $n(\mathbf{r})$  and  $v_{\text{ext}}$

$$n = F[v_{\text{ext}}]. \quad (2.9)$$

The second Hohenberg-Kohn theorem ensures that there exists a unique energy functional  $E^{(\text{HK})}[n(\mathbf{r}), v_{\text{ext}}]$  that is minimal at the exact ground-state density, and its minimum gives the exact ground-state energy of the many-electron system

$$E^{(\text{HK})}[n(\mathbf{r}), v_{\text{ext}}] = T[n(\mathbf{r})] + V_{ee}[n(\mathbf{r})] + \int v_{\text{ext}}(\mathbf{r})n(\mathbf{r})d\mathbf{r}. \quad (2.10)$$

The functional  $F[n(\mathbf{r})] = T[n(\mathbf{r})] + V_{ee}[n(\mathbf{r})]$  is universal and does not depend on  $v_{\text{ext}}$ ; however, the exact form of the functional  $F[n(\mathbf{r})]$  is not known and it must be approximated. An iterative solution scheme introduced by Kohn and Sham [3] has been widely used to construct a good approximate mean-field solution using DFT. This approach is based on

finding a noninteracting many-body system with the same ground state as the interacting one.

The ground state of the noninteracting systems is described via Eq. 2.3 as Slater determinant of single-particle orbitals  $\psi_i$ . Then the ground state electron density is given by

$$n(\mathbf{r}) = \sum_i |\psi_i(\mathbf{r})|^2, \quad (2.11)$$

where the sum is over occupied orbitals. Now the energy functional in Eq. 2.10 can be written as

$$\begin{aligned} E[n(\mathbf{r})] = & -\frac{\hbar^2}{2m} \sum_i \langle \psi_i | \nabla^2 | \psi_i \rangle + \int \int \frac{n(\mathbf{r})n(\mathbf{r}')}{|\mathbf{r} - \mathbf{r}'|} d\mathbf{r} d\mathbf{r}' \\ & + \int v_{\text{ext}}(\mathbf{r})n(\mathbf{r})d\mathbf{r} + E_{\text{XC}}[n], \end{aligned} \quad (2.12)$$

in terms of noninteracting orbitals, where the effect of interactions is captured in exchange-correlation functional  $E_{\text{XC}}[n]$ . Minimizing this energy functional with respect to  $\psi_i$  leads to the Kohn-Sham equations for the single particle orbitals

$$\left[ -\frac{\hbar^2}{2m} \nabla^2 + V_{\text{eff}} \right] \psi_i = \varepsilon_i \psi_i, \quad (2.13)$$

where

$$V_{\text{eff}} = \int \frac{n(\mathbf{r}')}{|\mathbf{r} - \mathbf{r}'|} d\mathbf{r}' + v_{\text{ext}}(\mathbf{r}) + V_{\text{XC}}. \quad (2.14)$$

The one-particle potential

$$V_{\text{XC}} = \frac{\delta E_{\text{XC}}}{\delta n(\mathbf{r})} \quad (2.15)$$

is the variational functional derivative of exchange-correlation functional. Kohn and Sham showed that if the exact exchange-correlation functional  $E_{\text{XC}}$  is known and if the one-particle potential  $V_{\text{XC}}$  can be computed, then an iterative self consistent solution of Eq. 2.13 would yield the exact ground state and total energy [3]. However, since the exact  $E_{\text{XC}}$  is not

known different approximation to the exchange-correlation functional have been developed for practical calculations.

In Chapter 4 we employ this approach to study topological properties of different band insulators. Strong electron-electron correlations do not play a significant role in the properties of the materials we studied and the exchange-correlation functional works reasonably well for these types of materials.

### 2.3 Bloch Band Theory

The one-electron wave functions  $\psi(\mathbf{r})$  must transform under the symmetries of the crystal, which in general include rotational (both proper and improper) and translational elements. The translation symmetry subgroup is Abelian, which means its irreducible representations are one-dimensional. This leads to the *Bloch theorem*, which is a fundamental result in the theory of solids.

Let  $T(\mathbf{R}_i)$  denote a lattice translation operator. The Hamiltonian  $H$  that describes the one-electron wave functions must commute with this operator,

$$[H, T(\mathbf{R}_i)] = 0. \quad (2.16)$$

The translation operators also commute with each other

$$[T(\mathbf{R}_i), T(\mathbf{R}_j)] = 0, \quad (2.17)$$

which means the one-electron wave functions  $\psi(\mathbf{r})$  must be simultaneous eigenfunctions of the Hamiltonian and of all the lattice translations. The norm of wave function will be unchanged by lattice translation

$$|\psi(\mathbf{r} + \mathbf{R}_i)| = |\psi(\mathbf{r})|, \quad (2.18)$$

thus

$$T(\mathbf{R}_i)\psi(\mathbf{r}) = \psi(\mathbf{r} + \mathbf{R}_i) = \lambda_i\psi(\mathbf{r}) \quad (2.19)$$

where  $\lambda_i = \exp(i\theta_i)$  is a complex number of modulus unity. The phase  $\theta_i$  is real and can be determined by considering two translation operators, say  $T(\mathbf{R}_i)$  and  $T(\mathbf{R}_j)$  acting in succession. The result will be a single translation  $T(\mathbf{R}_i + \mathbf{R}_j)$ , which means  $\theta_i$  is linearly related to the displacement  $\mathbf{R}_i$ . The eigenvalue  $\lambda_i$  is unity for a translation of zero length, therefore

$$\theta_i = \mathbf{k} \cdot \mathbf{R}_i. \quad (2.20)$$

The wave vector  $\mathbf{k}$  is the same for all lattice translation operations and characterizes the wave function of an electron in a crystal. Using these results, *Bloch's theorem* can be expressed as

$$\psi(\mathbf{k}, \mathbf{r} + \mathbf{R}_i) = \exp(i\mathbf{k} \cdot \mathbf{R}_i)\psi(\mathbf{k}, \mathbf{r}). \quad (2.21)$$

Let  $\mathbf{a}_i$  denote the lattice vectors which define the unit cell in the periodic crystal. Any lattice translation vector can be expressed in terms of these lattice basis vectors

$$\mathbf{R}_n = \sum_{i=1}^d n_i \mathbf{a}_i, \quad (2.22)$$

where  $d$  is the dimensions of the lattice and  $n_i$  are integers. The Fourier transform of any wave function defined over the periodic lattice is represented in reciprocal space, which is the counterpart of the crystalline lattice in momentum space. The reciprocal lattice basis vectors  $\mathbf{b}_i$  are defines as

$$\mathbf{a}_i \cdot \mathbf{b}_j = 2\pi\delta_{ij}, \quad (2.23)$$

and the reciprocal lattice unit cell defined by these basis vectors is called Brillouin zone

(BZ). Any reciprocal lattice vector  $\mathbf{K}$  can be expressed in terms of these basis vectors

$$\mathbf{K} = \sum_{i=1}^d m_i \mathbf{b}_i, \quad (2.24)$$

where  $m_i$  are integers. We adopt the convention that the domain of  $\mathbf{k}$  is restricted to the first BZ, since for any reciprocal lattice vector  $\mathbf{K}$

$$\psi(\mathbf{k}, \mathbf{r}) = \psi(\mathbf{k} + \mathbf{K}, \mathbf{r}). \quad (2.25)$$

There can be more than one wave function for any given wave vector  $\mathbf{k}$ . These different solutions are labeled by index  $n$  and satisfy the eigenvalue equation

$$H\psi_n(\mathbf{k}, \mathbf{r}) = E_n(\mathbf{k})\psi_n(\mathbf{k}, \mathbf{r}). \quad (2.26)$$

The function  $E_n(\mathbf{k})$  is referred to as the energy band function and the wave function  $\psi_n(\mathbf{k}, \mathbf{r})$ , labelled by a crystal momentum  $\mathbf{k}$  and a band index  $n$ , is called a Bloch function.

The electron wave function can also be described by the function  $u_n(\mathbf{k}, \mathbf{r})$  defined by the relation

$$\psi_n(\mathbf{k}, \mathbf{r}) = \exp(i\mathbf{k} \cdot \mathbf{r})u_n(\mathbf{k}, \mathbf{r}). \quad (2.27)$$

From Bloch's theorem

$$\begin{aligned} \psi_n(\mathbf{k}, \mathbf{r} + \mathbf{R}_i) &= \exp[i\mathbf{k} \cdot (\mathbf{r} + \mathbf{R}_i)]u_n(\mathbf{k}, \mathbf{r} + \mathbf{R}_i) \\ &= \exp(i\mathbf{k} \cdot \mathbf{R}_i)[\exp(i\mathbf{k} \cdot \mathbf{r})u_n(\mathbf{k}, \mathbf{r} + \mathbf{R}_i)], \end{aligned} \quad (2.28)$$

which shows the function  $u_n(\mathbf{k}, \mathbf{r})$ , known as cell-periodic Bloch function, must be unchanged by any lattice translation

$$u_n(\mathbf{k}, \mathbf{r} + \mathbf{R}_i) = u_n(\mathbf{k}, \mathbf{r}). \quad (2.29)$$

It is easy to show that the Bloch functions form an orthogonal complete set,

$$\int \psi_n^*(\mathbf{k}, \mathbf{r}) \psi_m(\mathbf{q}, \mathbf{r}) d\mathbf{r} = \frac{(2\pi)^3}{V} \delta_{nm} \delta(\mathbf{k} - \mathbf{q}), \quad (2.30)$$

where  $V$  is the real-space primitive cell volume. In the presence of impurities, defects or external fields the assumption of a perfect periodic lattice is not valid. However, the set of Bloch functions defined in the perfect crystal is a natural basis to expand the wave function of an electron.

## 2.4 Wannier Representation

The electronic ground state in periodic crystalline solids can alternatively be represented by the set of localized orbitals or WFs, which are defined in relation to the Bloch functions by a unitary transformation:

$$|W_n(\mathbf{R})\rangle = \frac{V}{(2\pi)^3} \int_{\text{BZ}} d\mathbf{k} e^{i\mathbf{k} \cdot (\mathbf{r} - \mathbf{R})} |u_{n\mathbf{k}}\rangle. \quad (2.31)$$

Here  $\mathbf{R}$  is a lattice vector and  $u_{n\mathbf{k}}$  is a periodic Bloch function. For the rest of this document we use this notation for the Bloch functions. It is easily shown that the set of WFs form an orthogonal complete set, and although they are not eigenstates of the Hamiltonian, they provide a valid description of the band subspace.

### 2.4.1 Gauge Freedom

The WFs are not unique, as there is a gauge freedom in the definition of Bloch functions  $\psi_{n\mathbf{k}}(\mathbf{r})$ . The physical description of the system is intact under a  $\mathbf{k}$ -dependent phase twist

$$|\tilde{u}_{n\mathbf{k}}\rangle = e^{i\phi_n(\mathbf{k})} |u_{n\mathbf{k}}\rangle.$$

Here  $\phi_n(\mathbf{k})$  can be any real function that satisfies the periodic condition

$$\phi_n(\mathbf{k} + \mathbf{K}) = \phi_n(\mathbf{k}) + \mathbf{K} \cdot \mathbf{R}, \quad (2.32)$$

where  $\mathbf{K}$  and  $\mathbf{R}$  are reciprocal and real-space lattice vectors respectively, and  $\mathbf{K} \cdot \mathbf{R}$  is a integer multiple of  $2\pi$ . In general, WFs corresponding to Bloch functions with different choices of  $\mathbf{k}$ -dependent phase  $\phi_n(\mathbf{k})$  can have different shapes and spreads.

In the case of multiple occupied bands, there is also a more general  $U(N)$  gauge freedom in choosing the  $N$  representatives of the occupied space at each  $k$ -point,

$$|\tilde{u}_{n\mathbf{k}}\rangle = \sum_{m=1}^N U_{mn}(\mathbf{k}) |u_{m\mathbf{k}}\rangle. \quad (2.33)$$

Here  $|u_{m\mathbf{k}}\rangle$  belong to a manifold of  $N$  occupied bands which are separated from any other lower or upper bands, but may have degeneracies and crossings among themselves. The presence of degeneracy among these  $N$  occupied bands means that the immediate eigenstates of  $H$  do not define a smooth gauge in Eq. 2.33, and will not produce well-localized WFs in general. In this regard, choosing a unitary transformation  $U(N)$  that defines a set of Bloch functions with a smooth gauge is important for constructing well-localized WFs. Ideally, however, we would like to have a procedure to define maximally localized WFs.

### 2.4.2 Maximally Localized Wannier Functions

Various approaches have been developed to construct localized WFs by removing the non-analyticities at the points of degeneracy in the BZ by symmetry considerations [4, 5], or employing projection methods on the occupies subspace spanned by the Bloch orbitals [6, 7]. A very general approach was introduced by Marzari and Vanderbilt [8] by introducing the localization functional

$$\Omega = \sum_n [\langle W_n(\mathbf{0}) | r^2 | W_n(\mathbf{0}) \rangle - \langle W_n(\mathbf{0}) | \mathbf{r} | W_n(\mathbf{0}) \rangle^2] = \sum_n [\langle r^2 \rangle - \bar{\mathbf{r}}^2]. \quad (2.34)$$



This functional measures the sum of quadratic spreads of the  $N$  WFs in the home unit cell around their centers, and it is minimized with respect to the unitary transformation  $U_{mn}(\mathbf{k})$ .

Matrix elements of the position operator between WFs can be written as

$$\langle W_n(\mathbf{R}) | \mathbf{r} | W_m(\mathbf{0}) \rangle = i \frac{V}{(2\pi)^3} \int d\mathbf{k} e^{\mathbf{k} \cdot \mathbf{R}} \langle u_{nk} | \nabla_{\mathbf{k}} | u_{mk} \rangle \quad (2.35)$$

and

$$\langle W_n(\mathbf{R}) | r^2 | W_m(\mathbf{0}) \rangle = i \frac{V}{(2\pi)^3} \int d\mathbf{k} e^{\mathbf{k} \cdot \mathbf{R}} \langle u_{nk} | \nabla_{\mathbf{k}}^2 | u_{mk} \rangle. \quad (2.36)$$

The gradient of any smooth function  $f(\mathbf{k})$  can be expressed by finite differences as

$$\nabla f(\mathbf{k}) = \sum_{\mathbf{b}} \omega_b \mathbf{b} [f(\mathbf{k} + \mathbf{b}) - f(\mathbf{k})] + \mathcal{O}(b^2), \quad (2.37)$$

where  $\mathbf{b}$  is a vector connecting a  $\mathbf{k}$ -point to one of its neighbors and  $\omega_b$  is a geometric weighting factor that depends on the number nearest neighbor  $\mathbf{k}$ -points and their geometry. In a similar way,

$$|\nabla f(\mathbf{k})|^2 = \sum_{\mathbf{b}} \omega_b [f(\mathbf{k} + \mathbf{b}) - f(\mathbf{k})]^2. \quad (2.38)$$

Now the only information needed to calculate the reciprocal space derivatives of Eqs. 2.37 and 2.38 is encoded in the overlap matrix elements

$$M_{mn}^{\mathbf{k}, \mathbf{b}} = \langle u_{m\mathbf{k}} | u_{n, \mathbf{k} + \mathbf{b}} \rangle. \quad (2.39)$$

Using these matrix elements the localization functional can be written as sum of a gauge-invariant term  $\Omega_I$  and two gauge-dependent terms  $\Omega_{OD}$  and  $\Omega_D$

$$\Omega_I = \frac{1}{N_{cell}} \sum_{\mathbf{k}, \mathbf{b}} \omega_b (N - \sum_{mn} |M_{mn}^{\mathbf{k}, \mathbf{b}}|^2), \quad (2.40)$$

$$\Omega_{OD} = \frac{1}{N_{cell}} \sum_{\mathbf{k}, \mathbf{b}} \omega_b \sum_{m \neq n} |M_{mn}^{\mathbf{k}, \mathbf{b}}|^2, \quad (2.41)$$

$$\Omega_D = \frac{1}{N_{cell}} \sum_{\mathbf{k}, \mathbf{b}} \omega_b \sum_n (-\text{Im} \ln M_{nn}^{\mathbf{k}, \mathbf{b}} - \mathbf{b} \cdot \bar{\mathbf{r}}_n), \quad (2.42)$$

where  $N_{cell}$  is the number of real-space cells in the system, or equivalently number of  $\mathbf{k}$ -points in the BZ. From these, the change in  $\Omega$  with respect to a small change in  $U_{mn}(\mathbf{k})$  can be calculated as a function of  $M_{mn}^{\mathbf{k}, \mathbf{b}}$  to minimize the localization functional. In 1D there is a unique gauge that minimizes the spread functional of the WFs [8]. These maximally localized WFs are eigenfunctions of the band-projected position operator  $PzP$ , where  $P = \sum_{nk} |\psi_{nk}\rangle \langle \psi_{nk}|$  is the projection operator onto the occupied bands. In 2D and 3D, on the other hand, the WFs cannot be maximally localized in all directions simultaneously, because the operators  $PxP$ ,  $PyP$ , and  $PzP$  do not commute and it is not possible to choose the WFs to be simultaneous eigenfunctions of all three. Instead, a compromise can be achieved through an iterative procedure that localizes the WFs in all directions as much as possible [8].

## 2.5 Tight-binding Approximation

In the tight-binding approximation the crystal states are expanded in terms of the atomic orbitals of the composing atoms. Let  $\phi_{\mu i}(\mathbf{r} - \mathbf{R} - \mathbf{t}_\mu)$  indicate an atomic orbital in the unit cell  $\mathbf{R}$ , where  $\mathbf{t}_\mu$  is the location of atom  $\mu$  in home unit cell. Bloch-like basis functions can be constructed as

$$\chi_i^{\mathbf{k}}(\mathbf{r}) = \sum_{\mathbf{R}} e^{i\mathbf{k} \cdot (\mathbf{R} + \mathbf{t}_\mu)} \phi_{\mu i}(\mathbf{r} - \mathbf{R} - \mathbf{t}_\mu). \quad (2.43)$$

The crystal wave function of energy band  $n$  is then expanded as

$$\psi_{n\mathbf{k}} = \sum_{\mathbf{i}} C_i^{n\mathbf{k}} \chi_i^{\mathbf{k}}. \quad (2.44)$$

From the eigenvalue Eq. 2.26 and the application of the variational principle we can calculate the crystal eigenvalues and eigenfunctions from the determinantal compatibility equation

$$\| \langle \chi_i^{\mathbf{k}} | H | \chi_j^{\mathbf{k}} \rangle - E \langle \chi_i^{\mathbf{k}} | \chi_j^{\mathbf{k}} \rangle \| = 0. \quad (2.45)$$

The matrix elements of the Hamiltonian

$$H_{ij}^{\mathbf{k}} = \langle \chi_i^{\mathbf{k}} | H | \chi_j^{\mathbf{k}} \rangle, \quad (2.46)$$

can be evaluated numerically. However, the tight-binding method is frequently used in a semi-empirical way in which the basis orbitals are considered to be orthonormal

$$\langle \phi_{\mu i}(\mathbf{r} - \mathbf{R} - \mathbf{t}_{\mu}) | \phi_{\nu j}(\mathbf{r} - \mathbf{R}' - \mathbf{t}_{\nu}) \rangle = \delta_{ij} \delta_{\mathbf{R}\mathbf{R}'} \delta_{\mu\nu}. \quad (2.47)$$

In this basis Eq. 2.48 turns into

$$\| \langle \chi_i^{\mathbf{k}} | H | \chi_j^{\mathbf{k}} \rangle - E \delta_{ij} \| = 0 \quad (2.48)$$

which can be solved straightforwardly to find energy eigenvalues and eigenvectors. This method will be used in Chapter 4 to describe various topological insulating and semiconducting models.

## 2.6 Geometrical Phases in Matter

Until recently, the main approach for discovering and classifying distinctive phases of matter was based on the underlying symmetries of the system as suggested by Landau. However, new phases of matter have been realized in recent decades which cannot be classified by their symmetries alone. This had led to a new classification criteria based on the topological properties of the ground state wave function. The possible topological phases that can be

realized in a material depend on its symmetries and dimensionality, but one needs to know the topological invariants of the system for distinguishing individual topological classes within each symmetry group.

In 2D insulators with broken time reversal symmetry an integer known as the first Chern number  $C^{(1)}$  specifies the topological class of the system. This topological invariant can be expressed in terms of *Berry connection*  $A_{mn,i}$  or *Berry curvature*  $\Omega_{mn,ij}$  of the periodic Bloch functions defined as

$$A_{mn,i} = i\langle u_{m\mathbf{k}} | \partial_i u_{n\mathbf{k}} \rangle, \quad (2.49)$$

and

$$\begin{aligned} \Omega_{mn,ij} &= \partial_a A_{mn,i} - \partial_b A_{mn,j} - i[A_i, A_j]_{mn} \\ &= i\langle \partial_i u_{m\mathbf{k}} | \partial_j u_{n\mathbf{k}} \rangle - i\langle \partial_j u_{m\mathbf{k}} | \partial_i u_{n\mathbf{k}} \rangle, \end{aligned} \quad (2.50)$$

where  $\partial_i = \partial/\partial k_i$  refers to partial derivative with respect to the wave vector  $k_i$ . The phase evolution of the state  $|u_{n\mathbf{k}}\rangle$  over a closed loop  $\mathcal{C}$  in the BZ is known as the Berry phase and is given by

$$\phi_n = \oint_{\mathcal{C}} \mathbf{A}_n \cdot d\mathbf{k}, \quad (2.51)$$

or equivalently

$$\phi_n = \oint_{\mathcal{S}} \boldsymbol{\Omega}_{nn} \cdot d\mathcal{S}_c, \quad (2.52)$$

where  $\mathcal{S}_c$  is the area defined by the closed loop  $\mathcal{C}$ . In general, integral of the Berry curvature on a closed surface is guaranteed to be a  $2\pi$  multiple of an integer. This integer is the first Chern number, which we will denote by  $C$  for simplicity. The BZ for any 2D lattice-periodical Hamiltonian is a closed surface, therefore

$$C_n = \frac{1}{2\pi} \oint_{BZ} \boldsymbol{\Omega}_{nn} \cdot d\mathcal{S}_c, \quad (2.53)$$

where  $C_n$  is the Chern number associated with band  $n$ . If the system has multiple occupied bands then the sum of Chern numbers associated with occupied bands will be topologically invariant. In other words, if the system is evolved adiabatically, as long as the insulating gap of the insulator remains open the total Chern number associated with it remains intact.

An insulator with nonzero Chern number behaves like an integer quantum Hall system but without any external magnetic field; such a system is called a quantum anomalous Hall (QAH) or Chern insulator. Thouless *et al.* [9] showed that this topological invariant determines the quantized Hall conductivity in a 2D insulators via

$$\sigma_{xy} = C \frac{e^2}{h}. \quad (2.54)$$

In a 3D insulator with broken time reversal symmetry, a Chern number can be calculated for each 2D projected BZ, e.g.  $k_x$ - $k_y$  plane. Therefore, the topological phase of a 3D insulator is specified by a set of three Chern numbers in the absence of time reversal symmetry.

In 2D time reversal invariant insulators the Chern number vanishes, but there is an additional topological invariant with two possible values,  $\nu = 0$  or  $1$ . An insulator with  $\nu = 1$  is known as a 2D  $Z_2$  insulator or a quantum spin Hall insulator. In 3D, a set of four  $Z_2$  invariants determines the topological phase of time reversal invariant insulators. A Wannier representation is not possible in a Chern insulator, but Hybrid WFs which are localized in only one direction are well defined in all dimensions and topological classes. We introduce this representation in chapter 3 and show how topological properties of different insulators can be visualized in this representation.

## Chapter 3

### Topological Aspects of Wannier Charge Centers

Since the work of Thouless *et al.* [9] relating the Chern number to the integer quantum Hall effect, there has been great interest in insulators with topologically non-trivial band structures. In time-reversal invariant insulators, the first Chern number vanishes, but topologically non-trivial band structures can still emerge in systems with strong spin-orbit coupling [1, 10–12] or crystal point group symmetries [13]. These topological phases are classified by a series of  $Z_2$  invariants. In two dimensions, a single  $Z_2$  invariant distinguishes a quantum spin Hall system from a trivial 2D insulator, while in three dimensions, a total of four  $Z_2$  invariants  $[\nu_0, \nu_1, \nu_2, \nu_3]$  are needed to classify the trivial, weak, and strong topological phases which can emerge. The topologically non-trivial phases are gapped in the bulk, like trivial insulators, but they are required to have robust metallic states on the edge (2D) or surface (3D). These surface states provide the strongest experimentally accessible signature of insulators with non-trivial topology [14–21]. However, for reasons of both computational efficiency and theoretical clarity, it is preferable to be able to calculate and understand the topological phases of insulators purely from bulk calculations.

There have been several previously proposed methods for calculating  $Z_2$  invariants. In principle, it is possible to calculate them by integrating the Berry connection on half of the Brillouin zone (BZ) [22], but this method requires fixing the gauge of the wavefunctions, which is challenging in numerical calculations. In the special case of a centrosymmetric crystal, the  $Z_2$  invariants can be calculated simply by considering the parity eigenvalues of the occupied electronic states at the time-reversal-invariant (TRI) momenta. The concepts discussed in this chapter are closely related to a recently developed method which is both

general (not limited to crystals with special symmetries) and computationally efficient [23, 24]. This method relies on the use of hybrid WFs, which provide an alternative to the Bloch representation of the occupied band subspace. By following the evolution of hybrid WFs around a closed loop in the BZ, we can describe the adiabatic, unitary evolution of the occupied Bloch bands. The partner switching of these Wannier charge centers (WCC) around a closed loop, which describes a pumping of “time-reversal polarization,” has been employed to calculate the  $Z_2$  invariants in TRI insulators [23–26].

In this Chapter, we focus on the topological properties of WCCs in 3D materials, which are functions of momentum  $\mathbf{k}$  in two dimensions and can be plotted as sheets over the 2D BZ. Although a knowledge of the behavior of the WCCs on the TRI planes in the BZ is already sufficient for determining the topological phase of the insulator, the more general behavior of WCCs sheets in different topological phases, including the crystalline topological phase, can provide new insights into the origin and properties of these phases. In addition, unlike the surface states, the behavior of these sheets is independent of surface termination and depends purely on the bulk wavefunctions, allowing for a simpler picture of many properties. In Sec. 3.1 we define the WCC sheets and explain how to construct them. In Sec. 3.2 we discuss the symmetry and topological properties of WCC sheets and establish the bulk-boundary correspondence between the surface energy bands and bulk WCCs. In Sec. 3.3 we review the modern theory of polarization briefly and show the connection between WCCs and the Berry phases of Bloch functions as they are carried around the BZ. We also explain how electric polarization can be calculated in insulators with nontrivial topology.

### 3.1 Wannier Charge Centers

Insulators for which the occupied bands are characterized by a nonzero Chern number are known as “Chern” or QAH insulators. In this case, it is well-known that there is a topological obstruction to the construction of exponentially localized WFs [27, 28]. The vanishing of the Chern number in TRI insulators guarantees the existence of localized

WFs, but special care needs to be taken in choosing the gauge for  $Z_2$ -odd insulators, as the localized WFs can only be constructed in a gauge which does not let them come in time-reversal pairs [29].

The fact that there is never a topological obstruction to the construction of WFs in 1D suggests that a convenient strategy for higher dimensions may be to construct “hybrid WFs” that are Wannier-like in 1D and Bloch-like in the remaining dimensions [8, 30]. Choosing the  $\hat{z}$  direction for Wannierization in 3D, these take the form

$$|W_{nl_z}(k_x, k_y)\rangle = \frac{1}{2\pi} \int dk_z e^{i\mathbf{k}\cdot(\mathbf{r}-l_z c\hat{z})} |u_{n,\mathbf{k}}\rangle \quad (3.1)$$

where  $l_z$  is a layer index and  $c$  is the lattice constant along  $\hat{z}$ . Since there is a unique construction of maximally localized WFs in 1D, these are easily constructed at each  $(k_x, k_y)$ , regardless of whether the system is a normal insulator or a Chern,  $Z_2$ , crystalline, or any other kind of TI. The charge center of these hybrid WFs along the localized direction  $\bar{z}_n$  is defined as the expectation value  $\bar{z}_n(k_x, k_y) = \langle W_{n0} | \hat{z} | W_{n0} \rangle$  of the position operator  $\hat{z}$  along this direction for the WF in the home unit cell  $\mathbf{R} = 0$ . These WCCs, which are eigenvalues of the  $PzP$  operator, have been useful in defining the polarization in 2D Chern insulators [31], understanding polarization in 3D layered insulators [32], and calculating the  $Z_2$  topological invariants in TRI insulators [23]. Their sum over occupied bands also gives the “polarization structure” describing the Berry-phase contribution to the electric polarization as a function of  $\mathbf{k}$  in the 2D BZ [33].

It is well known that the nontrivial topology of Chern,  $Z_2$ , and crystalline TIs is reflected in a corresponding nontrivial connectivity of the surface energy bands. While  $k_z$  is clearly no longer a good quantum number for a surface normal to  $\hat{z}$ ,  $k_x$  and  $k_y$  are still conserved, so that if surface states appear in the bulk energy gap, their energy dispersions  $\epsilon_n(k_x, k_y)$  are good functions of momenta in the surface BZ. In a similar way, the WCCs  $\bar{z}_n(k_x, k_y)$  can be plotted over the same 2D BZ, where the Wannierized real-space direction plays a role



analogous to the surface normal. Unlike the surface states  $\epsilon_n(k_x, k_y)$ , the WCCs  $\bar{z}_n(k_x, k_y)$  depend only on bulk properties. However, they still carry the same kind of topological information as is contained in the surface states, as will be explained in Sec. 3.2.

The WCCs can be obtained from a parallel-transport-based construction [8, 32] in a straightforward way, as explained next.

### 3.1.1 Construction

A cell-periodic Bloch state  $|u_{\mathbf{k}}\rangle$  belonging to an isolated band can be parallel transported to  $|u_{\mathbf{k}+\mathbf{b}}\rangle$  by choosing the phase of the latter such that the overlap  $\langle u_{\mathbf{k}}|u_{\mathbf{k}+\mathbf{b}}\rangle$  is real and positive, so that the change in the state is orthogonal to the state itself. If this is carried out repeatedly for a  $k$ -point string extending along the  $k_z$  direction by a reciprocal lattice vector  $\mathbf{G} \parallel \hat{z}$ , then once the phase of the initial  $|u_{\mathbf{k}_0}\rangle$  is chosen, the phase of each subsequent state, including the final  $|u_{\mathbf{k}_0+\mathbf{G}}\rangle$ , is determined by this parallel-transport procedure. The phase of the last state on the string is then compared with the one  $|\tilde{u}_{\mathbf{k}_0+\mathbf{G}}\rangle$  obtained by applying the periodic gauge condition  $|\psi_{\mathbf{k}_0+\mathbf{G}}\rangle = |\psi_{\mathbf{k}_0}\rangle$ , i.e.,  $\tilde{u}_{\mathbf{k}_0+\mathbf{G}}(\mathbf{r}) = \exp(-i\mathbf{G} \cdot \mathbf{r}) u_{\mathbf{k}_0}(\mathbf{r})$ , and the phase mismatch  $U = \langle u_{\mathbf{k}_0+\mathbf{G}}|\tilde{u}_{\mathbf{k}_0+\mathbf{G}}\rangle$  is computed. For a  $k$ -point string at  $\mathbf{k}_\perp$  in the 2D BZ, this yields the Berry phase  $\phi(\mathbf{k}_\perp) = -\text{Im} \ln U(\mathbf{k}_\perp)$  and the WCC  $\bar{z}(\mathbf{k}_\perp) = (c/2\pi) \phi(\mathbf{k}_\perp)$ , where  $c$  is the lattice constant along  $\hat{z}$ . If the parallel-transported states themselves are not needed, the same result can be obtained more straightforwardly by computing  $\phi = -\text{Im} \ln \prod \langle u_{\mathbf{k}}|u_{\mathbf{k}+\mathbf{b}}\rangle$ , where the product is carried out along the string and the phases are chosen arbitrarily except for the periodic gauge condition that fixes the phase of the first and last  $k$ -points in relation to each other.

In the multiband case, where  $n$  occupied bands are treated as a group regardless of possible internal crossings or degeneracies, the corresponding “non-Abelian” Berry phases  $\phi_n$  can be determined by generalizing this procedure in terms of  $n \times n$  matrix operations. For each pair of neighboring points along the string, the matrix  $M_{mn}^{(\mathbf{k}, \mathbf{k}+\mathbf{b})} = \langle u_{m\mathbf{k}}|u_{n, \mathbf{k}+\mathbf{b}}\rangle$  is computed and subjected to the singular value decomposition  $M = V\Sigma W^\dagger$ , where  $V$  and  $W$

are unitary and  $\Sigma$  is real and diagonal (typically, nearly unity). Again, the states at the end point  $\mathbf{k}_0 + \mathbf{G}$  are predetermined by those at the start  $\mathbf{k}_0$  by the periodic gauge condition. We can then identify  $U(\mathbf{k}, \mathbf{k} + \mathbf{b}) = VW^\dagger$  as the unitary rotation from  $\mathbf{k}$  to  $\mathbf{k} + \mathbf{b}$ , and the global unitary rotation matrix  $\Lambda(\mathbf{k}_\perp) = \prod U(\mathbf{k}, \mathbf{k} + \mathbf{b})$  is constructed as the product of these along the string. Being unitary, its eigenvalues  $\lambda_n$  are unimodular, and we can identify the non-Abelian Berry phases (also known as Wilson loop eigenvalues) as  $\phi_n(\mathbf{k}_\perp) = -\text{Im} \ln \lambda_n(\mathbf{k}_\perp)$ . The WCCs are then just

$$\bar{z}_n(\mathbf{k}_\perp) = \frac{c}{2\pi} \phi_n(\mathbf{k}_\perp). \quad (3.2)$$

As discussed in Ref. [8], this procedure gives the centers of the maximally-localized Wannier functions in 1D algebraically, without the need for any iterative localization procedure; we just repeat this procedure for each  $\mathbf{k}_\perp$  to construct the WCC sheets.

### 3.2 Bulk-boundary Correspondence

A major theme of this chapter is to show how the WCC sheet structure  $\bar{z}_n(\mathbf{k}_\perp)$  shares many qualitative features with the surface energy bandstructure  $\epsilon_n(\mathbf{k}_\perp)$ , a manifestation of the bulk-boundary correspondence which relates the boundary modes to the topological character of the bulk. The WCCs  $\bar{z}_n(\mathbf{k}_\perp)$  have the crucial advantage that they can be used to deduce the topological properties of the bulk from bulk properties alone.

In this subsection we show that the WCC sheet structure obeys all of the symmetries that are found in the surface energy bandstructure, and sometimes more. In particular, when TR is present, the Kramers degeneracies found at the 2D time-reversal invariant momenta (TRIM) in the surface energy band structure also necessarily appear in the WCC sheet structure. We also demonstrate the bulk-boundary correspondence by sketching a physical argument as to why the topological connectedness of the WCC sheets mirrors that of the surface bandstructure, providing access to the topological indices in a similar way.

### 3.2.1 Symmetry

To review, we consider a crystalline insulator with  $\hat{z}$  taken along a primitive reciprocal lattice vector, and let  $k_{\parallel}$  and  $\mathbf{k}_{\perp}$  denote the wavevectors parallel and perpendicular to  $\hat{z}$  respectively. We then consider the surface bandstructure  $\epsilon_n(\mathbf{k}_{\perp})$  for a  $1 \times 1$  (unreconstructed) surface that has been cut normal to  $\hat{z}$ , where  $n$  labels energy eigenstates lying in the bulk projected band gap. We also consider the WCC sheets  $\bar{z}_n(\mathbf{k}_{\perp})$  constructed as detailed in Sec. 3.1.1, where  $n$  labels the sheets with  $-c/2 \leq z \leq c/2$  in one unit cell along  $z$ . In both cases,  $\mathbf{k}_{\perp}$  resides in the same 2D surface BZ (both functions have the same periodicity in  $\mathbf{k}_{\perp}$ ).

An element  $S = \{G|\boldsymbol{\tau}\}$  of the full space group  $\mathcal{S}$  is composed of a generalized rotation  $G$  (possibly improper, and possibly containing TR) followed by a possible fractional translation  $\boldsymbol{\tau}$  (in non-symmorphic crystals), in addition to lattice translations; the full point group  $\mathcal{G}$  is composed of all of the  $G$  appearing in the space-group elements.

The symmetry of the WCC sheets is controlled by the reduced space group  $\mathcal{S}_W \subseteq \mathcal{S}$  and the corresponding point group  $\mathcal{G}_W \subseteq \mathcal{G}$  defined by restricting the list of  $G$ 's to those that map  $\hat{z}$  onto  $\pm\hat{z}$ . For such operations, let  $G = KT_zG_{\perp}$  where  $G_{\perp}$  is the in-plane rotation (possibly improper),  $T_z$  is either the identity or the simple mirror  $M_z$ , and  $K$  is either the identity or TR. Then a space-group element  $\{G|\boldsymbol{\tau}\} \in \mathcal{S}_W$  must transform a hybrid Wannier function  $W_n(\mathbf{k}_{\perp})$  into another hybrid Wannier function  $W_{n'}(\pm G\mathbf{k}_{\perp})$ , with the Wannier center transformed as

$$\bar{z}_{n'}(\pm G_{\perp}\mathbf{k}_{\perp}) = T_z\bar{z}_n(\mathbf{k}_{\perp}) + \tau_z, \quad (3.3)$$

where the minus sign applies if  $G$  contains TR.

The symmetry of the surface bandstructure  $\epsilon_n(\mathbf{k}_{\perp})$ , on the other hand, is associated with the space group  $\mathcal{S}_S \subseteq \mathcal{S}_W$  with the additional constraints that its elements do not reverse  $\hat{z}$  to  $-\hat{z}$  and do not contain partial translations  $\tau_z$  along  $\hat{z}$ . Then for any element

$G = KG_{\perp}$  in the corresponding point group  $\mathcal{G}_S$  we have that

$$\epsilon_n(\pm G_{\perp} \mathbf{k}_{\perp}) = \epsilon_n(\mathbf{k}_{\perp}) \quad (3.4)$$

where again the minus sign applies if TR is involved.

Since  $\mathcal{G}_S \subseteq \mathcal{G}_W$ , it follows from Eq. (3.3) that the WCC sheets also obey

$$\bar{z}_n(\pm G_{\perp} \mathbf{k}_{\perp}) = \bar{z}_n(\mathbf{k}_{\perp}) \quad (3.5)$$

for any  $G \in \mathcal{G}_S$ . Thus, the WCC sheets show at least as much symmetry as the surface bandstructure. If the space group contains symmetry elements that reverse the  $z$  axis, then there is an additional symmetry  $\bar{z}_n(\pm G_{\perp} \mathbf{k}_{\perp}) = -\bar{z}_n(\mathbf{k}_{\perp})$  associated with these elements, or if it contains glide or screw operations along  $\hat{z}$ , then also  $\bar{z}_n(\pm G_{\perp} \mathbf{k}_{\perp}) = \bar{z}_n(\mathbf{k}_{\perp}) + \tau_z$ . These additional WCC symmetries have no counterpart in the surface bandstructure.

Finally, we note that TR symmetry plays a similar role for the WCC sheets as for the surface energy bandstructure. Specifically, for any  $G \in \mathcal{G}_S$ , a Kramers degeneracy is enforced whenever  $G_{\perp} \mathbf{k}_{\perp} = -\mathbf{k}_{\perp}$  (modulo a reciprocal lattice vector), due to the antiunitary nature of the TR operation. In particular, if TR by itself is a symmetry, then the WCC sheets and the surface energy bands are guaranteed to touch and form Kramers pairs at all of the TRIM. Additionally, if  $C_2^Z \otimes \text{TR}$  is a symmetry, then both the WCCs and surface energy bands are Kramers degenerate everywhere in the 2D BZ.

### 3.2.2 Topology

Just as the symmetries of the surface bandstructure are replicated in the WCC sheet structure, a similar principle applies to the topological properties. This will be amply illustrated by the examples to follow, but we give here a sketch of a general argument that this should be so.

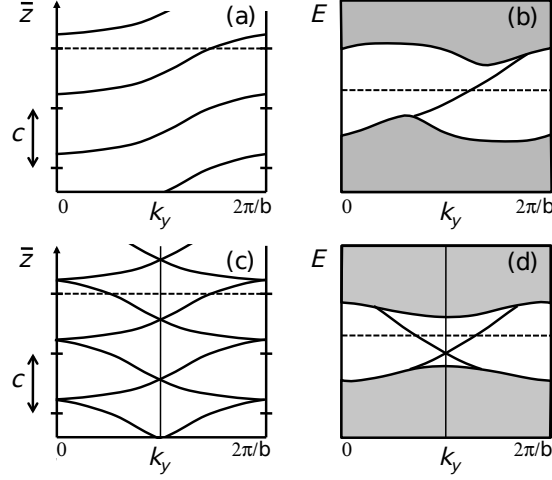


Figure 3.1: (a) Flow of Wannier charge centers along  $\hat{z}$  vs.  $k_y$  for a 2D Chern insulator. (b) Flow of surface energy bands vs.  $k_y$  for a 2D Chern insulator. (c-d) Same, but for a 2D  $Z_2$ -odd (quantum spin Hall) insulator. Dashed lines are arbitrary reference positions in (a) and (c), or Fermi energies in (b) and (d).

For simplicity, consider first a 2D Chern insulator lying in the  $y$ - $z$  plane with one occupied band carrying a Chern number  $C = +1$ . Then the WCC  $\bar{z}(k_y)$  undergoes a shift by  $c$  as  $k_y$  is adiabatically carried from  $k_y = 0$  to  $k_y = 2\pi/b$  (assuming a rectangular  $b \times c$  unit cell), as shown in Fig. 5.2(a). This means that one electron is adiabatically pumped by  $c\hat{z}$  during one cycle of  $k_y$  around the 1D BZ. If the edge bandstructure remained gapped throughout the cycle, this would lead to a contradiction, since by conservation of charge one extra electron per surface unit cell would reside on the top edge at the end of the cycle. However, the starting and ending point are physically identical, so the edge charge must be the same. This paradox can only be avoided if there is a surface state that emerges from the valence band, rises through the gap, and disappears into the conduction band during one cycle, as shown in Fig. 5.2(b). In this case, the sudden loss of one electron that occurs when the surface band crosses the Fermi energy compensates for the gradual gain of one electron from the pumping, restoring charge conservation. In other words, we conclude that the edge bandstructure has a state crossing the gap if and only if the WCC structure has a WCC that winds by one unit during the cycle.

More generally, for an insulator with  $N$  occupied bands, if  $\sum_n^N \bar{z}_n/c$  winds by Chern

integer  $C$  during the cycle, the number of up-crossing minus the number of down-crossing surface bands in the edge bandstructure must equal  $C$  in order to satisfy charge conservation. The argument also generalizes to 3D Chern insulators. If the WCC sheet structure is computed in the  $\hat{z}$  direction, the Chern indices along  $x$  and  $y$  (that is, corresponding to Berry curvatures  $\Omega_{yz}$  and  $-\Omega_{xz}$ ) are evident in the  $z$ -windings of the WCC sheets as  $\mathbf{k}_\perp$  is cycled in the  $k_y$  and  $k_x$  directions respectively. In each case, a similar surface state crossing necessarily must also occur in the surface bandstructure, following the arguments given above.

Turning now to TR-invariant insulators, the Chern number always vanishes, being odd under TR-symmetry, but the WCC structure and surface band structure still share their topological properties. Recall that TR symmetry leads to double degeneracy in both the WCCs and the surface energy bands at TRI points in BZ. Here we show that the WCCs connect the TRI points in the same manner as the energy bands do, and can be used in a similar way to deduce the  $Z_2$  index of the system.

Consider the simple case of a 2D  $Z_2$  insulator in the  $y$ - $z$  plane with two occupied bands. The TR symmetry relates the WCCs and the surface energy bands in the second half of the BZ to the ones in the first half by  $z(k_y) = z(2\pi/b - k_y)$  and  $\epsilon(k_y) = \epsilon(2\pi/b - k_y)$ , as illustrated in Figs. 5.2(c-d), so we only need to study their behavior in the first half  $[0, \pi/b]$ . In the absence of spin-mixing terms, the system decouples into two independent insulators with equal and opposite Chern numbers for spin-up and spin-down electrons. If these are  $\pm 1$ , the system is  $Z_2$ -odd. This implies both that the WCCs must switch partners as  $k_y$  evolves from 0 to  $\pi/c$ , as shown in Fig. 5.2(c), and that the surface energy bands zigzag, as shown in Fig. 5.2(d). More precisely, an arbitrary horizontal line in Fig. 5.2(c) intersects the WCC curves just once (or, in general, an odd number of times) in the half-BZ, as does an arbitrary Fermi level for the surface energy bands in the half-BZ in Fig. 5.2(d). One unit of up spin, relative to down spin, is pumped to the edge during this half-BZ evolution, corresponding to the “TR polarization pumping” discussed by Fu and Kane [25]. For a

$Z_2$ -even insulator, the number of crossings is, instead, an even integer (typically zero) for both the WCCs and the surface energy bands.

In more realistic  $Z_2$  insulators, the spin-orbit interaction mixes up and down spins such that the energy bands are no longer perfectly spin-polarized and a spin-Chern classification of the system is no longer guaranteed. However, as long as the bulk energy gap remains open as these spin-mixing terms are adiabatically turned on, neither the even/oddness of the number of WCC crossings, nor the even/oddness of the number of surface energy band crossings, can change. Therefore, it remains true that the  $Z_2$  index deduced from the WCC evolution is the same as that deduced from the surface energy bands, i.e., they both contain the same topological information.

The weak and strong topological indices of a 3D TR-invariant insulator can be determined from the 2D indices on the six TRI faces  $\tilde{k}_j = \{0, \pi\}$  of the 3D BZ (where  $\tilde{k}_x = k_x a$ ,  $\tilde{k}_y = k_y b$ ,  $\tilde{k}_z = k_z c$ ), which are negative if the WCCs have a non-trivial connectedness on that face and positive otherwise. Assigning an index  $\nu(\tilde{k}_i)$  to each of these faces, the four  $Z_2$  invariants  $[\nu_0, \nu_1, \nu_2, \nu_3]$  that uniquely specify the topological phase of a TR-invariant insulator can be determined from these  $\nu(\tilde{k}_i)$  as follows. The three  $\nu_i \equiv \nu(\tilde{k}_i = \pi)$ , which are known as weak topological indexes, are determined from the WCC behavior on the  $\tilde{k}_i = \pi$  faces, while the strong topological index  $\nu_0 \equiv \nu(\tilde{k}_i = 0)\nu(\tilde{k}_i = \pi)$  is only negative if the topological indices of opposing TRI faces are opposite, i.e., if the WCCs on the  $\tilde{k}_i = 0$  and  $\tilde{k}_i = \pi$  faces have different behavior. The indices could similarly be deduced from the behavior of the surface energy bands. For both the WCC and surface problems, we have to choose a particular axis  $\hat{z}$  to define  $\bar{z}$  or as the surface normal, and in this case we are only sensitive to four of the six TRI-face indices, defining whether WCCs (or surface states) zigzag or not along the four edges of the quarter 2D BZ. This determines the strong index  $\nu_0$  and two of the three weak indices ( $\nu_1$  and  $\nu_2$ ); the procedure has to be repeated with a different choice of axis to obtain the third weak index  $\nu_3$ .

In summary, we expect that the flow and connectedness of the WCC sheets and the

surface energy bands should always show the same qualitative features. Not surprisingly, similar considerations apply to the case of crystalline TIs as well. Numerous examples will be presented in the next chapter which amply illustrate this bulk-boundary correspondence between the WCC sheets and surface energy bands. In Chapter 5 we employ the WCC sheets to illustrate the pumping of Chern-Simons Axion coupling in an adiabatic loop defined by the second Chern number.

### 3.3 Berry Phase and Electric Polarization

The WCCs provide a local description of polarization as well as dielectric and polar responses in crystals. The electric dipole of molecular systems can be calculated straightforwardly from the matrix elements of position operator between the occupied Hamiltonian eigenstates  $\psi_i$

$$\mathbf{d} = -e \sum_i \langle \psi_i | \mathbf{r} | \psi_i \rangle. \quad (3.6)$$

This definition cannot be generalized to crystalline systems since the Hamiltonian eigenstates in a periodic infinite system are extended over all space and the position matrix elements are not well defined over such states. The modern theory of polarization addressed this issue by realizing that only the differences of polarization are experimentally measurable. In this approach the differences of polarization are calculated between two insulating states that are connected by an adiabatic switching process

$$\Delta \mathbf{P} = \mathbf{P}(\Delta t) - \mathbf{P}(0) = \int_0^{\Delta t} dt \mathbf{j}(t), \quad (3.7)$$

where  $\mathbf{j}(t)$  is the transient macroscopic current that flows through the insulating sample during the adiabatic evolution. Independently, King-Smith and Vanderbilt [34], and Resta [35] showed that  $\mathbf{P}(\Delta t)$  and  $\mathbf{P}(0)$  are in fact proportional to the single-point Berry phase of



occupied states and the electronic contribution to electric polarization is given by

$$\mathbf{P}_{\text{el}} = -\frac{e}{(2\pi)^3} \sum_n \int_{BZ} d\mathbf{k} \langle u_{n\mathbf{k}} | i\nabla_{\mathbf{k}} | u_{n\mathbf{k}} \rangle, \quad (3.8)$$

where  $u_{n\mathbf{k}}$  are occupied periodic Bloch functions that are smooth functions of  $\mathbf{k}$ .

The polarization finds an even simpler form in Wannier representation. Let us construct WFs from smooth periodic functions  $u_{n\mathbf{k}}$ . Then the WCCs in home unit cell are

$$\mathbf{r}_n = \langle W_n(\mathbf{0}) | \mathbf{r} | W_n(\mathbf{0}) \rangle = -\frac{V}{(2\pi)^3} \int_{BZ} d\mathbf{k} \langle u_{n\mathbf{k}} | i\nabla_{\mathbf{k}} | u_{n\mathbf{k}} \rangle. \quad (3.9)$$

Now it is obvious that the polarization in Eq.3.8 is simply the sum of WCCs of occupied bands

$$\mathbf{P}_{\text{el}} = -\frac{e}{V} \sum_n \mathbf{r}_n. \quad (3.10)$$

In this basis, any physical change in the system, such as external fields or displacement of atoms, which changes polarization results in a shift in the position of WCCs. It is important to notice that the choice of home unit cell in Wannier representation is arbitrary. Moreover, an arbitrary change of gauge can shift individual WCCs in an arbitrary way. However, the sum of WCCs over occupied space remains invariant modulo a lattice vector  $\mathbf{R}$ . Therefore the polarization defined via Eq. 3.10 is only well defined modulo a quantum  $e\mathbf{R}/V$ , which is consistent with the fact only a change in polarization is physically meaningful.

### 3.3.1 Electric Polarization in Nontrivial Insulators

It is well known that the electric polarization is not well defined in metals. In a Chern insulator with metallic edge states exponentially localized WFs cannot be constructed, however the Berry phase formulation of polarization can still be generalized to insulators with non-zero Chern number as Coh and Venderbilt showed [31]. In this case, spacial care needs to be taken in calculating the integrated bulk current arising from an adiabatic

evolution and Eq. 3.11 turns to

$$\Delta \mathbf{P}_{[\mathbf{k}_0]} = \mathbf{P}_{[\mathbf{k}_0]}(\Delta t) - \mathbf{P}_{[\mathbf{k}_0]}(0) = \int_0^{\Delta t} dt \mathbf{j}(t). \quad (3.11)$$

Here  $[\mathbf{k}_0]$  indicates the reciprocal-space unit cell with origin at  $\mathbf{k}_0$ . This reciprocal-space unit cell must be the same on both  $\mathbf{P}_{[\mathbf{k}_0]}(\Delta t)$  and  $\mathbf{P}_{[\mathbf{k}_0]}(0)$  terms.

A  $Z_2$ -odd insulators without spin-mixing terms can be decoupled into two Chern insulators with spin up and spin down. These decoupled Chern insulators are related to each other by time-reversal symmetry, therefore localized WFs can only be constructed in a gauge which does not allow them to come in time-reversal pairs. The time-reversal invariance of Hamiltonian in this gauge might not be obvious but the WFs are still exponentially localized and define the electric polarization via Eq. 3.10 [23].

## Chapter 4

### Topological Insulating and Semiconducting Phases in 3D

In this Chapter, we study the properties of WCCs in different topological phases in 3D using simple tight-binding (TB) models as well as realistic density-functional theory (DFT) descriptions of known materials. In particular, we use a Haldane-like [36] TB model of spinless electrons on a hexagonal lattice to study the properties of the WCC sheets in a 3D Chern insulator; the model of Fu, Kane, and Mele (FKM) [1] to study the WCCs of trivial, weak, and strong topological phases; and the tetragonal TB model of Fu [13] to study a crystalline TI. The spinless 3D model of Delplace, Li, and Carpentier (DLC) [37] is employed to study the WCC sheets properties in Weyl semimetals. These TB models are described in Sec. 4.1. We then compute the behavior of the WCC sheets in the  $Z_2$ -even  $\text{Sb}_2\text{Se}_3$ , weak  $Z_2$ -odd  $\text{KHgSb}$ , and strong  $Z_2$ -odd  $\text{Bi}_2\text{Se}_3$  insulators using first-principles DFT calculations. These materials and their crystal structure are described in Sec. 4.2, and the details of our computational approach are presented in Sec. 4.2.1.

#### 4.1 Tight-binding Models

A TB model of a 2D Chern insulator was first introduced by Haldane on a honeycomb lattice. [36] This spinless model is constructed by starting with real first and second-neighbor hoppings, but the time-reversal symmetry is then broken by introducing local magnetic fluxes in a pattern that respects the symmetry of the lattice and sums to zero in each unit cell. This magnetic flux has the effect of multiplying the second-neighbor hoppings by a unimodular phase factor  $\lambda = e^{i\varphi}$ . We then stack these 2D layers in the normal direction to

make a 3D TB model of a Chern insulator:

$$\begin{aligned}
H = & t_1 \sum_{l, \langle ij \rangle} c_{il}^\dagger c_{jl} + t_2 \sum_{l, \ll ij \gg} \lambda c_{il}^\dagger c_{jl} \\
& + t'_1 \sum_{li} c_{il}^\dagger c_{i, l+1} + t'_2 \sum_{l, \langle ij \rangle} c_{il}^\dagger c_{j, l+1} + \text{H.c.}
\end{aligned} \tag{4.1}$$

Here  $l$  is the layer index, single and double brackets label first- and second-neighbor in-plane pairs with hoppings  $t_1$  and  $t_2$  respectively, and  $t'_1$  and  $t'_2$  are (real) vertical and nearest-diagonal interlayer hoppings respectively. The hoppings included explicitly in the second term of Eq. (4.1) are those for clock-wise hoppings around the hexagon; counterclockwise ones are accounted for by the Hermitian conjugation and have phases  $\lambda^*$ . With  $t_1 = -1.0$ ,  $t'_1 = -0.45$ ,  $t_2 = 0.15$ ,  $t'_2 = 0.015$ , and  $\varphi = 0.5\pi$  the occupied band has a Chern number of one.

The FKM model [1] is a four-band TB model of  $s$  states on a diamond lattice in 3D with a spin-orbit interaction, and takes the form

$$H = t \sum_{\langle ij \rangle} c_i^\dagger c_j + i(8\lambda_{\text{so}}/a^2) \sum_{\ll ij \gg} c_i^\dagger \mathbf{s} \cdot (\mathbf{d}_{ij}^1 \times \mathbf{d}_{ij}^2) c_j. \tag{4.2}$$

Here the first and second terms describe spin-independent first-neighbor and spin-dependent second-neighbor hoppings respectively;  $\lambda_{\text{so}}$  is the spin-orbit strength, and  $a$  is the cubic lattice constant, which is set to one. The second-neighbor hopping between sites  $i$  and  $j$  depends on spin and on the unit vectors  $\mathbf{d}_{ij}^{1,2}$  describing the two first-neighbor bonds that make up the second-neighbor hop. For  $t = 1$  and  $\lambda_{\text{so}} = 0.125$ , the model has a gap closure at the high symmetry X point in the Brillouin zone.

By varying the relative strength of the nearest-neighbor bond in the [111] direction,  $t_{111} = t(1 + \alpha)$ , the cubic symmetry is broken and the system can be switched between trivial, weak and strong topological phases, as shown in Table 4.1. These insulating phases are separated from each other by gap closures at  $\alpha = -4$ ,  $-2$ ,  $0$ , and  $2$ . For  $\alpha < -4$  and  $\alpha > 2$ , the  $t_{111}$  bond is stronger than the other bonds and the system can be adiabatically

$\alpha$	$[\nu_0; \nu_1 \nu_2 \nu_3]$	Topological phase
$(-\infty, -4)$	$[+; + + +]$	Trivial insulator
$(-4, -2)$	$[-; - - -]$	Strong topological insulator
$(-2, 0)$	$[+; + + -]$	Weak topological insulator
$(0, 2)$	$[-; + + -]$	Strong topological insulator
$(2, \infty)$	$[+; + + +]$	Trivial insulator

Table 4.1: Topological phase of the FKM model [1] as a function of parameter  $\alpha$  specifying the relative strength of the  $[111]$  bond according to  $t_{111} = t(1 + \alpha)$ .

transformed to a system of dimers, which is topologically equivalent to a trivial atomic insulator. For  $-2 < \alpha < 0$ , on the other hand, the  $t_{111}$  bond is weaker than the others, and the system can be considered as a collection of 2D spin-Hall layers stacked along the  $[111]$  direction. Thus, the system is a weak TI in this range of  $\alpha$ . For  $-4 < \alpha < -2$  and  $0 < \alpha < 2$ ,  $t_{111}$  is stronger than the other first-neighbor bonds, but not strong enough to push the system into the topologically trivial phase. As a result, the 3D KM model is a strong  $Z_2$  TI for these values of  $\alpha$ .

For studying the WCC sheet behavior in a topological crystalline insulator, we adopted the TB model of Fu [13], consisting of a tetragonal lattice with two inequivalent A and B atoms stacked above one another, each carrying  $p_x$  and  $p_y$  orbitals, forming bilayers that we index by  $n$ . The total system Hamiltonian can be written as

$$H = \sum_n (H_n^A + H_n^B + H_n^{AB}), \quad (4.3)$$

where  $H^A$  and  $H^B$  are the contributions describing intralayer hoppings while  $H^{AB}$  describes interlayer ones. The former are given by

$$H_n^X = \sum_{ij} t^X(\mathbf{r}_i - \mathbf{r}_j) \sum_{\alpha, \beta} c_{X\alpha}^\dagger(\mathbf{r}_i, n) e_\alpha^{ij} e_\beta^{ij} c_{X\beta}(\mathbf{r}_i, n) \quad (4.4)$$

and the latter by

$$\begin{aligned}
H_n^{AB} &= \sum_{ij} t'(\mathbf{r}_i - \mathbf{r}_j) \sum_{\alpha, \beta} \left[ c_{A\alpha}^\dagger(\mathbf{r}_i, n) c_{B\alpha}(\mathbf{r}_i, n) + \text{H.c.} \right] \\
&+ t'_z \sum_i \sum_\alpha \left[ c_{A\alpha}^\dagger(\mathbf{r}_i, n) c_{B\alpha}(\mathbf{r}_i, n_1) + \text{H.c.} \right].
\end{aligned} \tag{4.5}$$

Here  $\mathbf{r} = (x, y)$  labels the coordinate in the plane,  $X = \{A, B\}$  labels the sublattice,  $\alpha$  and  $\beta$  label the  $\{p_x, p_y\}$  orbitals, and  $e_\alpha^{ij}$  is cosine of the angle between the bond  $(\mathbf{r}_i - \mathbf{r}_j)$  and orbital  $p_\alpha$ . We choose the nearest- and next-nearest-neighbor hopping amplitudes to be  $t_1^A = -t_1^B = 1$  and  $t_2^A = -t_2^B = 0.5$  in  $H^A$  and  $H^B$ , and  $t'_z = 2$ ,  $t'_1 = 2.5$  and  $t'_2 = 0.5$  in  $H^{AB}$ .

Note that this TB model is spinless, as the spin-orbit coupling plays no role in the non-trivial topology of crystalline TIs. Instead, the topological classification is based on certain crystal point-group symmetries and TRI, leading to robust surface states on those surface that respect the symmetries in question. In the tetragonal Fu model, these topological surface states exist on the (001) surface, where the fourfold  $C_4^z$  rotational symmetry of the crystal is preserved.

To study the properties of WCC sheets in a Weyl semimetal, we employed the spinless TB model of DLC [37], consisting of layers of face-centered square lattice with sublattices A and B. The on-site energies are  $\Delta$  and  $-\Delta$  for the two sublattices. The nearest neighbor hoppings between A and B sublattices are denoted by  $t$ , and the A-A and B-B next nearest hoppings by  $t'$ . Moreover, a magnetic flux pattern is applied to the lattice in a way that it preserves the  $C_{4h}$  symmetry of the lattice and the total flux through each surface of the unit cell is a quanta of the flux quantum  $\phi_0 = h/e$ . As a result each hopping term picks a phase factor and the total the Hamiltonian of the system can be written as

$$\begin{aligned}
H &= \Delta \left( \sum_i c_{Ai}^\dagger c_{Ai} - \sum_i c_{Bi}^\dagger c_{Bi} \right) \\
&+ \left( t \sum_{\langle ij \rangle} e^{i\phi_{ij}} c_{Ai}^\dagger c_{Bj} + t' \sum_{X, \langle\langle ij \rangle\rangle} e^{i\phi'_{ij}} c_{Xi}^\dagger c_{Xj} + \text{H.c.} \right).
\end{aligned} \tag{4.6}$$

where  $X = \{A, B\}$ . With  $\Delta = 2.0$ ,  $t = 1$ , and  $t' = 0.5$ , the 3D bulk bands are gapped except at two Weyl points  $(k_x, k_y, k_z) = (0, 0, \pm \frac{\pi}{2})$ . These Weyl points are related by inversion symmetry and have opposite helicities.

## 4.2 Material Systems

We carry out first-principles calculations of the WCC sheet structure for  $\text{Sb}_2\text{Se}_3$ ,  $\text{KHgSb}$ , and  $\text{Bi}_2\text{Se}_3$  as prototypical realizations of trivial, weak, and strong topological phases, respectively.  $\text{Bi}_2\text{Se}_3$  has a rhombohedral layered structure with space group  $D_{3d}^5(R\bar{3}m)$ . It consists of quintuple layers (QLs) formed by stacking Se and Bi triangular-lattice planes in the order Se-Bi-Se-Bi-Se, with two identical Bi atoms, two identical Se atoms and a third Se atom at the center. These QLs have strong internal covalent bonding, but the interaction between QLs is much weaker, being largely of van der Waals type. The states near the Fermi energy come from the

Bi  $6p$  and Se  $4p$  orbitals. The strong SOC leads to a band inversion at the  $\Gamma$  point and makes this material a strong  $Z_2$  insulator with a band gap of 0.3 eV [16, 38].  $\text{Sb}_2\text{Se}_3$  shares the same rhombohedral layered structure as  $\text{Bi}_2\text{Se}_3$ , but the weaker SOC in this material leaves it in a topological trivial phase.

$\text{KHgSb}$  consists of layers of  $\text{HgSb}$  in a honeycomb lattice, with hexagonal layers of K atoms stuffed between them. In a single layer of  $\text{KHgSb}$ , the valence bands near the Fermi energy are composed of the Hg  $6s$  and Sb  $5s$  and  $5p$  states, while the K  $4s$  band is considerably higher in energy. The strong SOC in the honeycomb  $\text{HgSb}$  layer leads to a band inversion at the  $\Gamma$  point in the 2D BZ and makes an isolated  $\text{KHgSb}$  layer a 2D TI. These 2D TI layers can be stacked along the  $z$  direction to form a 3D lattice, but the inter-layer coupling is very weak and there is little dispersion along the  $\Gamma$ - $Z$  direction. These honeycomb layers can either be stacked in an AA sequence to make a “single-layer” form, or in an ABAB sequence to make a “double-layer” form, where B is rotated by  $60^\circ$  with respect to A. In the latter structure, which is experimentally observed, the primitive cell

contains two honeycomb layers. Thus, two band inversions occur and cancel each other out at  $\Gamma$ , and the same happens at  $Z$ , making the compound a trivial insulator [39, 40]. In the hypothetical single-layered structure, which is proposed as an example of a weak TI [40], there is only one honeycomb layer in the primitive cell, and a single band inversion happens at  $\Gamma$  and another at  $Z$ . Thus single-layered KHgSb can be viewed as a stack of weakly coupled 2D TIs and belongs to the weak  $Z_2$ -odd topological class. Here, we focus on single-layered KHgSb, and we compare its WCC sheets to the weak topological phase of the FKM TB model in Sec. 4.6.

#### 4.2.1 Computational Methods

Our first-principles calculations of WCC sheets are based on DFT calculations using the PBE exchange-correlation functional [41] performed with the Quantum Espresso package [42]. We use fully-relativistic optimized norm-conserving pseudopotentials from the Opium package, with the semicore Bi  $5d$ , Sb  $4d$ , Hg  $5d$ , and K  $3s3p$  states included in the valence. The self-consistent calculations are carried out for the experimental structures using a  $10 \times 10 \times 10$  Monkhorst-Pack [43]  $k$ -mesh. The plane-wave energy cutoff is set to 70 Ry.

In principle one could include all occupied bands in the WCC construction. However, taking Bi<sub>2</sub>Se<sub>3</sub> as an example, the occupied Bi  $5d$  semicore states and the shallow Bi  $6s$  and Se  $4s$  bands have an obvious atomic character and remain well separated from the active valence  $p$  bands, so they are clearly trivial and do not need to be included in the topological analysis. Therefore, we concentrate on constructing WCC sheets only for the remaining upper valence bands. As these are the lowest 18 of the 30 bands of Bi  $6p$  and Se  $4p$  character, we do this by constructing a Wannier representation in this 30-band space using the Wannier90 package [44] to generate an *ab initio* TB Hamiltonian from the DFT calculation. The frozen window in which the first-principles band structure is exactly reproduced extends from 2 eV below to 2 eV above the Fermi level  $E_F$ . From the outer



energy window, which extends to 20 eV above  $E_F$ , 80 Bloch bands are used to produce 30 WFs for the Bi, Sb, and Se  $p$  bands in  $\text{Bi}_2\text{Se}_3$  and  $\text{Sb}_2\text{Se}_3$ . The orbital positions and hopping parameters between them are then used to construct the effective tight-binding Hamiltonians. Similarly, for  $\text{KHgSb}$  we carry out the Wannier construction for the ten Bloch bands of K  $4s$ , Hg  $6s$  and Sb  $5p$  character, of which the bottom six are the highest valence states. The outer window is chosen at 14 eV above  $E_F$  for  $\text{KHgSb}$ , with ten WFs constructed from 20 Bloch bands.

We have implemented the calculation of the WCC sheets into Version 1.6.2 of the open-source PythTB tight-binding code package [45]. The Wannierized Hamiltonians are imported into the PythTB code to calculate the WCC sheets using the parallel-transport approach explained in Sec. 3.1.1.

### 4.3 Results

In this section, we present the WCC sheets for the different topological phases we have studied. For the 3D Chern insulator in Sec. 4.4, the WCC sheets are plotted over the entire 2D BZ, while for the TR-invariant systems of Secs. 4.5-4.7 the sheets are plotted over one quarter of the BZ, i.e., between the TRI momenta  $[0, 0]$ ,  $[0, \pi]$ ,  $[\pi, \pi]$ , and  $[\pi, 0]$ .

The axis of highest rotational symmetry in each TB model or material system is chosen as the  $z$  axis. This axis in the FKM model is along the bond with altered strength ( $t_{111}$ ); the model has a 3-fold symmetry around this axis, which when combined with TR-symmetry results in a 6-fold rotational symmetry in the 2D BZ. In  $\text{Sb}_2\text{Se}_3$  and  $\text{Bi}_2\text{Se}_3$  the  $z$  axis is normal to the quintuple layers, which is the axis of 3-fold symmetry. In  $\text{KHgSb}$  the  $z$ -axis is chosen normal to the honeycomb HgSb layers, and in the Fu tetragonal TB model it is along the tetragonal axis.

The WCC sheets are computed along both  $z$  and  $y$  and plotted versus  $(k_x, k_y)$  and  $(k_x, k_z)$  respectively. (Henceforth we shall not be careful about the distinction between  $k_x$  and  $\tilde{k}_x = k_x a$ , etc.; the meaning should be clear from the context.) Plotting the WCC sheets

along these two perpendicular directions is especially important to reveal the topological behavior in the 3D Chern, weak  $Z_2$ , and topological crystalline phases, where, as we shall see, the topology of the WCC sheets may look trivial in one direction but topological in another.

The WCC sheets for the TR-broken Chern insulator phase are discussed next. WCC sheets for the TR-invariant trivial, weak, and strong  $Z_2$  phases are discussed in Secs. 4.5-4.7, using the FKM model and its material system analogues in each phase. The WCC sheets for the crystalline topological phase are discussed in Sec. 4.8.

In this Chapter, study the WCC sheets in trivial, Chern, weak topological, strong topological, and crystalline topological insulators (TIs) using tight-binding models and first-principles calculations. For the 3D Chern insulator in Sec. 4.4, the WCC sheets are plotted over the entire 2D BZ, while for the TR-invariant systems of Secs. 4.5-4.7 the sheets are plotted over one quarter of the BZ, i.e., between the TRI momenta  $[0, 0]$ ,  $[0, \pi]$ ,  $[\pi, \pi]$ , and  $[\pi, 0]$ .

The axis of highest rotational symmetry in each TB model or material system is chosen as the  $z$  axis. This axis in the FKM model is along the bond with altered strength ( $t_{111}$ ); the model has a 3-fold symmetry around this axis, which when combined with TR-symmetry results in a 6-fold rotational symmetry in the 2D BZ. In  $\text{Sb}_2\text{Se}_3$  and  $\text{Bi}_2\text{Se}_3$  the  $z$  axis is normal to the quintuple layers, which is the axis of 3-fold symmetry. In  $\text{KHgSb}$  the  $z$ -axis is chosen normal to the honeycomb  $\text{HgSb}$  layers, and in the  $\text{Fu}$  tetragonal TB model it is along the tetragonal axis.

The WCC sheets are computed along both  $z$  and  $y$  and plotted versus  $(k_x, k_y)$  and  $(k_x, k_z)$  respectively. (Henceforth we shall not be careful about the distinction between  $k_x$  and  $\tilde{k}_x = k_x a$ , etc.; the meaning should be clear from the context.) Plotting the WCC sheets along these two perpendicular directions is especially important to reveal the topological behavior in the 3D Chern, weak  $Z_2$ , and topological crystalline phases, where, as we shall see, the topology of the WCC sheets may look trivial in one direction but topological in

another.

The WCC sheets for the TR-broken Chern insulator phase are discussed next. WCC sheets for the TR-invariant trivial, weak, and strong  $Z_2$  phases are discussed in Secs. 4.5-4.7, using the FKM model and its material system analogues in each phase. The WCC sheets for the crystalline topological phase are discussed in Sec. 4.8.

#### 4.4 TR-broken Chern insulator

We first consider the TB model for a TR-broken Chern insulator phase that was introduced in Sec. 4.1. It is composed of 2D Chern layers stacked along the  $z$  direction with weak interlayer coupling, so we do not expect an (001) slab of the 3D model to show any topological surface states. This is confirmed in the surface projected bandstructure plotted in Fig. 4.1(a), where the shaded region indicates the region of bulk energy bands. No surface states are visible in this case, consistent with the trivial topology for this orientation. By the same token, the WCC sheets computed along the  $z$  direction from the single occupied band remain localized in the vicinity of the  $z$  positions of the layers, with no topological evolution along  $k_x$  or  $k_y$ . This is shown in Fig. 4.1(b-c), where the WCC sheets are plotted around the boundary, and throughout the interior, of the 2D projected BZ respectively.

In contrast, any slab of the 3D system that cuts through the 2D Chern layers will reveal the topological nature of the 3D crystal by displaying a surface energy band traversing the bulk gap on each surface, as shown in Fig. 4.1(d) for a (010) slab. The corresponding  $\bar{y}(k_x, k_z)$  WCC sheets are shown in Figs. 4.1(e-f). While these WCCs do not vary strongly along  $k_z$ , they wind by one unit as they evolve along  $k_x$ , pumping one electron per unit cell from the  $(0\bar{1}0)$  to the  $(010)$  surface. The pumped charge is restored on each surface as the surface bands cross the Fermi level in the bulk energy gap.

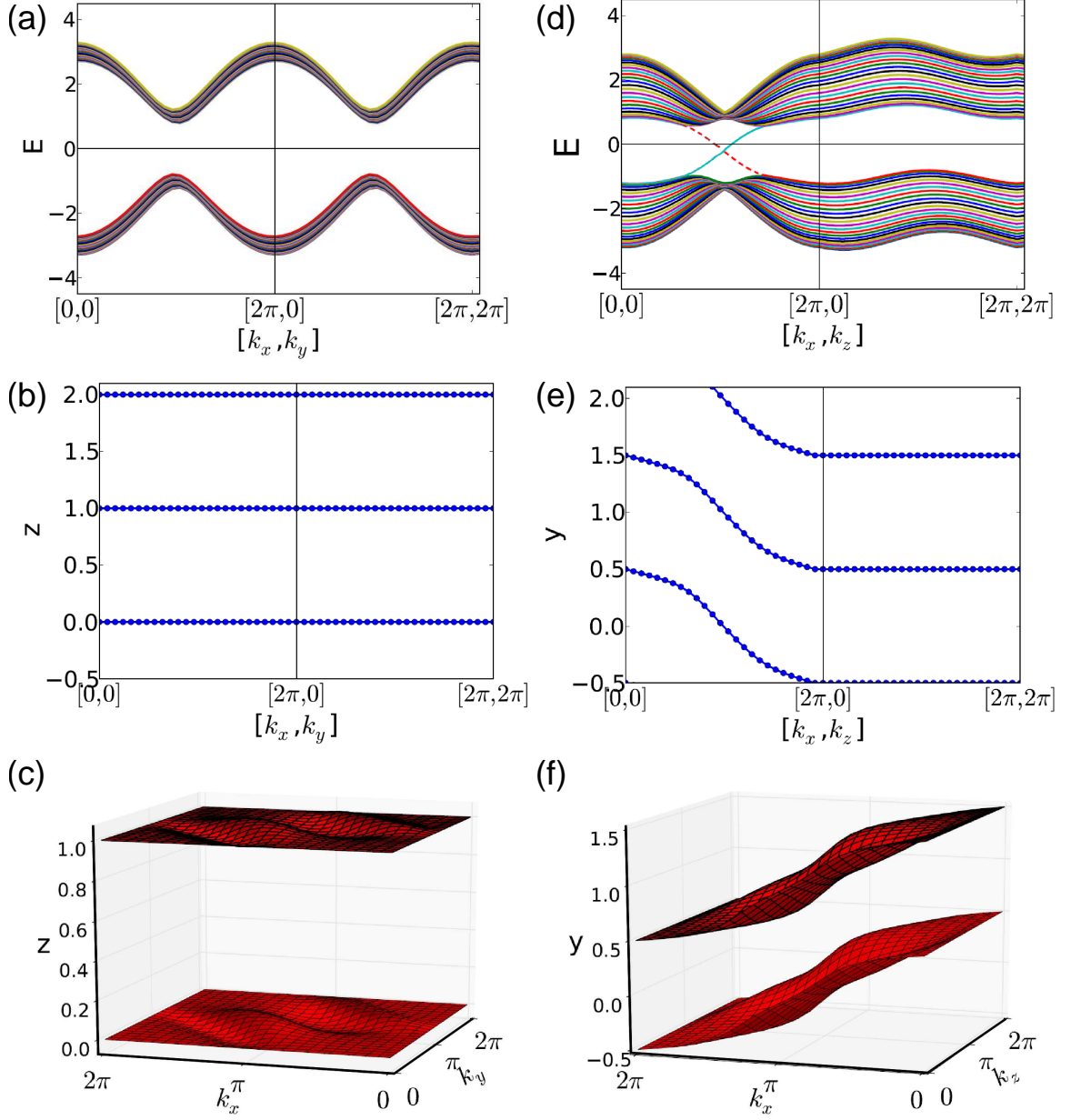


Figure 4.1: Surface energy bands and WCC sheets for the TR-broken Chern insulator model. (a-c) Surface normal and WCCs along  $\hat{z}$  vs.  $(k_x, k_y)$ . (d-f) Surface normal and WCCs along  $\hat{y}$  vs.  $(k_x, k_z)$ . Surface states for a 24-layer slab in (a) and (d); WCCs around 2D BZ boundary in (b) and (e); WCCs in 2D BZ in (c) and (f). Dashed and solid surface states in (d) reside on the top and bottom of the (010) slab respectively. The WCC sheets and surface bands wind by one unit in the  $k_y$ - $k_z$  plane, but not in the  $k_x$ - $k_y$  plane.

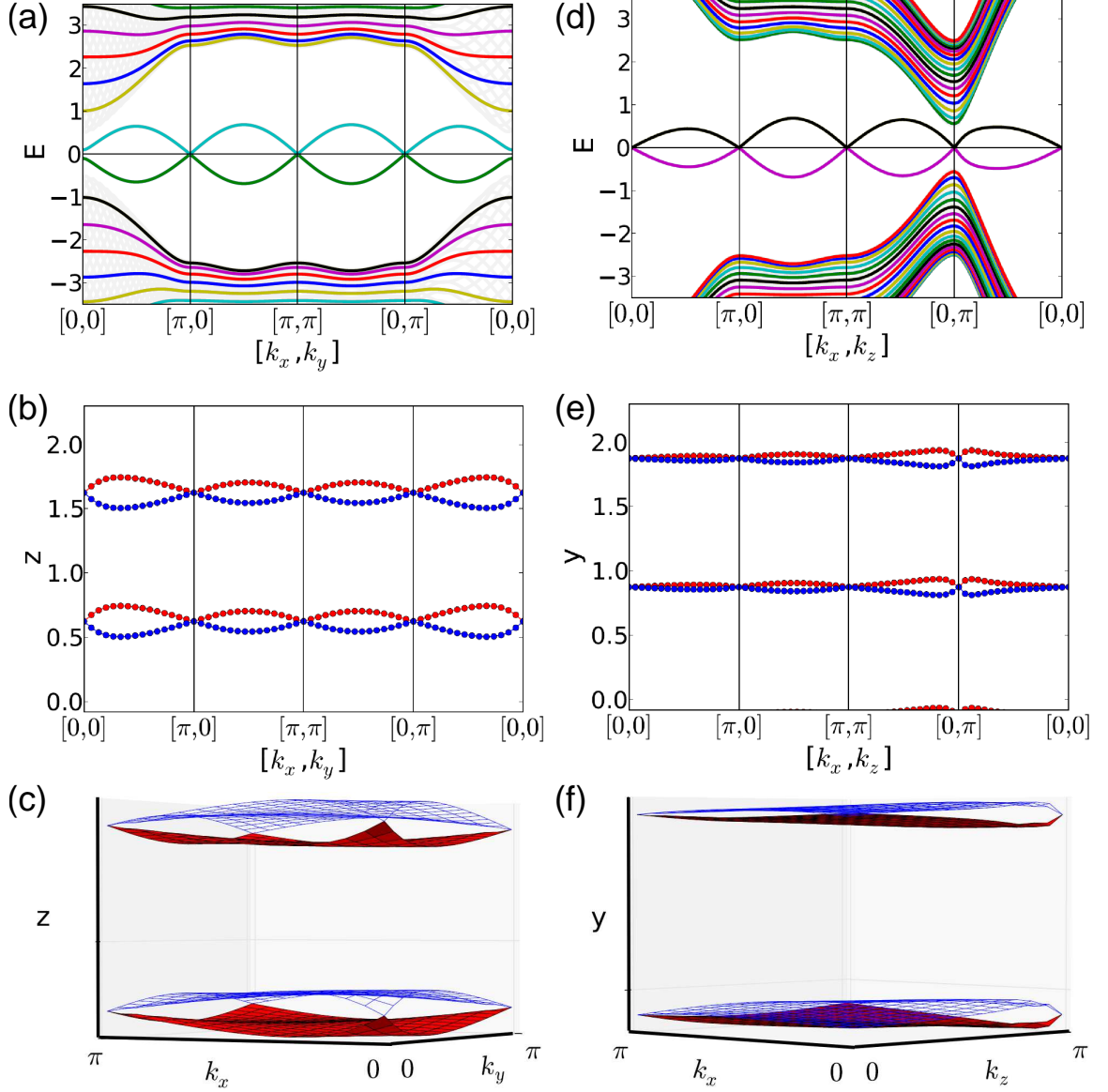


Figure 4.2: Surface energy bands (15-layer slab) and WCC sheets for the TR-invariant FKM model in the trivial phase ( $\alpha = 2.5$ ). (a-c) Surface normal and WCCs along  $\hat{z}$  vs.  $(k_x, k_y)$ . (d-f) Surface normal and WCCs along  $\hat{y}$  vs.  $(k_x, k_z)$ . The WCC sheets and surface bands show a trivial behavior in all directions.

## 4.5 TR-invariant trivial insulator

In general, the broken translational symmetry at the surface of a band insulator allows for the existence of surface states in the bulk band gap. In a topologically trivial insulator, these surface states, if present, are prone to localization by disorder and can be removed from the gap by an adiabatic transformation of the Hamiltonian. An example of such unprotected surface states can be seen in Fig. 4.2(a), which shows the surface states on the (001) surface of the FKM model in its trivial insulating phase. The surface bands are doubly degenerate at the TRI momenta as required by Kramer’s theorem, but nothing protects them from being adiabatically pushed to the valence or conduction band. (The model also happens to have a particle-hole symmetry which is responsible for the mirror symmetry along the energy axis, but we do not consider this as an imposed symmetry here.) The surface energy bands on the (010) surface, Fig. 4.2(d), show the same trivial behavior, indicating that this is a topologically trivial insulator.

The trivial topology of this material is equally evident from the WCC sheets, plotted along  $\hat{z}$  and  $\hat{y}$  in Figs. 4.2(b-c) and (e-f) respectively. The WCC sheets are plotted around the boundary of a quadrant of the 2D projected BZ in Figs. 4.2(b) and (e), and throughout its interior in Figs. 4.2(c) and (f). Here there are two WCC sheets per unit cell (vertical axis) because there are two occupied energy bands in the four-band model, but the band pairs remain well separated from their periodic images above and below. The WCC sheets touch at the TRI points at the corners of the quarter BZ, as required by Kramers’ theorem, but these Kramers pairs are connected in all directions in a topologically trivial way. As a result, the topological index is  $\nu_\mu = +1$  on all six TRI faces, signalling a fully trivial topological phase.

A similar trivial behavior is seen in the first-principles WCCs computed for  $\text{Sb}_2\text{Se}_3$  as shown in Fig. 4.3. The 18 WCC sheets in the quintuple layer come mainly from the Sb  $5p$  and Se  $4p$  orbitals. While having substantial Sb  $5p$  character, they are nevertheless centered

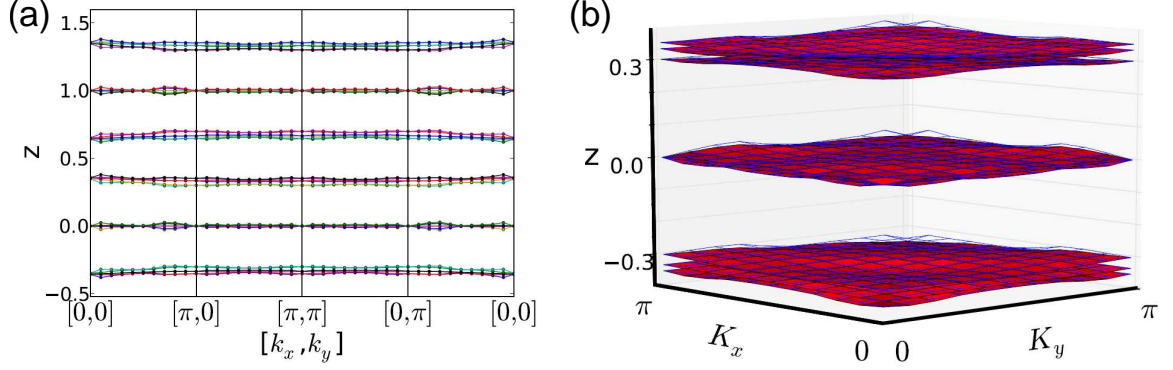


Figure 4.3: First-principles WCC sheets along  $\hat{z}$  for topologically trivial  $\text{Sb}_2\text{Se}_3$ , plotted on (a) the boundary and (b) the interior of the 2D quarter BZ. The WCCs show trivial behavior as expected.

on the anion Se sites located at  $z \simeq -0.3c, 0$ , and  $0.3c$  in the figure. While the gap between WCC sheets associated with neighboring quintuple layers, centered at  $0.5c$  in Fig. 4.3(a), is not obviously larger than the other gaps, it nevertheless remains open across the entire 2D BZ. The WCC sheets plotted along the  $x$  and  $y$  directions (not shown) display a similar trivial behavior. Thus, we can conclude that this is a fully trivial insulator, without having to carry out any surface-state calculation.

#### 4.6 TR-invariant weak topological insulator

The FKM model with  $-2 \leq \alpha \leq 0$  is a weak  $Z_2$ -odd insulator, as illustrated by our results for  $\alpha = -1$  in Fig. 4.4. In this case, the crystal can be thought of as a series of 2D spin-Hall insulators stacked along the  $z$  direction, i.e., the direction of the weakest bond. Thus, a slab of the model cut normal to this direction shows no robust surface states in the bulk energy gap, as shown in Fig. 4.4(a), and the WCC sheets along this direction pair up as they do in a trivial insulator, as can be seen in Figs. 4.4(b-c).

On the other hand, a slab of a weak  $Z_2$ -odd insulator cut through the 2D spin-Hall sheets should host an even number of Dirac cones on each surface. These surface states are shown for an (010) slab of the same FKM model in Fig. 4.4(d), where the Dirac cones are visible at  $(k_x, k_z) = (0, 0)$  and  $(0, \pi)$ . These surface bands have a gap-crossing  $Z_2$ -odd

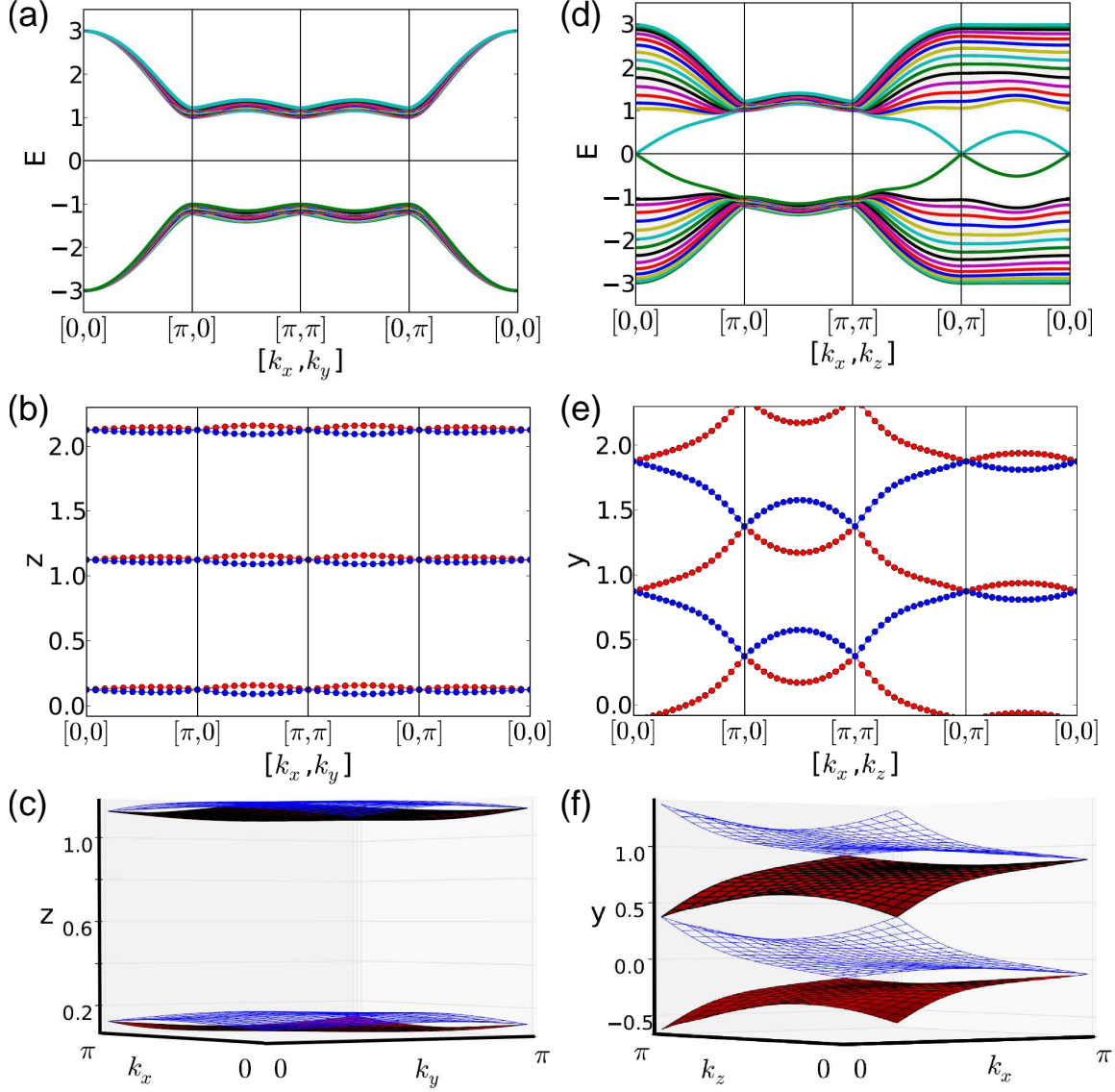


Figure 4.4: Surface energy bands (15-layer slab) and WCC sheets for the TR-invariant FKM model in the weak topological phase ( $\alpha = -1$ ). (a-c) Surface normal and WCCs along  $\hat{z}$  vs.  $(k_x, k_y)$ . (d-f) Surface normal and WCCs along  $\hat{y}$  vs.  $(k_x, k_z)$ . Only the  $(k_x, k_y)$  TRI faces at  $k_z = 0$  and  $k_z = \pi$  are  $Z_2$ -odd.



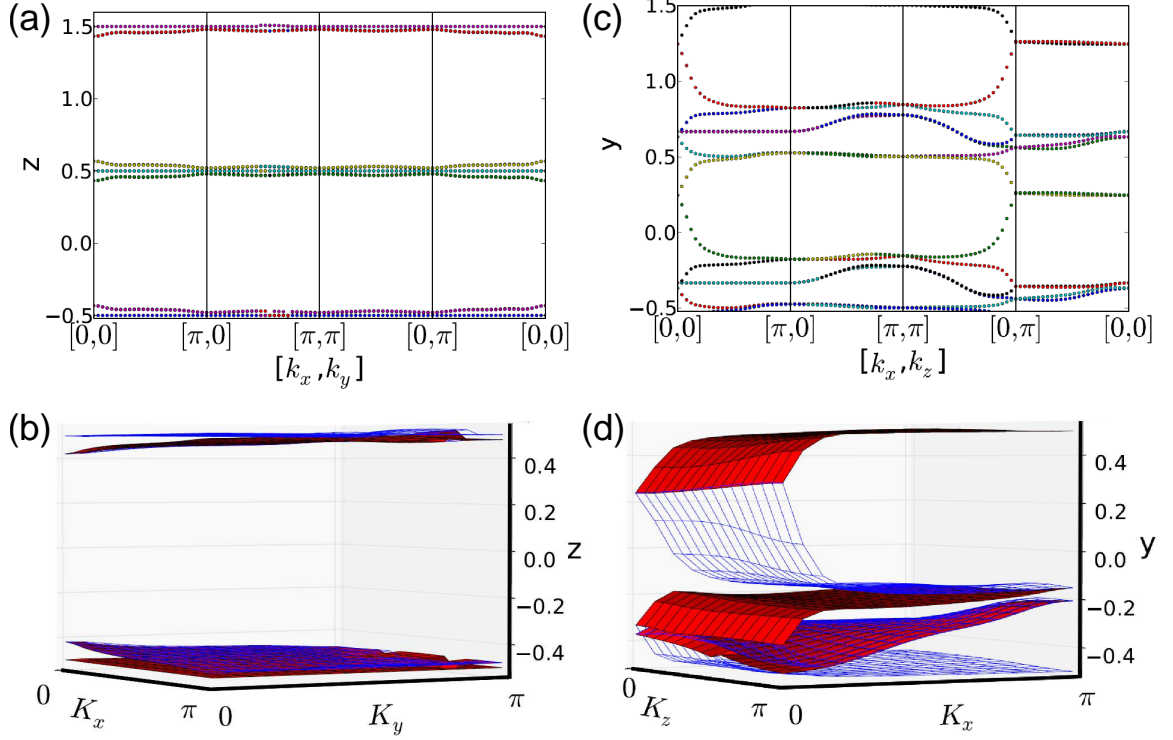


Figure 4.5: First-principles WCC sheets for the weak TI KHgSb. (a-b) Along  $\hat{z}$ . (c-d) Along  $\hat{y}$ . Only the  $(k_x, k_y)$  TRI faces at  $k_z=0$  and  $k_z=\pi$  are  $Z_2$ -odd.

behavior vs.  $k_x$  but not vs.  $k_z$ , suggesting that the  $(k_x, k_y)$  TRI faces of the 3D BZ are  $Z_2$ -odd at  $k_z=0$  and  $\pi$ , while those on the  $(k_y, k_z)$  faces are  $Z_2$ -even at  $k_x=0$  and  $\pi$ . This is confirmed in Figs. 4.4(e-f), where the WCC sheets are seen to swap partners vs.  $k_x$  but not vs.  $k_z$ .

The  $Z_2$  topological invariants  $\nu_\mu$  follow straightforwardly from the above considerations. The invariants are  $+1$  for the TRI faces at  $k_x=0$  and  $\pi$ ,  $+1$  for the TRI faces at  $k_y=0$  and  $\pi$ , and  $-1$  for the TRI faces at  $k_z=0$  and  $\pi$ . The conventional index set is then  $[\nu_0; \nu_1 \nu_2 \nu_3] = [+; + + -]$ , confirming that this is a weak TI ( $\nu_0 = +1$ ) corresponding to spin-Hall layers stacked along  $z$  ( $\nu_3 = -1$ ).

We see the same kind of weak topological behavior in our first-principles calculations of the WCC sheets for KHgSb shown in Fig. 4.5. As explained in Sec. 4.2, this material is composed of honeycomb HgSb layers that behave as 2D spin-Hall insulators, stacked along the  $z$  direction, and separated by hexagonal layers of K stuffing atoms. The pictures look

more complicated because there are now six occupied bands per cell, and thus six WCCs per lattice constant, and some of the artificial symmetries of the FKM model are now absent. However, the topological behavior is similar to that of Fig. 4.4. The weak coupling between the HgSb layers is reflected in the trivial behavior of the WCC sheets along the (001) direction, Figs. 4.5(a-b), but plotting the WCCs in a direction cutting across the honeycomb HgSb layers reveals the topological behavior, as seen in Figs. 4.5(c-d). These WCC sheets change partners on the  $(k_x, k_y)$  TRI faces at both  $k_z = 0$  and  $\pi$ , indicating  $\nu_3 = -1$  and  $\nu_0 = +1$ , giving the same  $[+, +, +, -]$  set of indices as for the FKM model in its weak topological phase. These results are entirely consistent with the existence of Dirac cones at the  $\bar{\Gamma}$  and  $\bar{Z}$  points in the surface bands of an (010) slab as shown in Ref. yan-prl12. However, we again emphasize the convenience of our approach, in which only primitive-cell bulk calculations are needed.

#### 4.7 TR-invariant strong topological insulator

In contrast to weak TIs, the non-trivial behavior of the WCC sheets in strong  $Z_2$  insulators should be evident no matter what direction is chosen to construct them; there would be switching of partners for one of the TRI faces in any chosen direction. This behavior is illustrated in Fig. 4.6, where the surface bands and WCC sheets are presented for the FKM model in the strong  $Z_2$ -odd phase at  $\alpha = 1$ . Both the surface bands and the WCC sheets swap partners in the  $(k_x, k_y)$  plane at  $k_z = \pi$ , the  $(k_x, k_z)$  plane at  $k_y = 0$ , and the  $(k_y, k_z)$  plane at  $k_x = 0$ , but not on the other three TRI faces. The set of topological indices is therefore  $[\nu_0; \nu_1 \nu_2 \nu_3] = [-; + + -]$ , and the system is a strong TI. This is also consistent with the existence of an odd number of Dirac cones on any surface of a strong  $Z_2$  insulator, as is evident in Figs. 4.6(a) and (d), where three Dirac cones are visible in each case.

We again confirm that our approach works in the first-principles context by presenting the WCC sheets along the  $z$  direction (rhombohedral-axis) in the strong TI  $\text{Bi}_2\text{Se}_3$ , as shown in Fig. 4.7. There are now 18 WCC sheets per cell; in most of the 2D projected BZ these

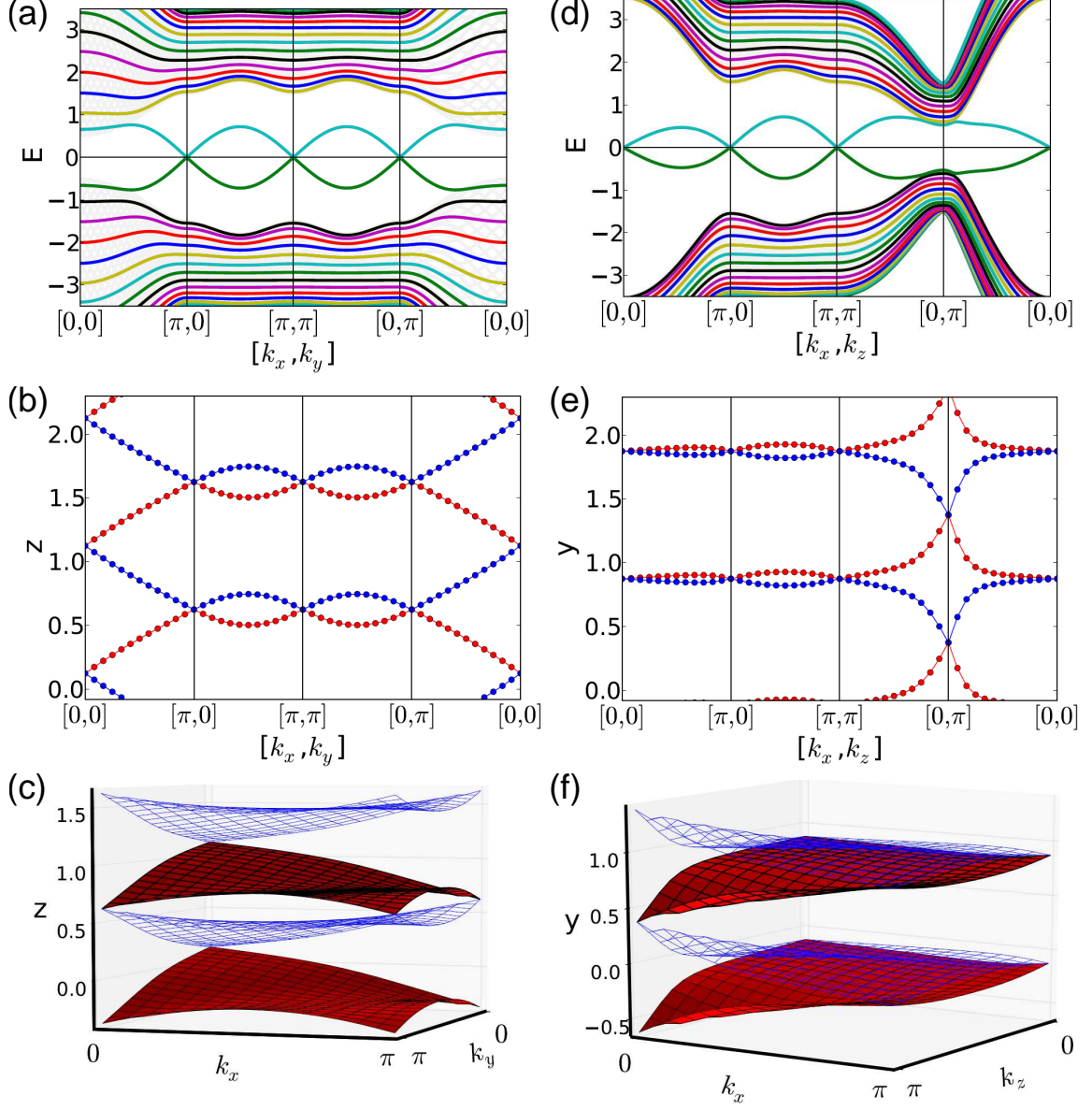


Figure 4.6: Surface energy bands (15-layer slab) and WCC sheets for the TR-invariant FKM model in the strong topological phase ( $\alpha=1$ ). (a-c) Surface normal and WCCs along  $\hat{z}$  vs.  $(k_x, k_y)$ . (d-f) Surface normal and WCCs along  $\hat{y}$  vs.  $(k_x, k_z)$ . The  $(k_x, k_y)$  TRI face at  $k_z=\pi$ , the  $(k_x, k_z)$  TRI face at  $k_y=0$ , and the  $(k_y, k_z)$  TRI face at  $k_x=0$  are  $Z_2$ -odd.

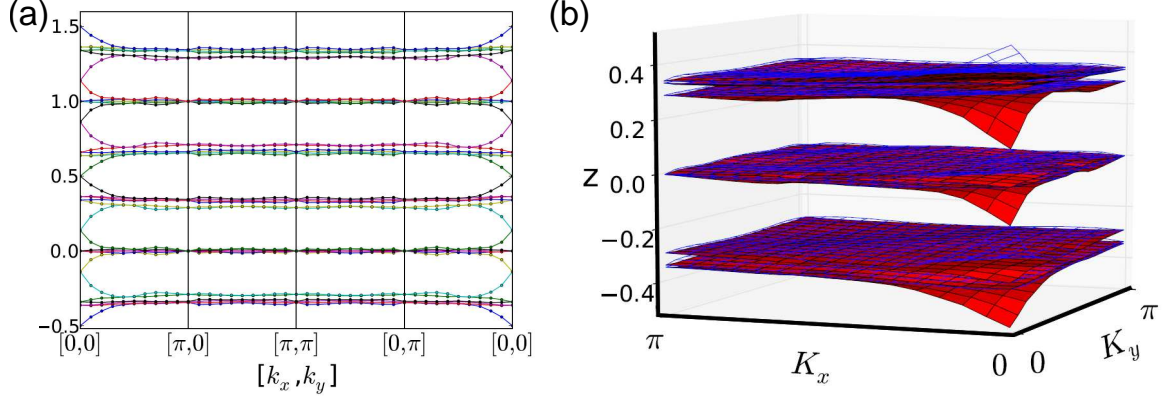


Figure 4.7: First-principles WCC sheets for the strong TI  $\text{Bi}_2\text{Se}_3$ , plotted on (a) the boundary and (b) the interior of the 2D quarter BZ. The WCC sheets on parallel TRI faces (e.g., at  $k_x=0$  and  $k_x=\pi$ ) show opposite topological behavior.

are clustered in groups of six, with each of the three clusters located close to the  $z$  position of a layer of Se atoms within the QL. This is reasonable, as the Bi and Se atoms can be regarded as cations and anions respectively, and it is natural to find the Wannier centers on the anions. However, this behavior changes drastically near  $\bar{\Gamma}$ , where two of the six WCC sheets in each cluster split off and form a Dirac point at  $\bar{\Gamma}$ , signaling the strong TI nature of this material. Clearly this results from the band inversion near  $\Gamma$  in the 3D bulk BZ, and is consistent with the existence of a single Dirac cone at  $\bar{\Gamma}$  on the surface of  $\text{Bi}_2\text{Se}_3$ , as has been amply demonstrated by angle-resolved photoemission and other experimental probes [21]. We can again read off the topological indices by noting that the WCC sheets swap partners in the  $(k_x, k_y)$  plane at  $k_z=0$ , the  $(k_x, k_z)$  plane at  $k_y=0$ , and the  $(k_y, k_z)$  plane at  $k_x=0$ , but not on the other three TRI faces, so that  $[\nu_0; \nu_1 \nu_2 \nu_3] = [-; ++]$ .

#### 4.8 Crystalline topological insulator

In contrast to the systems studied above, Fu's tetragonal model for a crystalline TI [13] is spinless, because the non-trivial topology of a topological crystalline insulator has its roots in the crystal symmetries rather than in TR symmetry and spin-orbit interaction. The TR symmetry in this scalar model does not guarantee double degeneracy at the TRI momenta, but its combination with the crystal  $C_4$  symmetry leads to a two-fold degeneracy of the

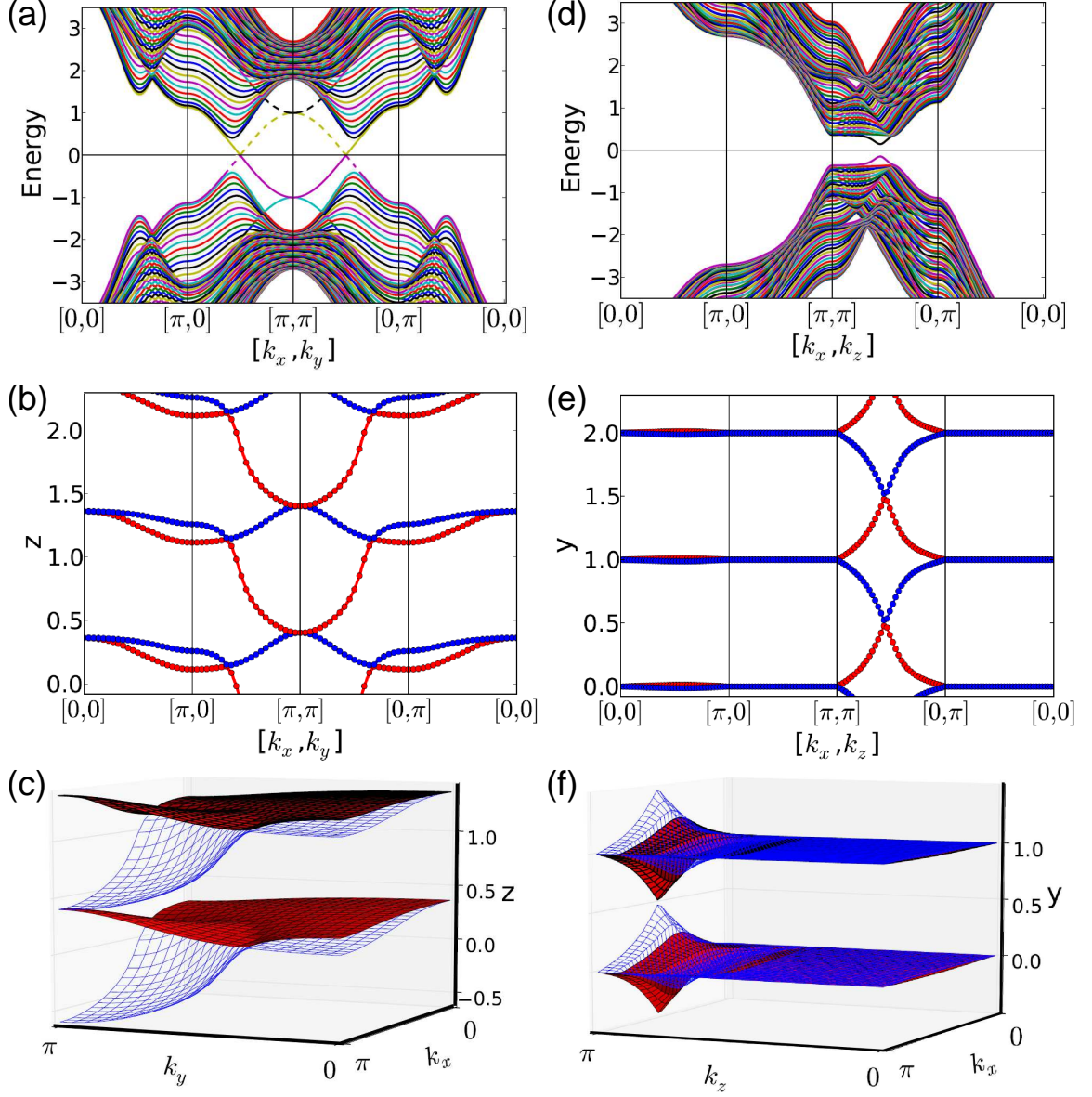


Figure 4.8: Surface energy bands (24-layer slab) and WCC sheets for tight-binding model of a crystalline TI. (a-c) Surface normal and WCCs along  $\hat{z}$  vs.  $(k_x, k_y)$ . (d-f) Surface normal and WCCs along  $\hat{y}$  vs.  $(k_x, k_z)$ . Dashed and solid surface states in (a) reside on the top and bottom of the (001) slab respectively. Quadratic band touching and cross-linking in panels (a-c) signals the crystalline topological phase.

surface energy bands at  $\bar{\Gamma} = (0, 0)$  and at  $\bar{M} = (\pi/a, \pi/a)$  for the (001) surface, where  $z$  is chosen along the tetragonal axis. These surface bands can be seen in Fig. 4.8(a) for an (001) slab of the model. The dashed and solid lines show the surface states on the two surfaces of the slab. These bands traverse the energy gap in a zig-zag manner, and their protected degeneracy at the  $\bar{M}$  point guarantees a robust metallic (001) surface. This non-trivial behavior is clearer when considering the behavior of the WCC sheets along the  $z$  direction, plotted in Figs. 4.8(b-c). Over most of the 2D BZ, the  $z$  location of these sheets is midway between the A and B atoms. The sheets touch two-by-two at  $\bar{\Gamma}$ , but they open up and switch partners on approaching the  $\bar{M}$  point. Thus, the WCC undergo the same kind of switching, and so reflect the same topological properties, as in the surface energy bands. Even the quadratic dispersion of the surface bands around  $\bar{M}$  is reflected in the WCCs.

The  $C_4$  symmetry is broken on any surface other than the (001) surface, which means no robust surface states are expected on these other surfaces. Fig. 4.8(d) confirms this for the case of an (010) slab of the model. The energy bands approach each other near a point midway between  $(k_x, k_z) = (\pi, \pi)$  and  $(0, \pi)$ , but they do not touch. The WCC sheets show a similar behavior in Figs. 4.8(e-f), remaining trivial except along the segment at  $k_z = \pi$ ; while there is a non-avoided crossing along this line, this appears to be an artifact of some special symmetries of the model, and is not relevant to the discussion at hand.<sup>1</sup> Thus, both the surface bands and WCC sheets are consistent with the trivial topology of an (010) slab of the model.

## 4.9 Weyl Semimetal

In Weyl semimetals the conduction and valence bands touch at points in the 3D BZ where the dispersion relation is linear. The Nielsen-Ninomiya theorem indicates that Weyl points must come in pair(s) [46]. In presence of inversion symmetry, the Weyl points happen

---

<sup>1</sup>The topological index for the path from  $(\pi, \pi)$  to  $(0, 0)$  (third and fourth panels) in Figs. 4.8(e) is even, because a horizontal segment drawn at any chosen  $y$  crosses the sheets an even number of times along this path; this is true regardless of whether the crossing is avoided or not.

at opposite positions in the BZ and have opposite helicities. If time-reversal symmetry is present, on the other hand, the Weyl points of opposite momenta must have the same helicity. Thus, in a Weyl semimetal with both time-reversal and inversion symmetries at least two Weyl pairs must be present.

In the DLC TB model the time-reversal symmetry is broken by magnetic flux, but the flux pattern respects the inversion symmetry of the lattice. Therefore, there are only two Weyl points at  $(k_x, k_y, k_z) = (0, 0, \pm \frac{\pi}{2})$ , and they have opposite helicities. These touching points coincide when projected on the (001) surface. Consequently, the energy bands on this surface are fully gapped. In contrast, on the (010) surface the two Weyl points are projected to  $(k_x, k_z) = (0, \pi/2)$  and  $(k_x, k_z) = (0, 3\pi/2)$  in the 2D BZ where the valence and conduction bands touch. As a result a Fermi arc appears on this surface connecting the two projected Weyl points. In general, a Fermi arc exists on any surface which is not perpendicular to the  $z$  axis.

The WCCs are not well defined at the degeneracy points, however they can be calculated for the valence band at any other point in the 2D projected BZ. The WCC sheets along two directions, parallel and perpendicular to  $\hat{z}$ , are plotted in Fig. 4.9. The WCC sheets along  $\hat{z}$  direction are almost flat and well separated from each other, in agreement with the gapped energy bands on the (001) surface. The WCC sheets calculated along  $\hat{y}$ , however, have the topology of a Riemann surface with two nodes at  $(k_x, k_z) = (0, \pi/2)$  and  $(k_x, k_z) = (0, 3\pi/2)$ . These two nodes show clockwise and anticlockwise chiralities which is a consequence of the Weyl points' opposite helicities. While in insulating topological phases the WCC sheets are double degenerate at high symmetry points where the protected surface energy band touchings happen; in topological semimetals the protected metallic nature of the nodes is reflected in the absence of localized WCCs at these points.



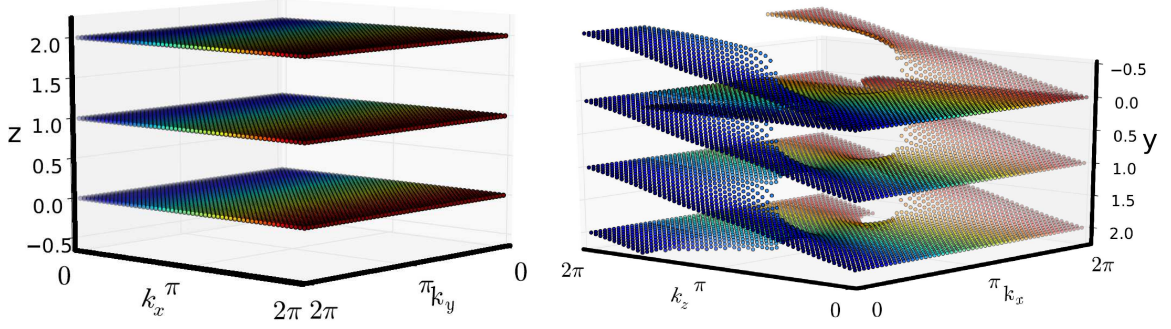


Figure 4.9: WCCs along  $\hat{z}$  vs.  $(k_x, k_y)$  and WCCs along  $\hat{y}$  vs.  $(k_x, k_z)$  for Weyl semimetal.

#### 4.10 Summary

In this manuscript, we have explained how the hybrid Wannier charge centers, or WCC sheets, can be calculated using a parallel-transport approach along a chosen direction in a 3D insulator and plotted versus the other  $k$ -space dimensions. We have shown that these sheets contain the same topological information as the surface energy bands, and thus provide an accessible means of deducing the topological invariants of the insulator from the bulk properties alone. We also show that the linear dispersion of the surface energy bands at Dirac points in  $Z_2$  TIs, and their quadratic behavior at the gap closure in topological crystalline insulators, are replicated by the WCCs. Moreover, the symmetry group of the WCCs in the 2D BZ include all the symmetry operators of the surface bands.

We have demonstrated the distinct behavior of the WCC sheets in trivial, Chern, weak, strong, and crystalline TIs as well as Weyl semimetal using various tight-binding models. In addition, we have used first-principles calculations to illustrate the calculation of the WCC sheets in  $Z_2$ -even  $\text{Sb}_2\text{Se}_3$ , weak  $Z_2$ -odd  $\text{KHgSb}$ , and strong  $Z_2$ -odd  $\text{Bi}_2\text{Se}_3$ , confirming the conclusions from the tight-binding models.

Admittedly, the topological invariants of Chern, TR-invariant, and crystalline TIs can be deduced in other ways. For example, for the TR-invariant case, parity eigenvalues can be used if inversion symmetry is present; if not, a calculation of 1D Wannier centers on each 2D TRI face is sufficient [23, 24]. However, the WCC sheets provide a unifying description



that works in all these cases, allows for a more intuitive comparison of different kinds of TIs, and provides deeper insight into the origins of the non-trivial topology.

The evolution of the WCC sheets as the Hamiltonian is varied through a trivial-to-topological phase transition, or carried adiabatically around a loop that pumps the Chern-Simons axion coupling by a quantum,[47, 48] is studied in Chapter 5.

## Chapter 5

### Adiabatic Pumping of Chern-Simons Axion Coupling

The discovery of topological insulators (TIs) and related classes of materials in recent years has generated interest in the Chern-Simons axion (CSA) coupling, which makes an isotropic contribution  $\alpha^{CS}$  to the magnetoelectric response tensor of the material. This coupling, defined as

$$\alpha_{ij} = (\partial P_i / \partial B_j)_E = (\partial M_j / \partial E_i)_B, \quad (5.1)$$

where  $P$  ( $M$ ) is the polarization (magnetization) and  $E$  ( $B$ ) is the electric (magnetic) field, is conventionally expressed in terms of a dimensionless parameter  $\theta$  defined via

$$\alpha_{ij}^{CS} = \frac{\theta e^2}{2\pi h} \delta_{ij}, \quad (5.2)$$

where  $\theta$  is determined by the band structure of the insulator via an integral over the Brillouin zone (BZ) of a Chern-Simons 3-form according to

$$\theta = -\frac{1}{4\pi} \int d^3k \epsilon^{ijk} \text{Tr}[A_i \partial_j A_k - i \frac{2}{3} A_i A_j A_k]. \quad (5.3)$$

Here  $A_i^{nm} = i\langle u_n | \partial_i | u_m \rangle$  is the Berry connection (or non-Abelian gauge field) in Cartesian direction  $i$ , where  $u_n(\mathbf{k})$  is the periodic part of the Bloch function of the  $n$ 'th occupied band, and the trace is over occupied bands.

In general, the linear magnetoelectric coupling tensor of a crystal  $\alpha_{ij}$  can have nonzero off-diagonal components as well as diagonal ones, depending on its magnetic point group. This polarizability can be decomposed into an ionic and an electronic part, where each part

has contributions from spin or orbital degrees of freedom. The ionic contribution describes the lattice-mediated response of crystal to external electromagnetic fields, while the orbital magnetoelectric polarizability measures the orbital response of material to external electromagnetic fields in frozen ion limit, and can be decomposed into an isotropic and a traceless part

$$\alpha_{ij}^{orb} = \tilde{\alpha}_{ij} + \alpha^{iso} \delta_{ij}. \quad (5.4)$$

The electromagnetic tensor  $\alpha$  is odd under time-reversal and inversion symmetry as can be seen from its definition in Eq. 5.1. As a result, in materials with either or both of these symmetries  $\tilde{\alpha}$  vanishes. The isotropic part of the coupling on the other hand, has a part generated by axionic fields in the material that can survive even in presence of these symmetries.

The ground-state properties of a band insulator are invariant under any gauge transformation, that is, any unitary transformation  $U_{nn'}(\mathbf{k})$  that mixes only the occupied bands. It can be shown that an arbitrary gauge transformation either leaves the 3-form integral in Eq. (5.3) unchanged or else shifts it by exactly  $2\pi$  times an integer. Thus,  $\theta$  is best regarded as a phase angle that is only well-defined modulo  $2\pi$ . As a consequence, the presence of either time reversal (TR) or inversion (either of which flips the sign of  $\theta$ ) requires  $\theta$  to be quantized to an integer multiple of  $\pi$ , with an odd/even value corresponding to an odd/even strong  $Z_2$  topological index of a TR-invariant 3D insulator.[47, 48] One way to understand the ambiguity of  $\theta$  modulo  $2\pi$ , which corresponds to an ambiguity of  $\alpha^{CS}$  modulo  $e^2/h$ , is to realize that the magnetoelectric coupling is related to the surface anomalous Hall conductivity (AHC) by  $\sigma = (\theta/2\pi + C)e^2/h$ . Thus the measurable magnetoelectric response can be changed by a quantum if a layer with non-zero Chern number is attached to the surface, changing the effective value of  $\theta$  by  $2\pi$ .

An interesting consequence of this  $2\pi$  ambiguity is that if an insulator is allowed to evolve adiabatically around a closed loop in the space of parameters determining the crystal

Hamiltonian, with the gap remaining open, then the fact that the system returns to the initial physical state means that  $\theta$  must either return to its original value or change by  $2\pi C^{(2)}$ , where  $C^{(2)}$  is an integer known as a “second Chern number.” This possibility of “pumping  $\theta$  by  $2\pi$ ” has been discussed and demonstrated for some theoretical models,[47, 48] but the characteristic behaviors of a system undergoing such an adiabatic loop have largely remained unexplored.

In Chapter 3 and 4, we showed that the hybrid Wannier representation can be a useful and insightful tool for computing topological indices and inspecting the topological properties of 3D insulators.[49] In this approach, the occupied-state wavefunctions are transformed into a maximally-localized Wannier representation in one chosen direction, while remaining Bloch-like in the orthogonal directions. The resulting hybrid Wannier functions (HWFs) inherit the topological character of the insulator, and plots of their Wannier charge centers (WCCs) over the 2D BZ (“Wannier sheets”) were shown to provide a useful means of visualizing the topological properties of insulators, allowing to discriminate between normal, strong topological, weak topological, crystalline topological, and related states.[23, 26, 49, 50]

With these motivations, we ask what happens if an adiabatic cycle that pumps  $\theta$  by  $2\pi$  is viewed from the point of view of the HWF representation. How do the WCC sheets evolve? Is there a characteristic behavior that signals the presence of a non-trivial cycle (i.e., a non-zero second Chern number)? Answering in the affirmative, we show that quanta  $e^2/h$  of Berry curvature are passed from one WCC sheet to the next in a series of isolated band-touching events, in such a way that one quantum of Berry curvature is pumped by an entire lattice vector by the close of the cycle. We illustrate this amusing and instructive result via numerical calculations on a 3D spinor tight-binding model and discuss its implications.

## 5.1 CSA Coupling in Wannier Representation

For a 2D insulator the WCCs can be plotted as curves  $\bar{z}_n$  vs.  $k_\perp$  in a 1D projected BZ,[23, 24] while for a 3D insulator they can be visualized as sheets plotted over the 2D projected BZ. In the previous chapter we have shown that these WCC sheets provide an insightful characterization of the topological character of the insulator in question, allowing one to see how electrons are adiabatically pumped along  $\hat{z}$  as  $k_x$  and  $k_y$  are varied. For example, in a 2D Chern insulator the WCCs shift by one or more lattice constants along  $z$  as  $k_x$  evolves across the projected BZ, pumping units of charge along that direction. This extra charge is removed from the edge as the edge band crosses the Fermi energy. Time reversal invariant (TRI) insulators have zero Chern numbers but are characterized by  $Z_2$  topological indices that are also reflected in the structure of WCC sheets. For example, a 3D TRI insulator is characterized by one strong and three weak  $Z_2$  indices, which can be determined by examining how the WCC sheets connect along TRI lines in the projected BZ for different Wannierization directions.[49]

It is also of interest to consider the behavior of the WCC sheets as the crystal Hamiltonian is carried adiabatically around a loop defined by some cyclic parameter  $\alpha$  corresponding, e.g., to some combination of atomic displacements and/or external fields. A celebrated result of Thouless[51] is that this results in quantized adiabatic charge transport, i.e., the pumping of exactly one electron per unit cell by a lattice vector  $\mathbf{R}$  during the cycle. Normally  $\mathbf{R} = \mathbf{0}$ , but for example if  $\mathbf{R} = c\hat{z}$  this corresponds to the pumping of one electron by one period along  $z$  during the cycle (a first Chern number of  $C = 1$ ), i.e., a change in electric polarization  $\Delta P_z = -e/A_{\text{cell}}$  with  $A_{\text{cell}}$  being the projected unit cell area.

Let us see how this evolution occurs from the viewpoint of the HWF representation. Intuitively, we expect each WCC sheet to drift along  $z$  with increasing  $\alpha$  such that it replaces the one above it, and is replaced by the one below it, at the end of the cycle. We

begin by defining Berry potentials “living on the sheets” as

$$A_{x,ln,l'm} = \langle W_{ln} | i\partial_x | W_{l'm} \rangle, \quad (5.5)$$

and

$$A_{y,ln,l'm} = \langle W_{ln} | i\partial_y | W_{l'm} \rangle. \quad (5.6)$$

These are functions of  $(k_x, k_y)$  and also matrices in the space of sheet labels  $ln$  (the  $n^{\text{th}}$  sheet in cell  $l$  along  $z$ ).

In general for any operator  $F$  which does not involve the  $z$  operator or  $k_z$  derivatives, we expect  $F$  to be periodic in the layer representation, i.e.,  $\langle W_{ln} | F | W_{l'm} \rangle$  only depends on  $l$  and  $l'$  through  $l - l'$ . The corresponding Berry potentials in the Bloch representation are then just

$$A_{x,nm}(\mathbf{k}) = \sum_l e^{ik_z lc} A_{x,0n,lm}(k_x, k_y), \quad (5.7)$$

$$A_{y,nm}(\mathbf{k}) = \sum_l e^{ik_z lc} A_{y,0n,lm}(k_x, k_y), \quad (5.8)$$

$$A_{z,nm}(\mathbf{k}) = \bar{z}_n(k_x, k_y) \delta_{nm}. \quad (5.9)$$

Note that  $Z_{ln,l'm} = \langle W_{ln} | z | W_{l'm} \rangle$  is not periodic and we have

$$Z_{ln,l'm} = Z_{0n,(l'-l)m} + lc \delta_{ll'} \delta_{nm}. \quad (5.10)$$

To derive Eq. 5.9 we use the relation  $i\partial_z |u_{nk}\rangle = \sum_l (z - lc) e^{-ik_z(z-lc)} |W_{ln}\rangle$  to write

$$A_{z,nm}(\mathbf{k}) = \frac{1}{N} \sum_{l''} e^{-ik_z(l''-l)c} \langle W_{ln} | (z - l''c) | W_{l''m} \rangle. \quad (5.11)$$

Setting  $l'' = l' - l$  and using Eq. 5.10 we find

$$A_{z,nm}(\mathbf{k}) = \frac{1}{N} \sum_{l''} e^{-ik_z l'' c} \langle W_{0n} | (z - l''c) | W_{l''m} \rangle, \quad (5.12)$$

which is independent of  $l$ . We arrive at Eq. 5.9 by simply renaming  $l'' \rightarrow l$ , and considering the fact that the operator  $z$  is diagonal in HWF representation

$$Z_{ln,l'm} = \delta_{ll'} \delta_{nm} (lc + z_n). \quad (5.13)$$

Plugging Eq.s 5.7-5.9 into the Berry-phase formula for the electronic contribution

$$P_j = -e(2\pi)^{-3} \sum_n \int d^3k A_{jn}(\mathbf{k}), \quad (5.14)$$

we find

$$P_x = \frac{-e}{(2\pi)^2 c} \sum_n \int d^2k A_{x,0n,0n}(k_x, k_y), \quad (5.15)$$

$$P_y = \frac{-e}{(2\pi)^2 c} \sum_n \int d^2k A_{y,0n,0n}(k_x, k_y), \quad (5.16)$$

$$P_z = \frac{-e}{(2\pi)^2 c} \sum_n \int d^2k \bar{z}_n(k_x, k_y). \quad (5.17)$$

For the case of a parametric loop that pumps electrons along  $z$ , the change

$$\Delta P_z = -e/A_{\text{cell}} \quad (5.18)$$

would occur via the gradual migration of the  $\bar{z}(k_x, k_y)$  along the  $+\hat{z}$  direction, with a relabelling of sheets required at the end of the loop.

Now we again consider an adiabatic cycle in a 3D insulator, but this time one that results in the pumping of the CSA coupling, increasing  $\theta$  by  $2\pi$  times the second Chern number  $C^{(2)}$  defined earlier. This corresponds to a pumping of Berry curvature, instead of electric charge, along  $z$  during the adiabatic cycle. For this purpose we define a Berry curvature on the WCC sheets as

$$\Omega_{xy,ln,l'm}(k_x, k_y) = i\langle \partial_x W_{ln} | \partial_y W_{l'm} \rangle - i\langle \partial_y W_{ln} | \partial_x W_{l'm} \rangle. \quad (5.19)$$

The relation to the Berry curvature in the Bloch representation is similar to that for  $A$

$$\Omega_{xy,nm}(\mathbf{k}) = \sum_l e^{ik_z lc} \Omega_{xy,0n,lm}(k_x, k_y). \quad (5.20)$$

The intrinsic AHC  $\sigma_{yx}$  of the crystal is just given by integrating the trace of  $\Omega_{xy}$  in the Bloch representation over the 3D BZ, and this is easily shown to be equal to  $(e^2/hc) \sum_n C_n$  where  $C_n$  is the Chern number of the  $n^{\text{th}}$  sheet in the home unit cell, given by

$$C_n = (2\pi)^{-1} \int d^2k \Omega_{xy,0n,0n}. \quad (5.21)$$

We shall exclude quantum anomalous Hall insulators from our discussion here, so we can assume that  $\sum_n C_n = 0$ , but importantly the individual  $C_n$  can be nonzero.

We now address the central issue of this chapter, namely, how to represent the CSA coupling  $\theta$  in the HWF representation. Starting from Eq. (5.3), and using the cyclic properties of the trace and the fact that  $A_i$  matrices are Hermitian, this can be written as

$$\theta = \theta_{z\Omega} + \theta_{\Delta xy} \quad (5.22)$$

where

$$\theta_{z\Omega} = -\frac{1}{2\pi} \int d^3k \text{Tr}[A_z \Omega_{xy}], \quad (5.23)$$

$$\theta_{\Delta xy} = -\frac{1}{2\pi} \int d^3k \text{Tr}[A_y \partial_z A_x - i A_z [A_x, A_y]]. \quad (5.24)$$

To arrive at this formula we used the periodicity of the gauge to convert  $A_z \partial_y A_z$  into  $-A_z \partial_y A_x$  etc. by integration by part.

Performing the  $k_z$  integrals, these are expressed in the HWF representation as

$$\theta_{z\Omega} = -\frac{1}{c} \int d^2k \sum_n \bar{z}_n \Omega_{xy,0n,0n}, \quad (5.25)$$



$$\theta_{\Delta xy} = \frac{i}{c} \int d^2k \sum_{lmn} (\bar{z}_{lm} - \bar{z}_{0n}) A_{x,0n,lm} A_{y,lm,0n}, \quad (5.26)$$

where  $\bar{z}_{lm} = lc + \bar{z}_m$ . In deriving Eq. (5.26) we have used that

$$\frac{c}{2\pi} \int dk_z \text{Tr}[A_y \partial_z A_x] = \sum_l \sum_{nm} (ilc) A_{x,0n,lm} A_{y,lm,0n}, \quad (5.27)$$

$$\frac{c}{2\pi} \int dk_z \text{Tr}[A_z A_x A_y] = -i \sum_l \sum_{nm} \bar{z}_{0n} A_{x,0n,lm} A_{y,lm,0n}, \quad (5.28)$$

and

$$\frac{c}{2\pi} \int dk_z \text{Tr}[A_z A_y A_x] = -i \sum_l \sum_{nm} \bar{z}_{0n} A_{y,0n,lm} A_{x,lm,0n}. \quad (5.29)$$

Eqs. (5.22) and (5.25-5.26) constitute a major result of the present work.<sup>1</sup>

Of primary concern to us here is the “Berry curvature dipole” term  $\theta_{z\Omega}$  in Eq. (5.25), which describes the extent to which concentrations of positive and negative Berry curvature on the WCC sheets, given by  $\Omega_{xy,0n,0n}(k_x, k_y)$ , are displaced from one another along the  $\hat{z}$  direction as given by  $\bar{z}_n(k_x, k_y)$ . Note that  $\theta_{z\Omega}$  is shifted by  $-2\pi C_n$  if the choice of WCC sheets comprising the home unit cell is changed so as to shift some  $\bar{z}_n$  by  $c$ . The  $\theta_{z\Omega}$  term is therefore the one that has the  $2\pi$  ambiguity, and we shall see that it is responsible for the pumping of CSA coupling. The second term  $\theta_{\Delta xy}$ , given by Eq. (5.26), is an intersheet contribution in which the  $z$ -separation between sheets at  $(k_x, k_y)$  is coupled to the off-diagonal (inter-sheet) matrix elements of the Berry potentials. There is no  $2\pi$  ambiguity associated with this term, and as we shall see, it typically remains small even when  $\theta$  is not. We regard it as a correction term that is needed for quantitative accuracy but is not relevant to topological considerations.

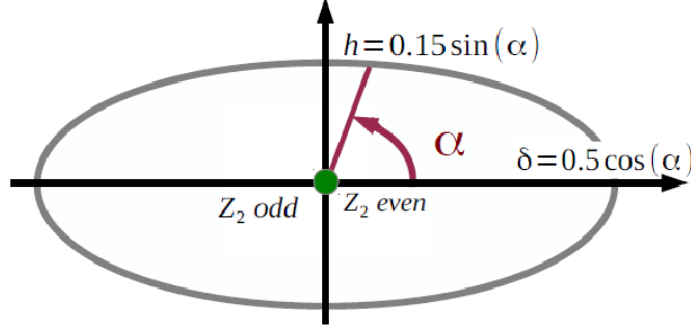


Figure 5.1: The adiabatic loop connecting the  $Z_2$ -odd and  $Z_2$ -even phase in FKM tight-binding model.

## 5.2 Tight-binding Model

We now illustrate the concepts introduced above in the context of a simple tight-binding model. Following Essin *et al.*, [48] we start with the Fu-Kane-Mele (FKM) model, [1] which is a four-band model of  $s$  orbitals on a diamond lattice with spin-orbit interaction,

$$H_{\text{FKM}} = \sum_{\langle ij \rangle} t(\mathbf{e}_{ij}) c_i^\dagger c_j + i\lambda_{\text{so}} \sum_{\langle\langle ij \rangle\rangle} c_i^\dagger \mathbf{s} \cdot (\mathbf{d}_{ij}^1 \times \mathbf{d}_{ij}^2) c_j. \quad (5.30)$$

The first term is a sum over first-neighbor hoppings, where  $\mathbf{e}_{ij}$  is the bond vector, while the second term involves second-neighbor hops in which vectors  $\mathbf{d}_{ij}^{1,2}$  describe the two first-neighbor bonds that make up the second-neighbor hop. We take the cubic lattice constant to be unity. In the original FKM model  $t(\mathbf{e}_{ij}) = t_0$  independent of hopping direction, but following Ref. essin-prl09 we take  $t(\mathbf{e}_{ij}) = t_0(3 + \delta)$  for the bond along (111) and  $t_0$  for the other three bonds. We set the first-neighbor and spin-dependent second-neighbor hoppings to  $t_0 = 1$  and  $\lambda_{\text{so}} = 1$  respectively, and assume two bands are occupied.

The strong topological and trivial phases are separated from each other by a band touching at the  $\Gamma$  point when  $\delta = 0$ . Again following Essin *et al.* [48] we add a staggered Zeeman field  $h$ , and define an adiabatic loop parametrized by  $\delta(\alpha) = m \cos(\alpha)$  and  $h(\alpha) = m \sin(\alpha)$  where  $\alpha$  runs from 0 to  $2\pi$ , such that the system remains insulating on the loop

---

<sup>1</sup>Note that the integrands in Eqs. (5.25-5.26) are gauge-invariant in the Bloch directions, i.e., unchanged under a phase twist  $\exp(i\varphi_n(k_x, k_y))$ .

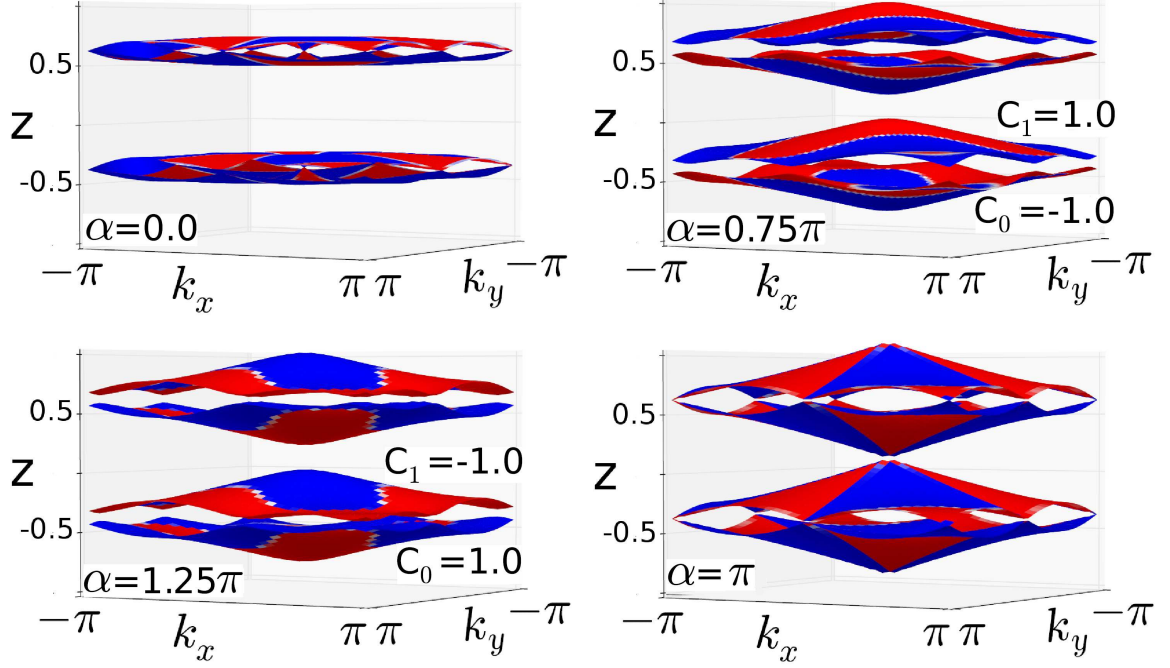


Figure 5.2: The two WCC sheets of the half-filled FKM model, and one set of periodic images, at four stages  $\alpha = (0, 3\pi/4, \pi, 5\pi/4)$  along the parametric cycle (clockwise from upper left). Blue and red colors show positive and negative values of Berry curvature  $\Omega_z$  on the sheets. The Chern numbers associated with the individual WCC sheets are shown for those cases where sheets do not touch.

and  $\theta$  is pumped by  $2\pi$ . The HWF representation is constructed with  $\hat{z}$  along the (111) direction.

### 5.3 WCC Sheets' Evolution

The WCC sheets derived from the two occupied bands in the FKM model are shown in Fig. 5.2, where one pair of sheets and one copy of their periodic images along  $\hat{z}$  are shown for some points around the adiabatic loop.<sup>2</sup> The evolution of the Wannier sheet positions is plotted in Figs. 5.4(a-b) at the four TRI points, namely at the BZ center  $\Gamma$  and at the three equivalent  $M$  points, e.g.,  $(\pi, \pi)$ .

For  $B = 0$ , the system has TR symmetry at  $\alpha = 0$  and  $\pi$ , where the system is  $Z_2$ -even and  $Z_2$ -odd respectively, and where the WCC sheets pair up at the four TRI-points due

<sup>2</sup>We use the “periodic” convention on the Bloch function coefficients in the sense of Ref. dobardzic-arxiv to insure that the Berry curvature respects the symmetry of the system.

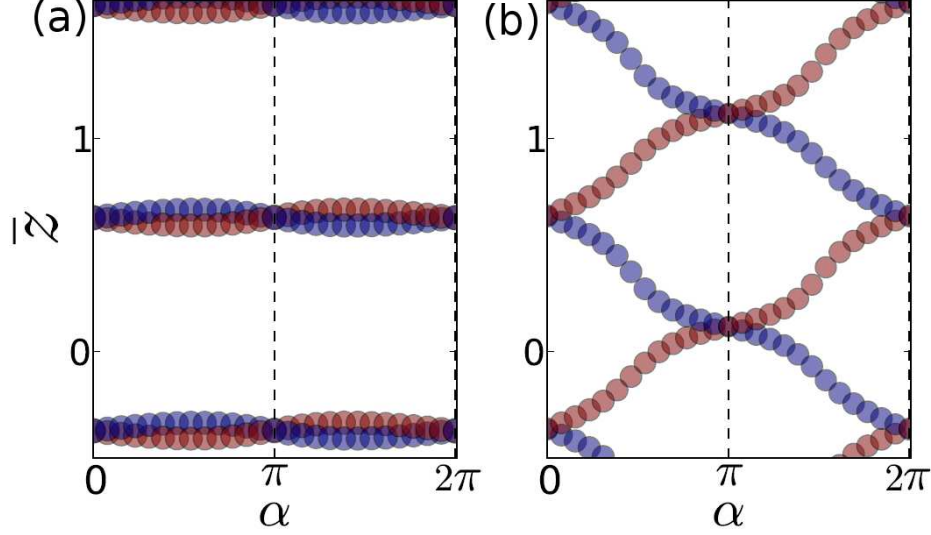


Figure 5.3: The WCCs at the (a)  $M$ -point and (b)  $\Gamma$ -point as they evolve around the adiabatic loop. Blue and red colors show positive and negative values of Berry curvature at these points.

to Kramers degeneracy.[49] In the normal phase at  $\alpha = 0$  this results in a pair of sheets connected by Dirac points at all four TRI momenta, and each pair is well separated from its neighbors along  $\hat{z}$ . As  $\alpha$  increases, the Dirac crossings are gapped and the sheets begin to separate. At the three  $M$  points the separation between the pair remains quite small, and the same sheets touch again at  $\alpha = \pi$ , as is obvious from Fig. 5.4(a). At the  $\Gamma$  point, however, the sheets separate strongly and eventually reconnect with their neighbors from the next unit cell along  $\hat{z}$  when  $\alpha = \pi$ . The swapping of partners at an odd number of the TRI points (here, only at  $\Gamma$ ) is characteristic of the strong topological ( $Z_2$ -odd) phase at  $\alpha = \pi$ . Note, however, that the WCC sheets, taken together, have no net displacement along the  $\hat{z}$  direction, so no charge is pumped.

#### 5.4 CSA Coupling Pump

Now we ask what happens to the CSA coupling  $\theta$  during this cycle, and to do this we inspect the Berry curvature  $\Omega_{xy}$  on the sheets. This is represented by the color-scale shading in Figs. 5.2 and 5.3. Recall that the evolution of  $\theta$  is expected to be reflected in the behavior

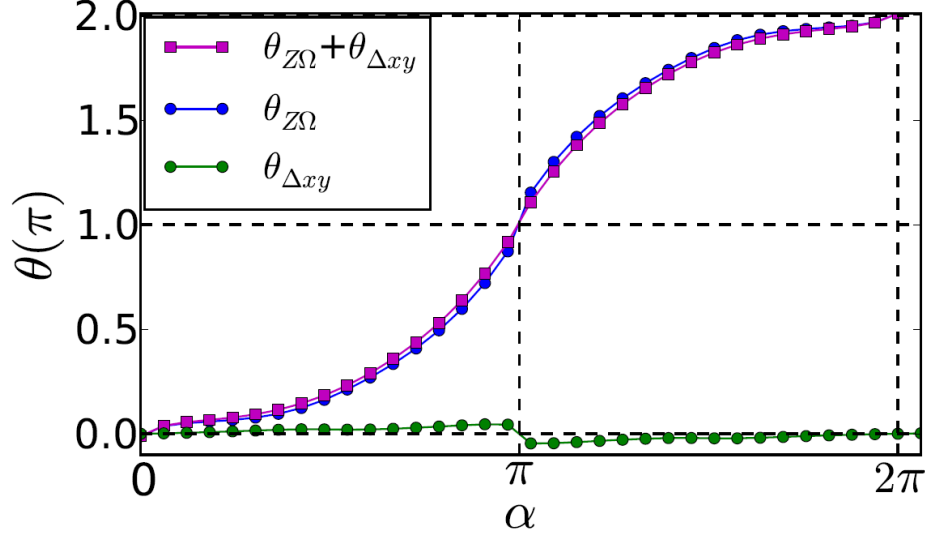


Figure 5.4: The CSA coupling  $\theta(\alpha)$ , and the contributions of the topological term  $\theta_{z\Omega}$  and the correction term  $\theta_{\Delta xy}$ , for the FKM model as it evolves around the adiabatic loop.

of the  $\theta_{x\Omega}$  term as given by Eq. (5.25). We immediately see that the behavior near the  $M$  points is uninteresting; positive and negative Berry curvature contributions separate slightly at first, but they then reverse and recross, and never give a large contribution to  $\theta_{z\Omega}$ .

Near  $\Gamma$ , however, the story is strikingly different. A negative (red) increment of Berry curvature is transported along  $+\hat{z}$  while a positive (blue) contribution is carried along  $-\hat{z}$  as  $\alpha$  evolves from 0 to  $\pi$ . For small and positive  $\alpha$  we intuitively expect that the total Berry curvature near  $\Gamma$  in the top and bottom sheets (at  $\bar{z}_2$  and  $\bar{z}_1$ ) should be  $-\pi$  and  $\pi$  respectively, characteristic of a weakly gapped Dirac point. Thus the contribution to the Berry curvature dipole term  $\theta_{z\Omega}$  from the vicinity of  $\Gamma$ , which is approximately  $\pi(\bar{z}_2(0,0) - \bar{z}_1(0,0))/c$ , grows gradually as  $\alpha$  increases and the sheets get further apart at  $\Gamma$ . As  $\alpha \rightarrow \pi$  the separation between the sheets at  $\Gamma$  approaches a full lattice constant  $c$  and the contribution to  $\theta_{z\Omega}$  approaches  $\pi$ . This expectation is confirmed in Fig. 5.4, where we plot the evolution of  $\theta$  *vs.*  $\alpha$ , and also its two individual contributions  $\theta_{z\Omega}$  and  $\theta_{\Delta xy}$ , as computed from Eqs. (5.25-5.26). Compared to  $\theta_{z\Omega}$ , the non-topological  $\theta_{\Delta xy}$  term is almost negligible everywhere around the adiabatic loop, with the possible exception of the vicinity of the  $Z_2$ -odd phase where it reverses suddenly, as a result of the WCC sheets from adjacent

layers coming close to each other at the  $\Gamma$ -point.

As  $\alpha$  passes through  $\pi$  there is a Dirac touching at  $\Gamma$  between sheet 2 in the home cell and sheet 1 in the cell above, with a hand-off of  $-2\pi$  units of Berry curvature (or a Chern number of  $-1$ ) from the former to the latter, and with the concentration of Berry curvature near  $\Gamma$  in band 2 switching from  $-\pi$  to  $\pi$ . A direct evaluation of Eq. (5.25) would show  $\theta_{z\Omega}$  and  $\theta$  dropping discontinuously by  $2\pi$  as  $\alpha$  crosses through  $\pi$ , but we make use of the gauge freedom to apply a  $2\pi$  shift of  $\theta$  to impose physical continuity when drawing the curves in Fig. 5.4.

Here we have illustrated the behavior of just one model system, and we have found that the pumping of  $\theta$  by  $2\pi$  is accomplished by a series of touching events between WCC sheets, such that one Chern number of Berry curvature is handed off to the neighboring sheet with each touching. But it is now clear in retrospect that *any cycle that pumps  $\theta$  by  $2\pi$  must involve such a sequence of touching events*. For, if these events did not occur, the CSA coupling could not be passed along by a lattice vector during the cycle. Incidentally, this observation also explains why a non-trivial  $\theta$  pumping cycle is impossible in a system with a single occupied band, since in this case the WCC sheets are always separated by  $c\hat{z}$  and can never touch.

## 5.5 Symmetries

In Chapter 3, we showed that the  $\bar{z}_n$  respect all the symmetries of the crystal in the  $(k_x, k_y)$  plane, including time reversal symmetry. On the other hand,  $\Omega_{xy,0n,0n}(k_x, k_y)$  is an odd function of  $(k_x, k_y)$  in the 2D BZ. Consequently, in a system with TR-symmetry the Berry curvature dipole term usually vanishes since  $\bar{z}_n(k_x, k_y)\Omega_n(k_x, k_y)$  is odd under TR-symmetry and its integral over the projected BZ should vanish. It can also be shown that  $\theta_{\Delta xy}$  vanishes in this case, which would appear to imply that  $\theta = 0$  for both normal and strong  $Z_2$ -odd TRI insulators. However, there is a subtlety at the TRI-points where two WCC sheets touch. At these points  $\Omega_{xy,0n,0n}(k_x, k_y) = -\Omega_{xy,0m,0m}(k_x, k_y)$ , where  $n$  and  $m$  are the band indices for

the two sheets which make up a pair in the home unit cell  $l = 0$ . Therefore the contribution of berry curvature at a TRI-point to the CSA coupling is  $\Omega_{xy,0n,0n}(k_x, k_y)(\bar{z}_n(k_x, k_y) - \bar{z}_m(k_x, k_y))$ . This expression vanishes at all the TRI-points in the  $Z_2$ -even phase as can be seen from Fig. 5.2, but in the strong  $Z_2$ -odd phase the two sheets exchange partners at  $\Gamma$  point and  $\bar{z}_n(0,0) - \bar{z}_m(0,0) = c$  which gives rise to the non-zero value of  $\theta_{z\Omega}$  at this phase.

When TR is broken, the value of  $\theta_{z\Omega}$  will depend on the choice of WCC sheets assigned to the “home unit cell” ( $l = 0$ ) if some sheets have non-zero Chern numbers  $C_n$ . That is, a shift of sheet  $n$  by  $c\hat{z}$  displaces  $2\pi C_n$  units of Berry curvature by the same distance, changing the dipole term  $\theta_{z\Omega}$  by  $-2\pi C_n$ . Thus, we see that our formalism is consistent with the fact that  $\theta$  is only well-defined modulo  $2\pi$ , and we identify the dipole contribution  $\theta_{z\Omega}$  as the “topological” term associated with this indeterminacy.

## 5.6 Perturbations

To make the model more generic, we also add a small uniform magnetic field  $B$  and a staggered on-site energy  $\epsilon$  to break the TR and inversion symmetries of the system, checking that the loop in  $(\delta, h)$  space remains insulating.<sup>3</sup> The full Hamiltonian is then

$$\begin{aligned} H(\alpha) &= H_{\text{FKM}}(\alpha) + \mathbf{h}(\alpha) \cdot \sum_i \xi_i c_i^\dagger \mathbf{s} c_i \\ &+ \mathbf{B} \cdot \sum_i c_i^\dagger \mathbf{s} c_i + \epsilon \sum_i \xi_i c_i^\dagger c_i, \end{aligned} \quad (5.31)$$

where  $\xi_i = \pm 1$  for  $i$  on sublattice A and B respectively, and  $\mathbf{h}$  and  $\mathbf{B}$  are along (111). Because of the  $B$  and  $\epsilon$  terms, the system is no longer exactly TRI at  $\alpha = 0$  and  $\pi$ , but we can still think of these as being loosely identified with the  $Z_2$ -even and  $Z_2$ -odd states respectively.

Adding a small staggered on-site energy,  $\epsilon$ , breaks the inversion symmetry of the FKM

---

<sup>3</sup>There is a band closure along a 1D curve in the 4D parameter space  $(\delta, h, B, \epsilon)$ , so we ensure that our loop in  $(\delta, h)$  for fixed  $B$  and  $\epsilon$  encircles this curve.

model but leaves the system TRI, thereby it doesn't alter the simultaneous touching events at  $\Gamma$  and  $M$  points when the system is at the  $\alpha = 0$  or  $\pi$ . Conversely, a small uniform magnetic field  $\mathbf{B}$  ensures that the TR-invariance of the system is broken everywhere along the loop, so the WCC sheet do not need to have double-degeneracy at TRI points at  $\alpha = 0$  and  $\pi$  any more. However, when the system is evolving along a topological non-trivial cycle which pumps the  $\theta$ -coupling, the WCC sheets need to go under some touching events along the loop. In the particular case of FKM model, the 3-fold rotational symmetry of the system keeps the touching events at  $\Gamma$  point in place and they still happen at  $\alpha = 0$  and  $\pi$ , but the touching events at the three  $M$ -points move slightly away from those points in the projected BZ, and they happen at  $\alpha = -\varepsilon$  and  $\pi + \varepsilon$ , where  $\varepsilon$  is a very small parameter depending on the TRI-breaking field  $\mathbf{B}$ .

## 5.7 Slab Configuration

One can also consider the corresponding evolution of the Berry curvatures and Chern transfers for finite slabs, where the bulk of the slab undergoes the same cyclic evolution. If the surface Hamiltonian could be constantly readjusted so as to remain insulating, the net result at the end of the cycle would be to change the surface AHC by  $\pm e^2/h$  at the bottom and top surfaces of the slab respectively. In the more common case that the surface returns to its initial state at the end of the cycle, the AHC must return to itself too, so the slab is topologically required to have a metallic surface phase over some interval of  $\alpha$ . During this  $\alpha$  interval, the surface AHC changes continuously with changing filling in such a way as to contribute  $\mp e^2/h$  by the time the surface band is completely filled or depleted, removing the extra Chern number pumped from the bulk. The existence of such surface states can be an experimental signature characterizing any adiabatic loop with non-zero second Chern number.



## 5.8 Summary

In summary, we have demonstrated that the WCC sheets as defined in the HWF representation, which had previously been shown to be useful for identifying and visualizing the topological properties of non-trivial insulating phases, also provides an insightful characterization of a non-trivial parametric loop characterized by a second Chern number. By defining Berry connections and curvatures associated with the WCC sheets, we have derived a new formula for the CSA axion coupling  $\theta$  as a decomposition into a topological Berry curvature dipole term and a non-topological correction term. In this kind of adiabatic cycle it is not the charge, but the sheet Berry curvature, that is pumped during the cycle. In our formulation the  $2\pi$  ambiguity of  $\theta$  is readily evident when some sheets have non-zero Chern numbers, in which case a different assignment of sheets to the home unit cell can shift  $\theta$  by  $2\pi$ , and the link to the surface anomalous Hall conductivity becomes more direct. We also speculate that Eqs. (5.25-5.26) may provide a more efficient practical means of computing  $\theta$  than those used previously, since there is no need to establish a smooth gauge in the 3D Brillouin zone. In any case, we believe that our extended development of the HWF representation should prove broadly useful in characterizing the adiabatic evolution of topological materials and their magnetoelectric properties.

## Chapter 6

### Bloch-type Ferroelectric Domain Walls in BaTiO<sub>3</sub>

Ferroelectrics find many industrial and commercial applications, such as in high-dielectric constant capacitors, ferroelectric thin-film memories, piezoelectric transducers, nonlinear optical devices, and switches. The performance of many kinds of ferroelectric devices is affected by the ferroelectric domain structure and the properties of the domain boundaries. For example, a recent experiment has shown that the observed dielectric permittivity of a BaTiO<sub>3</sub> single crystal in the rhombohedral phase varies depending on the domain structures induced by pre-treatments at higher temperatures [52]. Such influences on the mechanical and electrical properties of devices has motivated theoretical and experimental work directed toward obtaining a better understanding of ferroelectric domain structures.

Ferroelectric domain walls (FDWs) are usually considered to be of Ising type, in which  $\mathbf{P}_{\parallel}$ , the projection of the polarization vector onto the plane of the domain wall, simply reverses itself by passing through zero along a high-symmetry path as one scans through the domain wall. Ising FDWs tend to be favored because ferroelectrics are generally strongly electrostrictive, so that a rotation of  $\mathbf{P}_{\parallel}$  away from this high-symmetry path would entail a significant elastic energy cost. In contrast, the spontaneous magnetostriction which couples the magnetization and lattice strain in ferromagnetic materials is typically much weaker. As a result, magnetic domain walls are usually much wider, on the order of microns, and the magnetization vector can rotate away from the high-symmetry path. The domain wall is denoted as a Bloch or Néel wall depending on whether this rotation occurs in a plane parallel or normal to the domain wall, respectively.

In recent years, however, there have been some theoretical predictions of the presence of

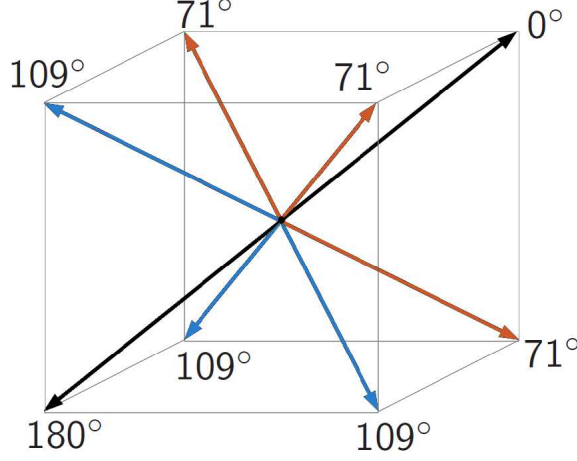


Figure 6.1: The directions of the symmetry-allowed spontaneous polarizations in rhombohedral  $\text{BaTiO}_3$ . Angles are relative to the reference direction labeled as  $0^\circ$ .

Bloch and even Néel components in some ferroelectric materials and heterostructures [53–55]. In particular, it has been predicted, in the framework of a phenomenological Ginzburg-Landau-Devonshire (GLD) model, that the  $180^\circ$  FDWs in rhombohedral  $\text{BaTiO}_3$  should be of Bloch type [56]. This work has motivated us to test whether this behavior is also reproduced by first-principles density-functional calculations on  $\text{BaTiO}_3$ .

Since the discovery of ferroelectricity in this material in 1945 [57],  $\text{BaTiO}_3$  has been very widely studied and has emerged as a kind of prototypical ferroelectric compound. It undergoes a sequence of phase transitions from a high-temperature paraelectric cubic phase to ferroelectric tetragonal, orthorhombic, and finally rhombohedral phases as the temperature is reduced. Here we are interested in the zero-temperature rhombohedral phase, in which the spontaneous polarization prefers to lie in eight energetically equivalent directions, as shown by the arrows in Fig. 6.1. The figure also shows the possible rotation angles between the spontaneous polarization directions on the two sides of the domain wall (relative to the arrow marked as ‘0’). In the low-temperature rhombohedral phase of  $\text{BaTiO}_3$ , the FDWs are therefore of three types:  $\text{R}71^\circ$ ,  $\text{R}109^\circ$ , and  $\text{R}180^\circ$ . (The ‘R’ denotes a FDW in the rhombohedral phase, following the notation of Ref. Marton.) Taking into account the constraints of electrical neutrality and mechanical compatibility, the plane of

the FDW is normal to the sum of the two polarization vectors for the  $R71^\circ$  and  $R109^\circ$  cases, while for the  $180^\circ$  case it can be either  $\{\bar{2}11\}$  or  $\{1\bar{1}0\}$ .

In this chapter the  $R71^\circ$ ,  $R109^\circ$ , and  $R180^\circ\{1\bar{1}0\}$  FDWs in  $\text{BaTiO}_3$  are investigated using first-principles calculations in the context of density-functional theory and a GLD model [56]. In Sec. 6.2 we describe the geometry of each of the FDWs to be studied. We also review the first-principles and GLD model approaches which are used to study the FDWs, and give the details of the methods used for the first-principles calculations. The results from the first-principles calculations and their comparison to the GLD model are then described in Sec. 6.3. In Sec. 6.4 we discuss the competition between Ising and Bloch configurations in terms of energy considerations, and in Sec. 6.5 we briefly summarize and discuss future prospects.

## 6.1 Domain wall and supercell geometries

The mechanically compatible and electrically neutral FDWs investigated in this chapter are shown in the left column of Fig. 6.2, where the arrows indicate the orientation of the polarization vectors  $\mathbf{P}(-\infty)$  and  $\mathbf{P}(\infty)$  on the two sides of the domain wall. In the right column, the symmetry-adapted coordinate system  $(r, s, t)$  is shown for each of these walls. The unit vector normal to the wall is denoted by  $\mathbf{s}$ . The second unit vector  $\mathbf{r}$  is chosen to be parallel to  $\mathbf{P}(\infty) - \mathbf{P}(-\infty)$ , the difference between the spontaneous polarizations on the two sides of the wall; electrically neutrality implies that this is normal to  $\mathbf{s}$ . The third basis vector is defined as  $\mathbf{t} = \mathbf{r} \times \mathbf{s}$ .

For the application of the GLD continuum approach, atomistic details are not important, and specific atomistic geometries do not have to be considered. This is obviously not the case, however, for the first-principles calculations. These are set up by considering a supercell that is extended along the direction  $\mathbf{s}$  normal to the wall, keeping minimal dimensions in the orthogonal directions. Ideally we would prefer a supercell containing only a single domain wall, but this is incompatible with periodic boundary conditions. Thus, we use

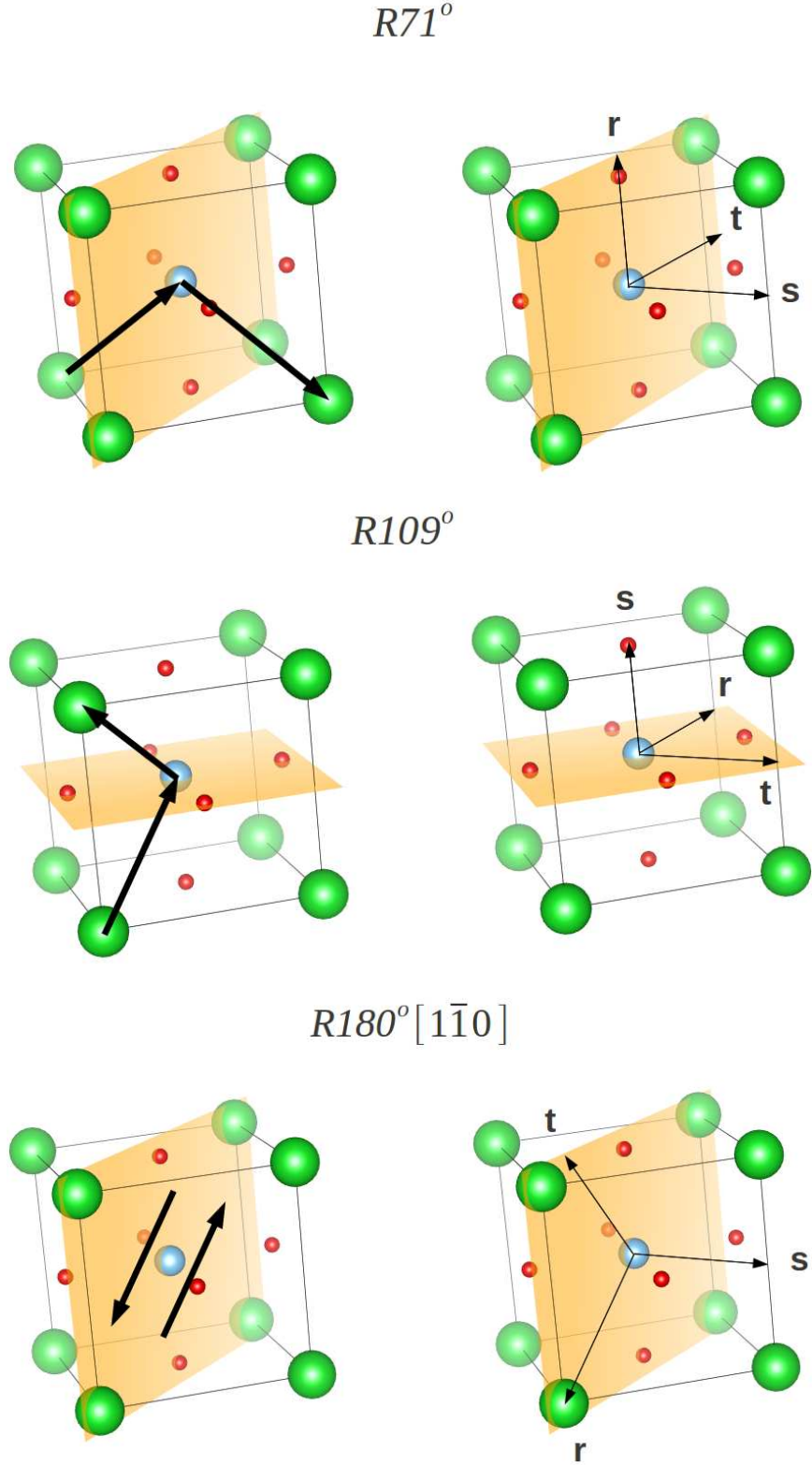


Figure 6.2: The  $R71^\circ$ ,  $R109^\circ$  and  $R180^\circ\{1\bar{1}0\}$  FDWs in  $\text{BaTiO}_3$ . The arrows in the figures at left show the directions of the polarization vectors on the two sides of the FDW, while those on the right depict the associated symmetry-adapted coordinate system  $(r, s, t)$ .

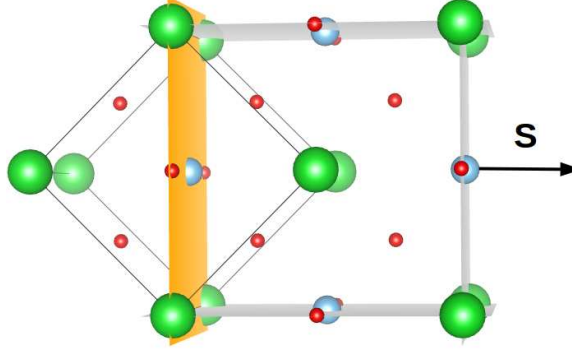


Figure 6.3: 10-atom rotated building block that is stacked along  $\mathbf{s}$  to construct supercells for studying  $R71^\circ$  and  $R180^\circ\{1\bar{1}0\}$  FDWs, which lie normal to  $\mathbf{s}$ .

supercells containing two equivalent FDWs, where we enforce this equivalence by imposing a two-fold screw symmetry (two-fold rotation about  $\mathbf{s}$  followed by a half superlattice-vector translation along the stacking direction  $\mathbf{s}$ ). If these walls are well separated, their effect on each other should be small and the physical properties of the walls should be unaffected.

We first construct a reference paraelectric supercell by identifying a minimal building block having lattice vectors parallel to  $\mathbf{r}$ ,  $\mathbf{s}$  and  $\mathbf{t}$ , and repeating this block  $N$  times along the stacking direction  $\mathbf{s}$ . An example of such a building block, used for the  $R71^\circ$  and  $R180^\circ\{1\bar{1}0\}$  cases, is shown in Fig. 6.3, and an example of a supercell built from it is shown in Fig. 6.4. An initial configuration for an Ising FDW is then chosen by shifting the coordinates of the oxygen atoms along the  $\mathbf{P}(-\infty)$  direction in the first half of the supercell, and along  $\mathbf{P}(\infty)$  in the second half. For the  $R71^\circ$  and  $R109^\circ$  cases this results in a configuration with a mirror symmetry relating the  $-\mathbf{t}$  and  $\mathbf{t}$  directions, and since this symmetry is preserved by the subsequent relaxation of atomic coordinates, the resulting relaxed configuration is guaranteed to be of Ising type. To initialize a calculation on a Bloch FDW, we also add oxygen displacement components along  $\mathbf{t}$  in one FDW and along  $-\mathbf{t}$  in the other (still preserving the screw symmetry), so that effectively the displacement vector in the  $\mathbf{r}$ - $\mathbf{t}$  plane is rotated from the  $\mathbf{r}$  to the  $\mathbf{t}$  direction across the wall before pointing to  $-\mathbf{r}$  on the other side of the wall. In both the Ising and Bloch cases, the  $\mathbf{s}$  component is left unchanged in the initial configuration, although of course it may relax later.

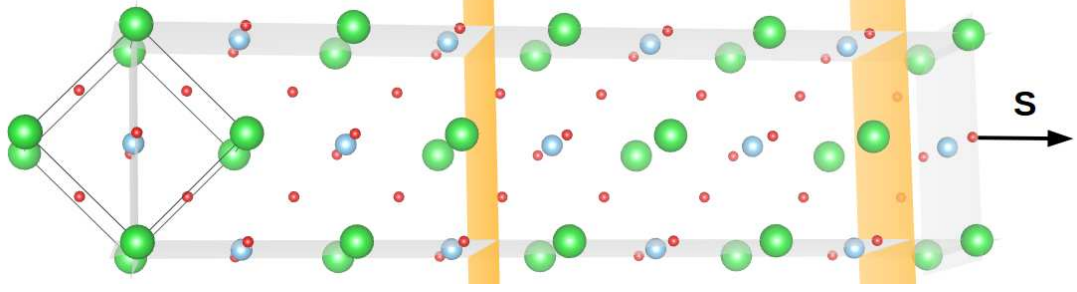


Figure 6.4: A supercell with four rotated 10-atom units stacked in the  $s$  direction. The centers of the FDWs are shown by the orange planes.

We then relax the atomic coordinates until all of the forces fall below a chosen threshold. While doing this, we constrain the two in-plane lattice vectors (i.e., in the plane of the FDW) to remain fixed, consistent with the relaxed strain state of a single-domain rhombohedral crystal. We do this because the physical system we are trying to model is an isolated FDW between very thick domains, in which case the bulk elasticity dominates over the interface and fixes the in-plane strain. We let the third (long) superlattice vector relax along with the atomic coordinates during the minimization. Finally, the polarization profile is calculated from the pattern of displacements and the calculated dynamical effective charges as described in Sec. 6.2.1 below.

For all the investigated FDWs, we can always find an Ising-type FDW solution if we impose an appropriate symmetry constraint. To test whether this solution is locally stable, we add small symmetry-lowering atomic displacements, and check whether it relaxes back to the Ising solution. We next try starting from a Bloch-type configuration, with substantial distortions similar to those that would be present in well-defined domains of rhombohedral phase. Again, if this structure relaxes back to the Ising one, then we conclude that no Bloch FDW was found, and the Ising solution is stable. If we find instead that the calculation converges to a Bloch-like solution, we compare its energy with that of the Ising solution (if locally stable) to determine which is the global solution.

The  $R71^\circ$  wall has its normal  $\mathbf{s}$  in the  $[1\bar{1}0]$  direction, so that it lies parallel to the diagonal plane in the primitive cell as shown in Fig. 6.2. Therefore, we consider the building block of

Fig. 6.3, which is a 10-atom  $\sqrt{2} \times \sqrt{2} \times 1$  cell obtained by rotating by  $45^\circ$  around the  $z$  axis with respect to the parent cubic unit cell. In this rotated cell, the FDW lies in the (100) plane. The simulation supercell is constructed by stacking these units in the  $\mathbf{s}$  direction, as shown in Fig. 6.4. The initial coordinates for the Ising  $R71^\circ$  FDW simulation are then obtained by shifting the oxygen atoms by about  $0.1 \text{ \AA}$  along  $[101]$  in half the supercell, and along  $[10\bar{1}]$  in the other half, in the rotated coordinate system.

The  $R109^\circ$  FDW lies in the (100) plane,  $\mathbf{s} = \hat{x}$ , and a supercell can easily be made by stacking the primitive 5-atom rhombohedral cells in this direction. The initial Ising configuration is then set by displacing the oxygen atoms from the equilibrium positions along the  $[111]$  direction on one side of the FDW, and along the  $[1\bar{1}\bar{1}]$  direction on the other side.

The  $R180^\circ\{1\bar{1}0\}$  wall is again parallel to the diagonal plane in the primitive cell, as for the  $R71^\circ$  domain wall. So in this case as well, a supercell is made by stacking the rotated 10-atom units shown in Fig. 6.3 in the  $\mathbf{s}$  direction. The initial configuration for the  $R180^\circ\{1\bar{1}0\}$  Ising FDW is obtained by shifting the oxygen atoms from their equilibrium positions along the  $[011]$  direction on one side of the FDW and along the opposite direction on the other side, in the rotated coordinate system.

For the Ising  $R180^\circ\{1\bar{1}0\}$  case there is also the possibility of imposing a higher symmetry by insisting that the FDW lie exactly in a Ba-Ti-O plane, or exactly in an O-O plane, which can be accomplished by adopting an inversion center through one of the atoms lying in the FDW. This is not possible for the  $R71^\circ$  and  $R109^\circ$  FDWs, since the presence of a global  $P_s$  component makes the “front” and “back” sides of the FDW distinguishable and rules out the presence of an inversion symmetry.



## 6.2 Computational Approach

### 6.2.1 First-principles calculations

The calculations are done using the ABINIT implementation of density functional theory [58] within the local-density approximation (LDA) using the Perdew-Zunger exchange-correlation functional [59]. Ultrasoft pseudopotentials,[60] in which semicore  $s$  and  $p$  states are included in the valence for Ba and Ti, were converted for use as projector augmented-wave (PAW) potentials [61] using the USPP2ABINIT package. The plane wave cut-off and the energy cut-off for the fine FFT grid are set to 25 Ha and 40 Ha respectively. The tolerance on the difference of forces in successive iterations in a self-consistent-field (SCF) cycle is set to  $5.0 \times 10^{-10}$  hartree/Bohr, which reached twice successively, causes one SCF cycle to stop and ions to be moved. The structural optimizations are done using the Broyden-Fletcher-Goldfarb-Shanno minimization [62–65].

The supercells employed for studying R71° and R180° FDWs are of dimensions  $\sqrt{2}Na \times \sqrt{2}a \times a$ , where  $a$  is the primitive lattice constant and  $N$  is the number of 10-atom units stacked in the  $\mathbf{s}$ -direction. Therefore, a  $1 \times 4 \times 6$  Monkhorst-Pack [66]  $k$ -mesh is chosen for simulating these domain walls. The supercell for the R109° FDW is made by stacking the 5-atom primitive cells in one direction, so a  $1 \times 6 \times 6$  Monkhorst-Pack [66]  $k$ -mesh seems a proper choice for simulating this FDW.

We also compute the dynamical effective charges [67]  $Z^*$  in bulk paraelectric cubic BaTiO<sub>3</sub>.<sup>1</sup> The dynamical charge tensor  $Z_{i\alpha,\beta}^*$  of a given atom measures the dipole induced along  $\beta$  by a displacement of atom  $i$  along  $\alpha$ . In many oxides including BaTiO<sub>3</sub>, these charges are quite different from the formal ionic charges. The  $Z^*$  tensors are computed by finite differences, i.e., by making small displacements and calculating the resulting change in Berry-phase polarization [68].

---

<sup>1</sup>The dynamical effective charge tensors in the rhombohedral phase are anisotropic and depend on the rhombohedral axis. We thus use the cubic tensors instead; we judge this to be a reasonable approximation within the intended accuracy of our calculations.

These dynamical charges are then used as an ingredient in an algorithm [53] by which we map out the polarization profiles in FDW-containing supercells, as follows. The polarization is only changing along the stacking direction and is constant in the planes normal to this direction. So first the contribution from each layer to the dipole moment in direction  $\alpha$  arising from displacements of atoms  $j$  in direction  $\beta$  is calculated as

$$p_{\alpha}^{(l)} = \sum_{\beta, j \in l} Z_{j\beta, \alpha}^* u_{j\beta} \quad (6.1)$$

where  $l$  is a layer index. In the supercell used for studying the R109° FDW these are Ba-O and Ti-O-O layers, while for the R71° and R180°{1 $\bar{1}$ 0} FDWs built from the rotated 10-atom units  $l$  refers to Ba-Ti-O and O-O layers. If we break the supercell into smaller cells centered on these layers, we can assign a local polarization to cell  $l$  by counting its own contribution and half that of each neighbor, i.e.,

$$P_{\alpha}^{(l)} = \frac{1}{\Omega} \left( \frac{1}{2} p_{\alpha}^{(l-1)} + p_{\alpha}^{(l)} + \frac{1}{2} p_{\alpha}^{(l+1)} \right), \quad (6.2)$$

where  $\Omega$  is the volume of the cell.

### 6.2.2 The GLD model

We review the Ginzburg-Landau-Devonshire model used in Ref. Hlinka, which is again used here to model the FDW properties and compare with the first-principles results. The excess free energy  $F$  relative to the reference cubic paraelectric state is expressed in terms of polarization and strain fields as

$$F[\{P_i, P_{i,j}, e_{i,j}\}] = \int f(\mathbf{r}) d\mathbf{r}, \quad (6.3)$$

where  $f$  is the GLD free-energy density which is taken to be a function of the polarization components  $P_i$ , their spatial derivatives  $P_{i,j} = \partial P_i / \partial x_j$ , and strain components  $e_{i,j}$ . In

particular,  $f$  is expressed in terms of Landau, elastic, electrostriction, and gradient terms:

$$f = f_L^{(e)}\{P_i\} + f_c\{e_{ij}\} + f_q\{P_i, e_{ij}\} + f_G\{P_{i,j}\}. \quad (6.4)$$

In Ref. Hlinka, explicit forms were given for each of the terms in this expression, parameter values were estimated from the bulk single-crystal properties of BaTiO<sub>3</sub>, and the GLD model was used to investigate domain-wall properties.

Here we are especially concerned with the gradient or Ginzburg terms in the free-energy expansion, which take the form

$$\begin{aligned} f_G = & \frac{1}{2}G_{11}(P_{1,1}^2 + P_{2,2}^2 + P_{3,3}^2) \\ & + G_{1,2}(P_{1,1}P_{2,2} + P_{2,2}P_{3,3} + P_{1,1}P_{3,3}) \\ & + \frac{1}{2}G_{44}[(P_{1,2} + P_{2,1})^2 + (P_{2,3} + P_{3,2})^2 \\ & + (P_{3,1} + P_{1,3})^2]. \end{aligned} \quad (6.5)$$

As discussed in Ref. Hlinka, considerable caution was required in extracting the  $G$  coefficients from inelastic neutron scattering experiments, and the remaining uncertainties are significant. The  $G$  tensor has an important effect on the widths and energies of the FDWs, so that the uncertainties in the values of these coefficients is a limiting factor in determining the properties of the FDWs. The original parameters of Ref. Marton describing the gradient terms are  $G_{11} = 51 \times 10^{-11} \text{ Jm}^3\text{C}^{-2}$ ,  $G_{12} = -2 \times 10^{-11} \text{ Jm}^3\text{C}^{-2}$ , and  $G_{44} = 2 \times 10^{-11} \text{ Jm}^3\text{C}^{-2}$ .

In order to establish a better estimate of these coefficients, the GLD model is employed below to recalculate the polarization profiles of R71°, R109°, and R180°{1 $\bar{1}$ 0} FDWs at zero temperature using modified  $G$  coefficients, and the results are compared with first-principles ones. In order to facilitate the comparisons, these GLD model calculations have been performed on the identical geometries as in the first-principles calculations. That is, we impose periodic boundary conditions corresponding to the size of the first-principles

	$Z_{\text{Ba}}$	$Z_{\text{Ti}}$	$Z_{\text{O} \perp}$	$Z_{\text{O} \parallel}$
Nominal ionic	2	4	-2	-2
$Z^*$ (Exp. [69])	2.9	6.7	-2.4	-4.8
$Z^*$ (LDA )	2.75	7.18	-1.86	-5.65

Table 6.1: The experimental and theoretical values of the dynamical effective charges of the Ba, Ti and O atoms in  $\text{BaTiO}_3$  (in units of the charge quantum  $e$ ).

supercells, impose the same two-fold screw symmetry as was used there, and specify the strain state to be consistent with infinite domains.

### 6.2.3 Domain-wall width

In the case of a domain wall whose polarization profile can be fit to a hyperbolic tangent,  $p(x) = p_0 \tanh(x/\xi)$ , a common definition of the width is  $w = 2\xi$ . However, some of the domain walls to be studied here have unusual polarization profiles that do not resemble a single hyperbolic tangent at all. To accommodate such cases, we define  $w$  as the width of the region within which  $|p(x)|/p_0 < \tanh(1) = 0.762$ . This definition has the advantages of being globally reasonable and of reducing to the conventional definition above when the FDW does resemble a hyperbolic tangent. We adopt this definition throughout the remainder of this work.

## 6.3 Results

$\text{BaTiO}_3$  has been studied extensively both experimentally and theoretically. Our first-principles computed values of 3.95 Å for the lattice constant and 89.93° for the rhombohedral angle can be compared with experimental values [70] of 4.00 Å and 89.87°, respectively. Our results are consistent with the experience that the LDA typically gives slightly underestimated values for the unit-cell volume and ferroelectric distortion [71].

We have also computed the values of the dynamical charge tensors for cubic paraelectric  $\text{BaTiO}_3$ , to be used as an ingredient in the algorithm for computing polarization profiles as described in Sec. 6.2.1. The calculated values of  $Z^*$  for Ba, Ti and O in  $\text{BaTiO}_3$  are

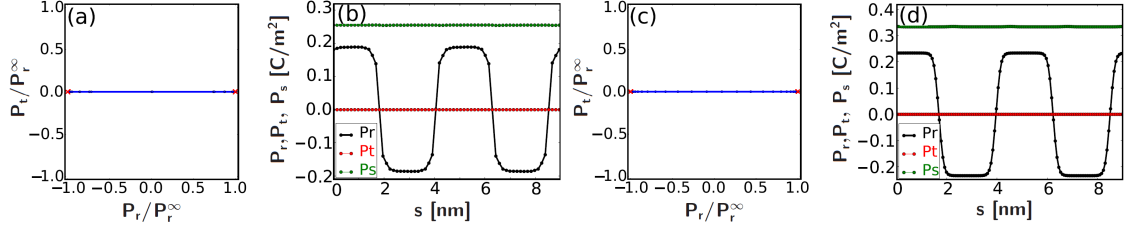


Figure 6.5: Polarization profiles of Ising R71° FDWs in rhombohedral BaTiO<sub>3</sub> as calculated using (a-b) first-principles calculations, and (c-d) the GLD model. Panels (a) and (c): parametric plots showing polarization values in the  $P_r$ – $P_t$  plane. Crosses indicate local energy minima associated with homogeneous rhombohedral domains. Panels (b) and (d): polarization components as a function position  $s$  along the supercell direction (two supercells containing four FDWs are shown for clarity).

compared to the experimental values as well as ionic charges in Table 6.1. The values of  $Z_O \parallel$  and  $Z_O \perp$  refer to the  $Z^*$  of the oxygen ion when it is displaced along the Ti-O direction or perpendicular to it, respectively.

A Berry-phase calculation of the polarization [68] using the relaxed atomic positions in rhombohedral BaTiO<sub>3</sub> yields a value of  $30 \mu\text{C}/\text{cm}^2$ . The polarization calculations using the atomic displacements and the theoretical  $Z^*$  values yields  $31 \mu\text{C}/\text{cm}^2$ , which is slightly underestimated compared to the experimental value [70] of  $33.5 \mu\text{C}/\text{cm}^2$  as expected. The GLD model, on the other hand, yields a value of  $38 \mu\text{C}/\text{cm}^2$ .

In the following subsections, we report the results of our supercell calculations for the R71°, R109°, and R180°{1 $\bar{1}$ 0} ferroelectric domain walls.

### 6.3.1 The R71° domain wall

We have investigated the R71° FDW in rhombohedral BaTiO<sub>3</sub> by carrying out first-principle calculations on an 80-atom supercell made by stacking 10-atom rotated units as described in Sec. 6.1. In this case we only found an Ising FDW; perturbing this by adding symmetry-lowering components only led back to the Ising structure upon further relaxation. The polarization profile computed from the relaxed Ising structure using Eq. (6.2) is displayed in two ways in Fig. 6.5(a-b). The left panel, Fig. 6.5(a), shows the  $P_r^{(l)}$  and  $P_t^{(l)}$  values for each layer  $l$ , while Fig. 6.5(b) shows plots of  $P_r^{(l)}$ ,  $P_s^{(l)}$  and  $P_t^{(l)}$  as a function of position  $s$

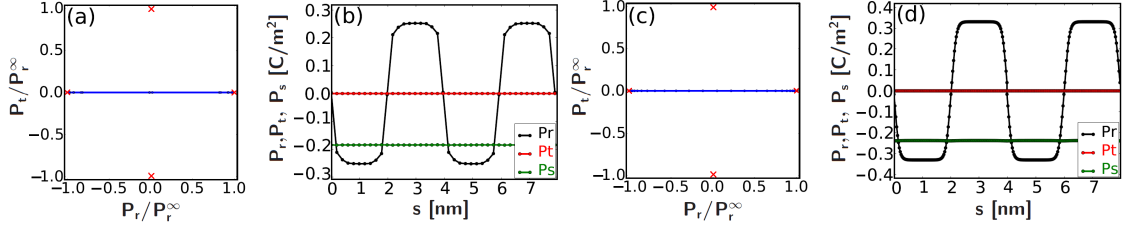


Figure 6.6: Polarization profiles for Ising R109° FDWs in BaTiO<sub>3</sub> using (a-b) first-principles calculations and (c-d) the GLD model. Details are as in Fig. 6.5.

while scanning through a sequence of four domain walls (two entire supercells). As is clear from this figure, the  $P_t$  component remains zero everywhere in the supercell, which clearly indicates the Ising nature of this FDW. The  $P_r$  value reverses quite suddenly and attains a value very close to its saturation bulk value deep inside each domain, indicating a rather narrow FDW width. The  $P_s$  value is almost exactly constant; as we shall see, this is true of all FDWs in this study, consistent with the expectation that inhomogeneities in  $P_s$  would result in bound charge which in turn would involve an extra Coulomb energy cost.

The above results are in good qualitative agreement with those of the GLD model, but the GLD domain-wall width of 0.58 nm is almost twice that of the first-principles prediction of 0.33 nm. This suggests the need for a reduction of the zero-temperature values of the gradient terms in the GLD model to bring it into better agreement with the first-principles results. This reduction of the gradient terms will be even more important in the R180°{110} case, to be discussed in Sec. 6.3.3. As explained there, we have chosen to reduce all three of the gradient coefficients in Eq. (6.5) by 40% in order to arrive at an improved GLD model.

The results computed for the R71° FDW using this modified GLD model are presented in Fig. 6.5(c-d) using the same plotting conventions as for the first-principles results in Fig. 6.5(a-b). The FDW width is now 0.37 nm. Furthermore, the GLD domain-wall energy is reduced from 5.0 to 3.2 mJ/m<sup>2</sup>, to be compared with the first-principles value of 3.8 mJ/m<sup>2</sup>. While these numerical values should be interpreted reservedly in view of the uncertainties in both theories, it is clear that the GLD theory is in better agreement with the first-principles theory after the reduction of the strength of the gradient term.

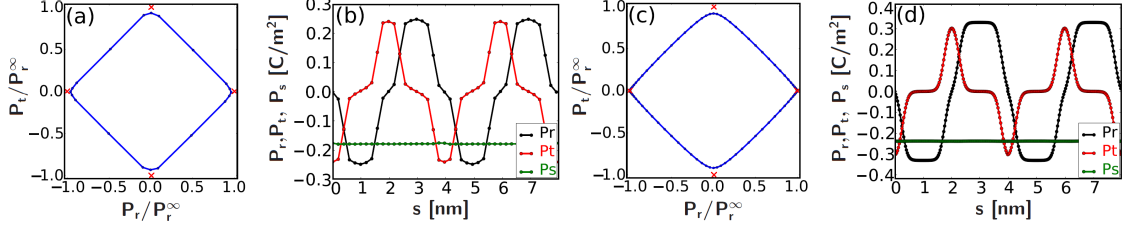


Figure 6.7: Polarization profiles for Bloch R109° FDWs in BaTiO<sub>3</sub> using (a-b) first-principles calculations and (c-d) the GLD model. Details are as in Fig. 6.5.

### 6.3.2 The R109° domain wall

According to the GLD model calculations of Marton *et al.* [56], both Ising and Bloch solutions are possible for the R109° FDW in BaTiO<sub>3</sub>. Our first-principles results confirm this picture.

Starting first with the Ising case, Fig. 6.6(a-b) shows the polarization profile for a 50-atom supercell in which the atomic positions have been relaxed from an initial configuration with two Ising-type R109° FDWs. The domain wall is again fairly narrow, though not quite as narrow as in the R71° case. The energy and width of this Ising R109° FDW are calculated from first principles to be 0.36 nm and 11.1 mJ/m<sup>2</sup>, respectively. The corresponding GLD results using the reduced gradient term, shown in Fig. 6.6(c-d), are clearly in good qualitative agreement.

When the atomic positions are relaxed from an appropriately distorted initial configuration, a Bloch-type solution for this wall is found. The first-principles polarization profiles computed for the Bloch-type R109° FDW in a 50-atom supercell are shown in Fig. 6.7(a-b). To a first approximation, this Bloch FDW can be regarded as a composition of two 71° FDWs in close proximity. In part for this reason, the Bloch-type FDW is clearly broader than the Ising one. However, the energies of the Bloch and Ising solutions are found to be almost identical, with the Ising one being only ~2-3% lower in energy. If we extrapolate to larger separations between FDWs we might expect the Bloch energy to fall more than the Ising one, because of the larger FDW width in the Bloch case. This suggests that both

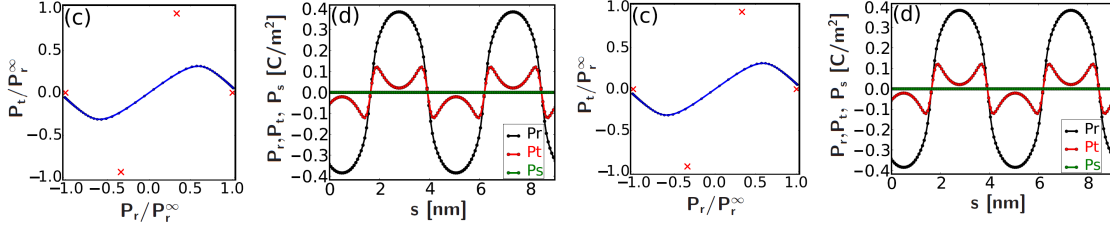


Figure 6.8: Polarization profiles for Ising  $R180^\circ\{1\bar{1}0\}$  FDWs in  $\text{BaTiO}_3$  using first-principles calculations. Details are as in Fig. 6.5.

types of  $R109^\circ$  FDWs have similar energies and that both might be found in rhombohedral  $\text{BaTiO}_3$  crystals. The reason for existence of both Ising and Bloch solutions for the  $R109^\circ$  FDW is discussed in Sec. 6.4. The modified GLD model again gives good qualitative and semiquantitative agreement with the first-principles results for the case of the Bloch  $R109^\circ$  FDW, as shown in Fig. 6.7(c-d).

### 6.3.3 The $R180^\circ\{1\bar{1}0\}$ domain wall

A major result of the GLD study of Marton *et al.* [56], was the prediction that the lowest-energy FDW for the  $R180^\circ\{1\bar{1}0\}$  case in  $\text{BaTiO}_3$  is of Bloch type, with an energy lying 10% lower than that of its Ising counterpart. Verifying this result from first principles is computationally more challenging than studying the  $R71^\circ$  or  $R109^\circ$  FDWs. The  $R180^\circ\{1\bar{1}0\}$  FDW has the biggest rotational angle and is hence the widest of the three investigated FDWs. Moreover, the Bloch-type FDWs are generally much broader than the Ising-type ones. Preliminary first-principles calculations showed that supercells smaller than 80 atoms are too small to accommodate two  $R180^\circ$  FDWs; initial 60-atom Bloch-wall supercells relaxed to unreasonable configurations. We have therefore carried out our calculations on an 80-atom supercell. While the polarization does not quite have room to reach its saturation value between neighboring FDWs, at least we obtain a stable solution that can reveal the Ising or Bloch nature of this FDW.

As mentioned in the last paragraph of Sec. 6.1, it is possible to enforce an Ising-like geometry in the  $R180^\circ\{1\bar{1}0\}$  case by imposing an initial inversion symmetry about an atom



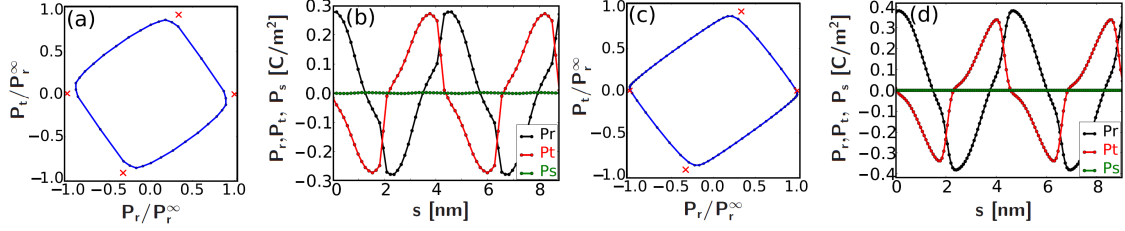


Figure 6.9: Polarization profiles for Bloch  $R180^\circ\{1\bar{1}0\}$  FDWs in  $\text{BaTiO}_3$  using (a-b) first-principles calculations and (c-d) the GLD model. Details are as in Fig. 6.5.

in the center of the FDW and preserving this symmetry during relaxation. When we apply our first-principles calculations including this symmetry constraint, we arrive at a configuration like that shown in Fig. 6.8(a-b), which is Ising-like in the sense that  $P_r = P_t = 0$  in the center of the wall. However,  $P_t$  has substantial excursions away from zero, with the polarization path following an S-like curve in  $(P_r, P_t)$  space, as can be seen clearly in Fig. 6.8(a).

However, we find that if we do not impose this special symmetry, most initial conditions relax to the Bloch configuration shown in Fig. 6.9(a-b). Even if we start from an Ising-like configuration and break the symmetry only slightly, we find that the simulation will eventually relax to the Bloch configuration. It is clear from Fig. 6.9(a-b) that both  $P_t$  and  $P_r$  components are strongly non-zero, and the rotation of the polarization as one progresses through the domain wall, which is the characteristic feature of a Bloch-type wall, is clearly visible. It is also obvious that this Bloch FDW resembles an adjacent pair of  $71^\circ$  and  $109^\circ$  FDWs. We also find that this Bloch wall has a significantly lower energy than that of the Ising-like wall of Fig. 6.8, supporting the conclusion that the Bloch solution is the global minimum for the case of the  $R180^\circ\{1\bar{1}0\}$  FDW.

We have also carried out corresponding simulations of the Ising-like and Bloch configurations of the  $R180^\circ\{1\bar{1}0\}$  FDW using the GLD model. If this is done using the full strength of the gradient term under periodic boundary conditions, we find a stable Bloch solution only when the centers of the domain walls can be at least 3.4 nm apart. This is equivalent to using a supercell of 120 atoms in the first-principles calculations, and imposing the

	Wall width (nm)			Wall energy (mJ/m <sup>2</sup> )		
	LDA	GLD	GLD-r	LDA	GLD	GLD-r
Ising R71°	0.33	0.58	0.37	3.8	5.0	3.2
Ising R109°	0.36	0.54	0.34	11.1	10.6	6.8
Bloch R109°	1.01	1.10	0.72	11.2	10.2	6.2
Ising R180°	0.51	–	0.83	26.6	–	27.2
Bloch R180°	1.38	–	1.40	24.0	–	27.6

Table 6.2: Summary of computed energies and widths of R71°, R109°, and R180°{1 $\bar{1}$ 0} FDWs in BaTiO<sub>3</sub>. LDA indicates first-principles results; GLD and GLD-r refer to the Ginzburg-Landau-Devonshire model with original and reduced gradient term, respectively.

rhombohedral epitaxial strain does not change this result very much. On the other hand, we find that if the gradient term is reduced by about 40%, then stable solutions become possible under the same periodic boundary condition as in the 80-atom supercell. The polarization profiles calculated for the R180°{1 $\bar{1}$ 0} FDWs using the GLD model with reduced gradient term, with the same domain-wall distance and elastic boundary conditions as in the first-principles calculations, are shown in Figs. 6.8(c-d) and 6.9(c-d) for the Ising-like and Bloch cases respectively. The GLD results are clearly now in good qualitative agreement with the first-principles calculations.

The computed energies and widths of all of the FDWs are collected and presented in Table 6.2. It is evident that the first-principles and GLD results are in broad agreement. As expected, the GLD model with reduced gradient term yields narrower walls and lower wall energies, yielding improved agreement for the Ising R71° and R109° cases, but somewhat overshooting for the Bloch R109° case.

For the R180° FDWs, the values given in Table 6.2 ought not be taken too seriously because the repeat distance of the supercell is rather short compared to the FDW width. In fact, we did not succeed in finding stable FDW solutions with the original GLD model. The present 80-atom supercell is large enough to give stable solutions in both the LDA and reduced-GLD calculations, but their properties are undoubtedly not yet converged with supercell size. The FDW energy can be expected to fall with supercell size, so the energies in Table 6.2 should be taken as upper bounds. The “crowding” of the Bloch R180° walls

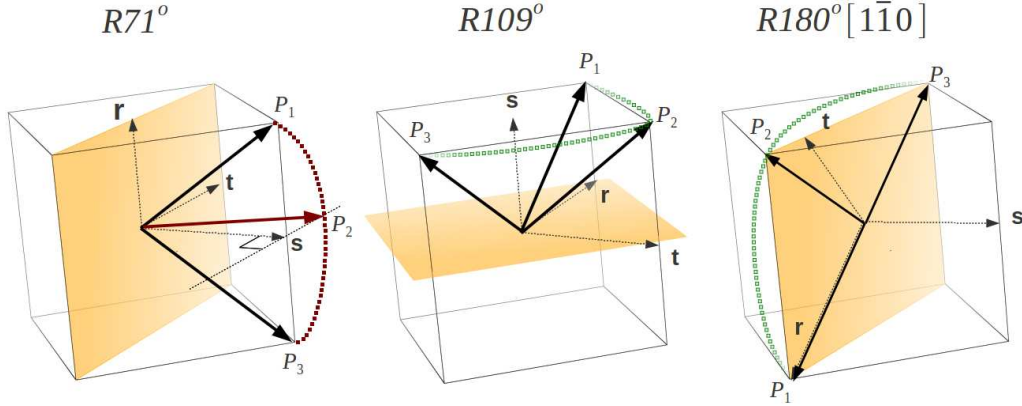


Figure 6.10: The path swept by the tip of the polarization vector while rotating from  $\mathbf{P}_1$  to  $\mathbf{P}_3$  when crossing through hypothetical Bloch-type FDWs for the  $R71^\circ$ ,  $R109^\circ$ , and  $R180^\circ\{1\bar{1}0\}$  geometries. For the  $R71^\circ$  case the path (which rotates in a plane parallel to the FDW) is shown in red to indicate that it is unfavorable.

appears to be more serious than for the Ising ones, which can explain why the reduced GLD model predicts a slightly higher energy for the Bloch compared to the Ising FDW. When the GLD calculations are repeated for larger FDW separations, they clearly predict that the Bloch configuration is lower in energy [56]. The first-principles calculations already predict the Bloch wall to be lower in energy for the 80-atom supercell, and this trend would only be strengthened if we could afford to repeat the calculations at increasingly larger FDW separations such that well-developed rhombohedral domains could form between domains.

#### 6.4 Discussion

Among the three investigated FDWs, the polarization vector rotates by the smallest angle in the  $R71^\circ$  FDW, and by the biggest angle in the  $R180^\circ\{1\bar{1}0\}$  FDW, so it is not surprising that the former has the smallest energy and the latter the biggest, as summarized in Table 6.2. We can also propose a simple explanation for the fact that the first-principles calculations and the GLD model results predict an Ising nature for the  $R71^\circ$  FDW, a Bloch nature for the  $R180^\circ\{1\bar{1}0\}$  FDW, and a very small energy difference between Ising and Bloch solutions for the  $R109^\circ$  FDW. The path the polarization vector would take in rotating from one side

of the wall to the other in a Bloch-type solution is shown for each of these FDWs in Fig. 6.10. In a hypothetical Bloch  $R71^\circ$  FDW the polarization vector would pass close to the center of one of the adjacent faces, which corresponds to a tetragonal polarization state and is not energetically favorable in the rhombohedral phase.

On the other hand, the Bloch  $109^\circ$  FDW can be considered as a combination of two  $R71^\circ$  FDWs. As can be seen from Table 6.2, the total energy of two Ising  $R71^\circ$  FDWs is rather close to the energy of one Ising  $109^\circ$  FDW, from both the LDA and GLD calculations. By way of a caveat, we point out that such a comparison may be overly simplistic because the Ising walls comprising the Bloch  $109^\circ$  FDW experience a foreign strain environment and do not conform to the plane of mechanical compatibility of a true  $R71^\circ$  FDW. Nevertheless, the comparison does hint that we should not be surprised to find the Ising and Bloch configurations to be competitive here. Finally, for the Bloch  $180^\circ\{1\bar{1}0\}$  FDW, which can be regarded as one  $R71^\circ$  FDW plus one  $R109^\circ$  FDW, the LDA calculations indicate that the sum of the energies of these two walls is much lower than that of a single Ising  $180^\circ$  FDW. The above caveat has perhaps even more force here, but again we can roughly understand in these terms why the  $R180^\circ\{1\bar{1}0\}$  FDW can only adopt a Bloch form.

## 6.5 Summary

In conclusion, we have calculated the domain wall widths, energies, and polarization profiles for Ising and Bloch ferroelectric domain walls in the zero-temperature rhombohedral phase of  $\text{BaTiO}_3$  using both first-principles and Ginzburg-Landau-Devonshire methods. The first-principles results confirm the expectation that  $180^\circ$  domain walls are of Bloch type, adopting a configuration resembling a pair of  $109^\circ$  and  $71^\circ$  walls in close proximity. For the case of the  $109^\circ$  wall, Ising and Bloch configurations are competitive. The Ginzburg-Landau-Devonshire results are brought into improved agreement with the first-principles calculations if the coefficient of the gradient term is reduced by about 40%. In view of the uncertainties in the original extraction procedure for the coefficients, it is not surprising

that these parameters can be improved; indeed, it is encouraging that even the original parameters gave qualitatively sound results.

While we have not extended our work to other rhombohedral ferroelectrics such as  $\text{KNbO}_3$ , we expect that these may show a similar pattern of behavior. When instabilities other than ferroelectric ones are also present, the domain-wall behavior can become more complicated, as for example with the octahedral rotations and magnetic ordering that play a role in  $\text{BiFeO}_3$  [72]. However, we hope that the present work will serve as a useful benchmark for domain walls in rhombohedral ferroelectrics generally, and will lead to an improved understanding of ferroelectric domain dynamics and switching in these systems.

## Bibliography

- [1] Fu L, Kane CL, Mele EJ (2007). Phys. Rev. Lett. 98:106803.
- [2] Hohenberg P, Kohn W (1964) Inhomogeneous electron gas. Phys. Rev. 136:B864–B871.
- [3] Kohn W, Sham LJ (1965) Self-consistent equations including exchange and correlation effects. Phys. Rev. 140:A1133–A1138.
- [4] Sporkmann B, Bross H (1994) Calculation of wannier functions for fcc transition metals by fourier transformation of bloch functions. Phys. Rev. B 49:10869–10876.
- [5] Sporkmann B, Bross H (1997). Journal of Physics: Condensed Matter 9:5593.
- [6] Satpathy S, Pawłowska Z (1988) Construction of bond-centered wannier functions for silicon valence bands. physica status solidi (b) 145:555–565.
- [7] Stephan U, Drabold DA, Martin RM (1998) Improved accuracy and acceleration of variational order- $n$  electronic-structure computations by projection techniques. Phys. Rev. B 58:13472–13481.
- [8] Marzari N, Vanderbilt D (1997). Phys. Rev. B 56:12847.
- [9] Thouless DJ, Kohmoto M, Nightingale MP, den Nijs M (1982). Phys. Rev. Lett. 49:405.
- [10] Kane CL, Mele EJ (2005). Phys. Rev. Lett. 95:146802.
- [11] Kane CL, Mele EJ (2005). Phys. Rev. Lett. 95:226801.
- [12] Moore JE, Balents L (2007). Phys. Rev. B 75:121306.
- [13] Fu L (2011). Phys. Rev. L 106:106802.
- [14] Chen YL et al. (2009). Science 325:178.
- [15] Hsieh D et al. (2008). Nature (London) 452:970.
- [16] Xia Y et al. (2009). Nat. Phys. 5:398.
- [17] Analytis JG et al. (2010). Phys. Rev. B 81:205407.
- [18] Hsieh D et al. (2009). Phys. Rev. L 103:146401.
- [19] Park SR et al. (2010). Phys. Rev. B 81:041405.
- [20] Lin H et al. (2010). Nat. Mater. 9:546.
- [21] Hasan MZ, Kane CL (2010). Rev. Mod. Phys. 82:3045.
- [22] Fukui T, Hatsugai Y (2007). J. Phys. Soc. Jpn. 76:053702.

- [23] Soluyanov AA, Vanderbilt D (2011). Phys. Rev. B 83:235401.
- [24] Yu R, Qi XL, Bernevig A, Fang Z, Dai X (2011). Phys. Rev. B 84:075119.
- [25] Fu L, Kane CL (2006). Phys. Rev. B 74:195312.
- [26] Alexandradinata A, Bernevig BA (2012). arXiv:1208.4234.
- [27] Thouless DJ (1984). J Phys. C 17:L325.
- [28] Thonhauser T, Vanderbilt D (2006). Phys. Rev. B 74:235111.
- [29] Soluyanov AA, Vanderbilt D (2011). Phys. Rev. B 83:035108.
- [30] Sgierovello C, Peressi M, Resta R (2001). Phys. Rev. B 64:115202.
- [31] Coh S, Vanderbilt D (2009). Phys. Rev. L. 102:107603.
- [32] Wu X, Diéguez O, Rabe KM, Vanderbilt D (2006). Phys. Rev. L. 97:107602.
- [33] Yao Y, Fu H (2009). Phys. Rev. B 79:014103.
- [34] King-Smith RD, Vanderbilt D (1993) Theory of polarization of crystalline solids. Phys. Rev. B 47:1651–1654.
- [35] Resta R (1994) Macroscopic polarization in crystalline dielectrics: the geometric phase approach. Rev. Mod. Phys. 66:899–915.
- [36] Haldane FDM (1988). Phys. Rev. Lett. 61:2015.
- [37] Delplace P, Li J, Carpentier D (2012) Topological weyl semi-metal from a lattice model. EPL (Europhysics Letters) 97:67004.
- [38] Zhang G et al. (2009). Applied Physics Letters 95:053114.
- [39] Zhang HJ et al. (2011). Phys. Rev. L. 106:156402.
- [40] Yan B, Muchler L, Felser C (2012). Phys. Rev. L. 109:116406.
- [41] Perdew JP, Burke K, Ernzerhof M (1996). Phys. Rev. L. 77:3865.
- [42] Giannozzi P et al. (2009). Journal of Physics: Condensed Matter 21:395502.
- [43] Monkhorst HJ, Pack JD (1976). Phys. Rev. B 13:5188.
- [44] Mostofi AA et al. (2008). Comput. Phys. Commun. 178:685.
- [45] (year?). Available at <http://www.physics.rutgers.edu/pythtb/index.html>.
- [46] Nielsen H, Ninomiya M (1981) A no-go theorem for regularizing chiral fermions. Physics Letters B 105:219 – 223.
- [47] Qi XL, Hughes TL, Zhang SC (2008). Phys. Rev. B 78:195424.
- [48] Essin AM, Moore JE, Vanderbilt D (2009). Phys. Rev. L. 102:146805.
- [49] Taherinejad M, Garrity KF, Vanderbilt D (2014). Phys. Rev. B 89:115102.

- [50] Alexandradinata A, Bernevig BA (2014). [arXiv:1409.3236](#).
- [51] Thouless DJ (1983). [Phys. Rev. B 27:6083](#).
- [52] Wang YL et al. (2011). [J. Appl. Phys. 110:014101](#).
- [53] Meyer B, Vanderbilt D (2002). [Phys. Rev. B. 65:104111](#).
- [54] Lee D et al. (2009). [Phys. Rev. B. 80:060102R](#).
- [55] Behera RK et al. (2011). [J. Phys.: Condens. Matter 23:175902](#).
- [56] Marton P, Rychetsky I, Hlinka J (2010) Domain walls of ferroelectric  $\text{BaTiO}_3$  within the ginzburg-landau-devonshire phenomenological model. [Phys. Rev. B 81:144125](#).
- [57] Megaw H (1954). [Nature 155:484](#).
- [58] Hohenberg P, Kohn W (1964) Inhomogeneous electron gas. [Phys. Rev. 136:B864–B871](#).
- [59] Perdew JP, Zunger A (1981) Self-interaction correction to density-functional approximations for many-electron systems. [Phys. Rev. B 23:5048–5079](#).
- [60] Vanderbilt D (1990) Soft self-consistent pseudopotentials in a generalized eigenvalue formalism. [Phys. Rev. B 41:7892–7895](#).
- [61] Blöchl PE (1994) Projector augmented-wave method. [Phys. Rev. B 50:17953–17979](#).
- [62] Broyden C (1969). [Amer. Math. Soc. 16:670](#).
- [63] Fletcher R (1970). [Comput. J. 13:317](#).
- [64] Goldfarb D (1970). [Math. Comp. 24:23](#).
- [65] Shanno D (1970). [Math. Comp. 24:647](#).
- [66] Monkhorst HJ, Pack JD (1976) Special points for brillouin-zone integrations. [Phys. Rev. B 13:5188–5192](#).
- [67] Zhong W, King-Smith RD, Vanderbilt D (1994) Giant lo-to splittings in perovskite ferroelectrics. [Phys. Rev. Lett. 72:3618–3621](#).
- [68] Vanderbilt D, King-Smith RD (1993) Electric polarization as a bulk quantity and its relation to surface charge. [Phys. Rev. B 48:4442–4455](#).
- [69] Axe JD (1967) Apparent ionic charges and vibrational eigenmodes of  $\text{BaTiO}_3$  and other perovskites. [Phys. Rev. 157:429–435](#).
- [70] Hewat W (1974). [Ferroelectrics 6:215](#).
- [71] Rabe K, Ghosez P (2007) [Studies of Ferroelectric Oxides, Physics of Ferroelectrics: A Modern Perspective](#).
- [72] Lubk A, Gemming S, Spaldin NA (2009) First-principles study of ferroelectric domain walls in multiferroic bismuth ferrite. [Phys. Rev. B 80:104110](#).